UNIVERSITA’ DEGLI STUDI DI TORINO

Department of Chemistry

PhD program in Molecular Medicine

XXXV Cycle

ADVANCED MODELS FOR THE HAZARD/BIOCOMPATIBILITY ASSESSMENT OF MICRO- AND NANO-MATERIALS

Thesis author: Giulia Antonello

Supervisor: Prof. Ivana Fenoglio

Co-supervisor: Prof. Chiara Riganti

PhD program co-ordinator: Prof. Franco Novelli

Academic years of enrolment: 2019 – 2023

Code of scientific discipline: BIO10

Summary

Abstract

Nowadays, the human exposure to micro- and nano-materials is constantly increasing due to their consistent production and use. However, the possible effects that they could exert on human health are not still deeply understood. One of the main reason is the lack of advanced validated models on which to perform the tests.

The employment of models closer to human physiology and high throughput assays could help to fill this gap by better predicting the micro- and nano-materials exposure consequences.

With this aim, in this study a simple intestinal *in vitro* model, represented by Caco-2 cells, was implemented considering the cell heterogeneity, the intestinal fluids composition, and the intestinal microenvironment physical features. Moreover, a high throughput screening test for oxidative stress induction was validated.

Different physico-chemical changes based on the chemical nature of the tested particles (lipid-surfactant, carbon-based, iron oxide, and hydroxyapatite nanoparticles) after subjecting them to an *in vitro* simulated digestion and different effects on intestinal Caco-2 cell viability, inflammation, and barrier integrity were observed. The potential for the pre-treatment with a simulated digestion to increase the predictiveness of *in vitro* testing over *in vivo* circumstances is indicated by the comparison with the lipid-surfactant nanoparticles effects observed in mice, albeit with some differences probably due to the lack of some physiological features of the intestinal barrier such as cell heterogeneity, mucus secretion, and environmental characteristics. Implementing the model by using a Caco-2/HT29-MTX/M-cells co-culture, differences in inflammation and barrier integrity were also found after simulated digestion of high-density polyethylene microplastics with *V. parahaemolyticus* biofilm. Moreover, the application of physiological pressure

and flow showed different outcomes in terms of inflammation and barrier permeability on Caco-2/HT29-MTX/M-cells model exposed to microplastics.

Finally, the results obtained in different laboratories on the tested oxidative stress induction assay by using iron oxide, silver, and titanium dioxide nanoparticles were similar between each other, indicating a promising applicability of this test in high throughput screenings and representing an important step in raising the repeatability of *in vitro* tests and moving toward the creation of standardised protocols.

These findings suggest that the employment of advanced models and methods in testing micro- and nano-materials can help to better predict the effects that they could have on human health and reduce the use of animal testing.

1 Introduction

1.1 Micro- and nanomaterials

1.1.1 Micromaterials

Micromaterials (MMs) still do have not a common, univocal, and accepted definition, but they can be considered as structures with dimensions less than 1000 µm and greater than 1 µm [1–4].

MMs can derive from natural or artificial processes and can be made up of natural and/or synthetic substances. For example, among main MMs found in the environment there are the well-known asbestos particles that can derived from naturally formation by spontaneous disposition in long and thin crystalline fibres of hydrated silicates [5,6] or from artificial synthesis for industrial purpose [6,7]. Like these particles, others can be found as environmental MMs: silica dust [8], soot [9], cotton dust [10] and wood dust [11] are such examples of particles produced by human activities, while hay dust is one of those naturally present in the environment [12,13]. What join all of them is their potential for disease induction [14–19]. Not all MMs represent a danger for human health, indeed some MMs are synthesized and studied as medical devices from different purposes, especially for drug delivery.

Actually, some MMs are under study as carriers of drugs for different types of diseases for which there are evidence of increased efficacy and/or stability than free drug administration. Some examples can be found in the study of treatment of Alzheimer's disease [20], Chronic Obstructive Pulmonary Disease [21], and Tuberculosis [22].

Not only for drug delivery, but even in regenerative medicine MMs play an important role. In fact, different gelatine-based MMs are being studied both *in vitro* and *in vivo* to regenerate cardiac tissue [23,24], blood vessels [25], bones [26–28], cartilage [29][30], and muscles [31].

Moreover, another application of MMs can be found in the field of tumours theragnostic. In particular, Bi_2Se_3 nanodots and doxorubicin hydrochloride co-embedded tumour cell-derived microparticles were studied by Wang and colleagues observing the enhancement of cellular internalization followed by deepened tumour penetration and increased cell damage *in vitro* [32]. In addition, by combining the intravenous injection (low-dose chemotherapy) and laser irradiation at 808 nm (photothermal therapy) of these microparticles a good anti-tumour effects in H22 tumour-bearing mice was obtained [32].

In recent years, microplastics (MPs) emerged as a preponderant type of MMs. In fact, thanks to their unique properties, plastics are used in a huge range of commercial applications producing a large amount of waste that when abandoned and not properly disposed. They can break down into fractions generating the MPs that were the most studied plastics fraction in the last decade [33,34]. In the last years, they were under global attention because of their ubiquitous nature and, consequently, the high risk of human exposure and the associated risk to diseases (**Figure 1.1**). However, the possible effects that these particles can have on human health remain poorly understood [35]. The main reason can be found in the limited availability of realistic MPs. In fact, most of the studies on the possible health effects of MPs have been carried out on unrepresentative particles in terms of shape, heterogeneity and polymeric nature as they are represented by spherical polystyrene (PS) particles [36–43]. For this reason, there is the need to perform further studies to better understand what effects these particles could have on human health.

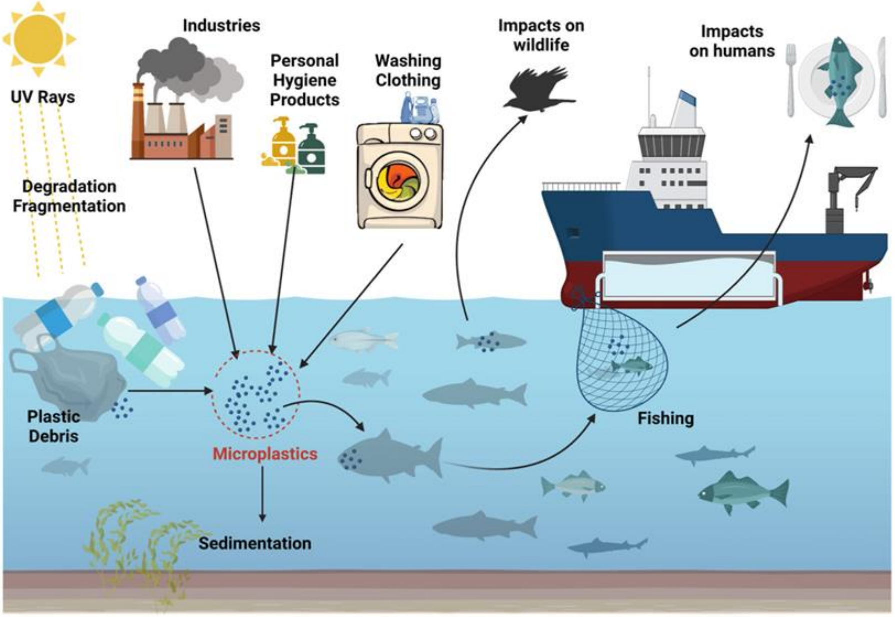

Figure 1.1. *Microplastics cycle. Adapted from Ziani et al., 2023* [44].

1.1.2 Nanomaterials

Unlike MMs, nanomaterials (NMs) are accurately defined by European Union thanks to scientific evidence provided by European Commission Joint Research Centre.

A "nanomaterial" is an organic, inorganic, or synthetic substance that contains at least 50% of solid particles that can be present alone or as identifiable constituent particles in aggregates or agglomerates and meet at least one of the following criteria in the number-based size distribution.

The particle has an elongated shape, like a rod, fibre, or tube, where two external dimensions are smaller than 1 nm and the other dimension is larger than 100 nm; the particle has a plate-like shape, where one external dimension is smaller than 1 nm and the other dimensions are larger than 100 nm; or the particle has one or more external dimensions that fall within the size range of 1 nm to 100 nm (**Figure 1.2**).

Particles with at least two orthogonal exterior dimensions larger than 100 µm need not be taken into account when determining the particle number-based size distribution. However, an item cannot be considered a nanomaterial if its specific surface area by volume is less than 6 m^2/cm^3 [45].

As described in the above definition, like MMs, also NMs can be naturally, accidentally or intentionally produced. In fact, NMs can spontaneously occurring from volcanic ash [46], mineral and salts deposition in water [47], erosion [48], and also from bacterial activity [49,50] or produced as secondary consequence of human activity [51]. Moreover, NMs can be produced and used in different field [52]. Some examples can be found in TiO_2 NMs that are used in cosmetics [53] and in paints industry [53][54], silica NMs employed in food industry [55], and Se NMs used in agriculture [56]. Another important emerging field in which NMs are employed is represented by biomedicine in which they take the name of nanobiomaterials (NBMs). This field include different branches of study of which the main examples are given below: drug delivery [57–60], diagnosis [61,62], and theragnostic [63]. The huge and ever increasing NMs employment in different fields is mainly due to their unique properties. In fact, they show different features than the corresponding bulk material. Some examples are the surface area that is higher than that of the bulk counterparts [64], the magnetism that can be appear only at the nanoscale level [65], the quantum effects that are more pronounced when the material is nanosized [66], the electrical and thermal conductivity that increases in nanomaterials compared to bulk materials depending on their nature [67], and extraordinary mechanical properties that can be absent in the macroscopic materials [68].

These particular features together with the increasing NMs usage can influence human exposure and the effects on human health, for this reason it is needed to deeply study the tissues/cells-NMs interaction to better understand case-by-case the NMs-associated risk.

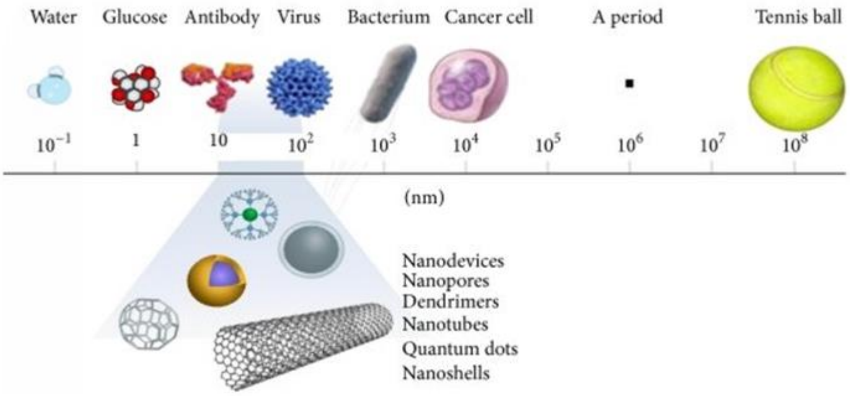

Figure 1.2. *Nanomaterials size comparison with other large materials. Adapted from Amin et al., 2014* [69].

1.2 Human exposure

As discussed above, both MMs and NMs present useful features that can be exploited in different fields, so their production is becoming more and more leading to a constant increase in human exposure.

This exposure can accidentally or voluntarily occur via different routes, among which the main ones have been identified in inhalation, ingestion, skin penetration, and injection [70].

Air pollution and worker exposure are the main source of inhaled MMs and NMs which mainly derived by exhausted gases from means of transport and industries, synthetic textiles, degradation of plastics and other wastes, building materials, waste incineration, and landfills [71–73]. According to recent works, it is estimated that urban air may contain 10,000–50,000 NMs/m^3 and 9.8 MPs/m^3 [74,75]. In NMs processing and manufacturing businesses, these presented limits may grow larger, which might be quite concerning for occupational safety [76]. A great number of studies through the last decades have reported that the exposure to air-suspended MMs and NMs could induce inflammation, cytotoxicity, and genotoxicity in lungs [77–

84] leading to the appearance of respiratory diseases, such as asthma, pneumoconiosis, and chronic obstructive pulmonary disease [85–87].

Ingestion, together with inhalation, is considered the major route of exposure to MMs and NMs due to their presence in food and beverages [88–90]. For example, it was estimated that beer and white wine may contain up to 256 particles/L and 2563–5857 MPs/L respectively [91], even if the first source of MPs ingestion has been identified in drinking water [89]. It was estimated that, on a global average, humans may consume up to 74,000–121,000 particles per year, or 0.1–5 g of MPs with a maximum size of 1 mm per week [75]. However, MMs and NMs could also being ingested in a voluntary way. As a matter of facts, a huge quantity of different particles is studied as oral delivery systems. An example can be found in pH-sensitive MPs studied for the intestinal delivery of cinnarizine [92]. Another one is represented by the study of nanolipospheres as oral delivery agent for cannabinoids [93]. The mechanisms and the effects of particles-intestine interaction will be discussed in detail in the following section, but it can be anticipated that, as above reported for inhalation, the main consequences of MMs and NMs ingestion are cytotoxicity, genotoxicity, and oxidative stress [94,95].

Another important source of MMs and NMs exposure is represented by personal care products. TiO_2, ZnO, and silver NMs are present in products that directly interact with skin [96][97], while plastic microbeads are frequently used as abrasives in cosmetic products, such as scrubs and exfoliating soaps, skin creams, and toothpaste [98,99]. Particles smaller than 4 nm can easy cross the skin through its pores [100] causing skin inflammation and cytotoxicity [101,102].

The injection of MMs and NMs occur only voluntarily. This route of exposure mainly concerns drug delivery systems. In fact, during the last years several MMs and NMs have been studied as vehicles for drugs to increase their stability in human body and to better allow their uptake into the target tissue.

Some examples are microaggregates of nanoparticles that mimic the platelet behaviour studied for drug delivery against circulatory system diseases [103], nano-cocrystal-delivered cytarabine used to enhance the drug antitumor activity [104], and endostatin-loaded carboxymethyl chitosan nanoparticles developed to inhibit the tumoral angiogenesis and hypoxia [105]. In the circulation system, some particles have been shown to be able to bind coagulation system biomolecules potentially causing haemorrhage or thrombosis [106] and from the blood circulation, they may reach any body area by penetrating through the endothelium [97].

The type and the magnitude of effects that particles can cause in different districts is strictly influenced by their chemical composition, size, and shape. For example, abilities like catalytic activity, production of reactive oxygen species (ROS), and absorption rate can be higher for smaller particles than for bigger ones [107,108]. Moreover, it was reported that gold is more toxic towards fibroblasts when it is shaped as nanospheres than as nanostars [109], but gold nanostars showed higher cytotoxicity than nanospheres and nanorods on tumoral osteoblasts and pancreatic cells [110]. In addition to this, another factor that can affect the toxicity of the particles is the presence of contaminants on their surface. MPs are the main example of this problem, in fact, to improve their features, plastics polymers are treated with additives such as phthalate esters and bisphenol A [111] which, once they enter the organism, cause negative effects on the reproduction capability, and increase the risk to develop allergic diseases and asthma [112,113]. Moreover, poorly degradable synthetic polymers such as high-density polyethylene (HDPE) and polyethylene terephthalate (PET) are rapidly colonised by microorganisms, acting as vectors for pathogenic species [114–116].

Another aspect that can influence the particles interactions inside the human body and their possible effects is the bio-corona formation. Biomolecules like proteins and lipids can bind the particles forming a layer that can partially or completely cover the surface [117]. This layer gives a new biological identity to the particles changing their mechanism of interaction with cells and the effects that can exert. In a study published in 2016, it is reported that different NMs (i.e., TiO_2, SiO_2, and carbon nanoparticles) showed higher cytotoxicity and inflammation on macrophages when fibrinogen was present on their surface [118]. On the contrary, in a recent study, gold nanoparticles showed a reduction in cytotoxic effects towards monocytes, dendritic cells, B cells, natural killer cells, and T cells in presence of a protein corona [119].

In general, after entering in the body, MMs and NMs can interact with cells leading to different cell responses possibly leading to toxic effects.

The main mechanism through which MMs and NMs exert their toxic action is oxidative stress, which results from an imbalance between free radicals and antioxidants in the body. As a result, extra free radicals accidentally interact with other molecules causing an imbalance in the respiratory system of the cells [120]. PS MPs showed to induce oxidative stress in mice's liver [121], while ROS production and consequent oxidative stress due to the disturb of respiratory chain have been reported in human fibroblasts after accumulation of Ag nanoparticles outside the mitochondria [122]. Interestingly, in a study conducted by Huang and colleagues, it was suggested that the biochemical mechanism underlying oxidative stress due to SiO_2 nanoparticles in BEAS-2B bronchial cells is the induction of heme oxygenase-1—an antioxidant enzyme via the signalling pathway of Nrf-2–ERK MAP kinase [123].

The second toxicity process is represented by inflammation. After low-density polyethylene (LDPE) MPs subcutaneous implants in rats, the presence of multinucleated giant cells derived from activated macrophages, a sign of an inflammation process, was observed [124]. In other studies, it was found an increased release of pro-inflammatory IL-6 in A549 alveolar cells exposed to TiO_2 nanoparticles [125], while in rats' bronchoalveolar lavage fluid high levels of IL-1β and macrophages inflammatory protein-2 were found after exposure to different metal oxide NMs [81].

Finally, the third main toxicity-driver mechanism is identified in genotoxicity. It can be primary or secondary depending on whether derives from direct particles-DNA interaction rather than indirectly by oxidative stress or inflammation caused by MMs/NMs [81,126]. An example of primary genotoxicity can be found in zirconia nanoparticles and nano- and micro-PS that are able to induce DNA double-strand breaks after 24 h of exposure on V-79 hamster lung cells and A549 cells, respectively [127,128]. As secondary mechanism, it was reported that silica nanoparticles tested on human peripheral blood lymphocytes and Wistar rats lead to secondary genotoxicity through the oxidants release derived from inflammatory cells [129].

1.2.1 Ingestion

As previously discussed, ingestion represents, together with inhalation, the main route of human exposure to MMs and NMs. Despite this, a relative low number of studies on possible effects of particles ingestion is still available today. This is mostly due to the gastrointestinal system complexity and the dearth of *in vitro* models that can replicate it.

The main organs of the oral-gastro-intestinal (OGI) tract are mouth, stomach, and intestine and together they form a mucosal tube that is responsible of the food's motility, digestion, and nutrients absorption [130]. Other organs such as salivary glands, liver, gallbladder, and pancreas have the task of producing the digestive fluids [130].

Since the intestine is the main responsible for the final step of digestion, and absorption of nutrients and water, its surface presents special structures called villi to increase the area available for the absorption [131]. These structures host different types of cells which are represented by enterocytes, which are involved in absorption, goblet cells, which produce mucus, enteroendocrine cells, which release hormones, Paneth cells, which regulate intestinal homeostasis in many ways, and microfold cells (M-cells), which phagocyte large exogenous particles and present antigens to the immune system [132]. All these cells, as the whole OGI tract, are mechanically protected by a mucus layer that represents the first barrier that ingested materials, including MMS and NMs, must diffuse and pass through before coming into contact with OGI epithelial cells. The ability to penetrate the mucus layer depends on the chemical nature of the particles, in particular on their surface charge. In fact, it was demonstrated that cationic nanoparticles like chitosan-based NMs have a mucoadhesive ability 10-50 fold higher than poly(isobutyl cyanoacrylate) nanoparticles due to the presence of positively charge on their surface that interact with the negatively ones of the mucins [133].

After the mucus, the second physical barrier of the intestine is represented by epithelial cells that, thanks to the connections they establish between each other by tight junctions (TJs), adherent junctions (AJs) and desmosomes, are able to regulate the absorption of nutrients and prevent the passage of bacteria and other particles maintaining the epithelium integrity [132,134,135].

As the thickness of the TJs is less than 0.4 nm, in a healthy barrier the ingested particles cannot cross the epithelium through the paracellular route [136], but some particles are able to perturb the barrier integrity by disrupting the TJs structures [137–139]. An alternative way to cross the intestinal epithelium is represented by transcytosis through M-cells and, in a lesser way, through enterocytes. An example of M-cells-mediated transcytosis can be found in the ability of carboxylated PS nanoparticles to cross an *in vitro* model of intestinal barrier [140], while in another study PS nanoparticles were found to be able to cross an *in vitro* intestinal model with no M-cells made up only from epithelial cells cultured both on porous inserts and on an Organ-on-Chip device [141].

After ingestion, the particles meet conditions that can drastically alter their bio-identity, including pH ranges from 2 to 8, strong ionic strength, interactions with mucus, and various proteins and enzymes. Consequently, depending on the chemical composition of the particles, dissolution, enzymatic degradation, aggregation/agglomeration, and surface changes, including the generation of bio-corona, may occur affecting the biological response [142,143]. For example, it was reported that SiO_2 and ZnO NMs dissolve more rapidly than TiO_2 and Fe_2O_3 NMs in a mouth simulated fluid [144]. At the same time, no agglomeration was found for SiO_2, TiO_2, and ZnO NMs, while Fe_2O_3 NMs formed large agglomerates [144]. In another study, food-grade TiO_2 subjected to a simulated digestion showed aggregation due to the formation of a hard corona that decreased the surface reactivity of the particles and their ability to induce oxidative stress on HCT116 intestinal cells [94].

In general, the OGI exposure to MMs/NMs generates local inflammation both *in vitro* and *in vivo* models for different types of particles [145,146]. Moreover, as demonstrated for TiO_2 NMs, the particles could cross the intestinal barrier entering the blood circulation and reaching other body sites exerting toxic effects such as necrosis of hepatocytes, lipid peroxidation and oxidative DNA damage in liver leading to hepatic injuries, and oxidative stress in red blood cells, liver, and brain [147,148].

For this reason, it is important to study in depth the possible consequences that MMs/NMs could have on human physiology.

1.3 Current (*in vitro*) methodologies for micro/nano-materials hazard assessment

In vitro models for the evaluation of MMs/NMs effects on human health have undergone many innovative changes over the years.

The intestinal models, for example, were born as 2D models and in particular were mainly represented by mono-cultures of Caco-2 cells. In fact, they have the ability to form a competent epithelial barrier after 21 days of culture on porous membrane inserts differentiating into adult enterocyte-like cells [149]. This allows to obtain a barrier useful for permeability studies thanks to the presence of typical intestinal TJs and brush border [149]. Unfortunately, these features are not enough to represent the intestinal physiology. As a matter of fact, in the intestinal epithelium there are many other types of cells, each with important functions [132]. For this reason, the researcher started to develop co-culture models that included different types of cells. An example is the co-culture of Caco-2 cells and HT29-MTX cells, a model that considers even the production of mucus [150]. In order to obtain a model exploitable to absorption studies, the last cited one was implemented with M-cells that, unlike enterocytes, are able to carry out the transcytosis even of big particles [151]. This was successfully obtained thanks to the addition in the culture of Raji B cells that allow the Caco-2 differentiation into M-cells [140]. The latter represents one of the most current used models and in a recent study conducted by the Italian Health Institute "Istituto Superiore di Sanità" it was considered the standardization of an intestinal *in vitro* advanced model for nanoparticles uptake and crossing, testing on it SiO_2 nanoparticles [152].

Other barrier models closer to the intestinal anatomy and physiology have been recently developed by using murine, porcine, or human *ex-vivo* systems to study the intestinal permeability after nanoemulsions or latex beads exposure [153,154]. The most recent advances are represented by 3D systems that exploit scaffold to reproduce the 3D intestinal structure and that could even successfully mimic the microenvironment, mechanical peristalsis, fluid system, signalling gradients or other important aspects of the original human intestine [155]. Unfortunately, none of these models consider the possible change that the particles surface along the passage through the OGI tract. For this reason, in the last years some *in vitro* simulated digestion models have been developed [144,156] to predict the physicochemical properties modification that can occur in consequence to particles interaction with digestive fluids [157–159]. However, few studies are still available on the possible effects that these changes can induce to the intestinal physiology [94,160–162].

Other models suitable for micro- and nanotoxicity studies that are currently evolving are those for the evaluation of particles oxidative stress induction.

The ROS production assessment by physical techniques such as electron paramagnetic resonance (EPR) spectroscopy represents the first step of the evaluation of surface reactivity of MMs and NMs [163–165] that even allows to discriminate between different species of ROS based on the specificity of the probes [163,166]. However, in cellular experiments is more practical to rely on probe-based biological assays that are unable to discriminate between the different type of ROS. Moreover, in the cell environment the particles can have different behaviour. In fact, oxidative stress can be induced by direct ROS production by particles [167,168] or can be indirectly triggered by cells-produced ROS in response to the interaction of the particles with a variety of biological targets as a consequence of cell respiration, metabolism, inflammation, and metabolism of different particles [169] leading to the mitochondria damage [170,171].

For this reason, cell-based methods have been considered to predict the potential oxidative stress generation. Probes like 5-(and-6)-chloromethyl-2′,7′-dichorodihydrofluorescein diacetate-acetoxymethyl ester (DCFDA) have been employed to test the ROS generation in target cells, as in the case of carbon nanoparticles studied for the treatment of lung cancer [172]. Another method suitable for the evaluation of oxidative stress in target cells is the immunohistochemistry through which it is possible to evaluate the expression and translocation into the nucleus of the transcription factor nuclear factor erythroid 2-related factor 2 (Nrf2) that regulates the switch of various of cytoprotective genes after redox insults [173]. Unfortunately, none of the previous described technics allows a high throughput screening. The KeratinoSens^{TM} assay is based on immortalised human keratinocytes (HaCaT) stably transfected with luciferase that emit a luminescent signal when the NRF2 gene is activated. It is recognized as a Test Guideline by the OECD since 2018 [174] and recently was successfully used to test different NMs like CuO, Co_3O_4, NiO, TiO_2, CeO_2, Fe_2O_3, and ZnO NMs [175]. This assay has been taken as example to produce other similar tests based on other cell types to produce high throughput screening methods to determine the oxidative potential of particles [176,177].

2 Aim of the study

This study is aimed to explore advanced methods and models to better predict *in vitro* the effects of particles in the human organism.
Starting by the Caco-2 cells line, the simplest and most used model for the *in vitro* evaluation of intestinal effects of MMs/NMs, we investigated different co-culture models in order to obtain more physiological conditions (i.e., cell heterogeneity, mucus production). Moreover, considering that the digestive process along the OGI tract can dramatically modify the physico-chemical properties of ingested particles, we applied an *in vitro* simulated digestion system. Finally, a dynamic model was developed by using a milli fluidic system. The models were in part validated by *in vivo* experiments. Moreover, a validation of the high throughput method to predict the oxidative stress induction was performed by an interlaboratory study.

3 Development of human digestive system for the assessment of *in vitro* intestinal nanobiomaterials biocompatibility

The study enclosed in this chapter was conducted in context with the European project BIORIMA and it was realized in collaboration with National Technical University of Athens, Colorobbia Consulting Srl, Nanovector Srl, Institute of Science and Technology for Ceramics ISTEC-CNR, Royal College of Surgeons in Ireland, and Université Grenoble Alpes. It was aimed to develop a human *in vitro* model of the digestive system to assess the biocompatibility of nanobiomaterials.

3.1 Materials and methods

3.1.1 Materials and reagents

Plastic ware for cell cultures was purchased from Falcon (Becton Dickinson, Franklin Lakes, NJ), while foetal bovine serum (FBS) and culture medium were from Invitrogen Life Technologies (Carlsbad, CA).
Reagents were purchased from Sigma-Merck unless otherwise noted.

3.1.2 Nanobiomaterials (NBMs)

According to a previously disclosed process [163], carbon nanoparticles (CNPs) were created by hydrothermal carbonization of glucose and then suspended in water to create a colloidal suspension. Lipid surfactant nanoparticles (LSNPs) were created by Nanovector srl Turin, Italy, and are made of water (Citrate/Phosphate buffer pH 5), glycerol, soy lecithin, glyceryl citrate/lactate/oleate/linoleate (E-472), glycerol monostearate (E-471), polysorbate 20, ascorbyl palmitate, sodium benzoate, α-tocopheryl acetate, strawberry favour, sucralose and loaded with Melatonin (0.1% (w/w)). Magnetite nanoparticles (FNPs) are Fe_3O_4 nanoparticles embedded in a polymeric matrix made of poly-lactic-co-glycolic acid and polyethylene glycol, are suspended in phosphate buffer 1 mM and were produced by Colorobbia Consulting, Vinci, Italy. Hydroxyapatite (HNPs) were obtained from Sigma Aldrich (Merck KGaA, Darmstadt, Germany) in the form of a powder that is composed of stoichiometric calcium hydroxyapatite ($Ca_5(PO_4)_3OH$) and then suspended in water.

3.1.3 Dynamic light scattering (DLS) and Electrophoretic light scattering (ELS)

A 633 nm HeNe laser-equipped Zetasizer Nano instrument (Malvern Instruments, UK) were used for the measurements. Size distribution and polydispersity index (PDI) measurements were performed on treated and untreated NBMs diluted in ultrapure water (100 µg/ml) or in cell medium (DMEM supplemented with 10% FBS, 1% penicillin/streptomycin solution) (100 µg/ml). Replicate 3, equilibrium time 60 s, T=25 °C, dispersant refractive index 1.330 for water and 1.345 for the cell medium, dispersant viscosity 0.8872 cP for water and 0.8000 cP for the cell medium, material refractive index 1.410 for LSNPs, 2.420 for CNPs, 2.420 for FNPs, and 1.650 for HNPs, and material absorption of 1.000 were the instrument settings. Before analysis, untreated NBMs were diluted in ultrapure water, and HNPs were also subjected to a 5-minute sonication with a probe sonicator (Sonoplus HD3100 Bandelin, Microtip MS73, diameter 3 mm, power 100 W, amplitude 30%). Without dilution, treated NBMs were directly analysed in fluids.

NBMs were diluted to 500 µg/ml in ultrapure water for the ζ-potential curve *vs* pH, and pH was changed by using 0.1 M NaOH or HCl. Dispersant (water) dielectric constant: 78.5 was the instrument setting.

The average values of 15 measurements from three separate studies are shown by each line.

3.1.4 Flow particle imaging analysis (FPIA)

Using a Sysmex FPIA3000 analyser, the flow particle imaging analysis (FPIA) was carried out. A high-power field with a secondary lens was used, allowing the measurement of particles between 1 and 40 µm. Rotina 380 R (Hettich Zentrifuger) was used to centrifuge the nanoparticle suspensions in the simulated digestive fluids for 10 minutes at 8000 rpm. After pelletizing the suspensions and removing the supernatant, the pellets were resuspended in ultrapure water for two minutes in an ultrasonic bath. 5 ml of the suspensions were analysed after the washing procedure that was carried in triplicate.

3.1.5 Surface reactivity

By using TEMPONE-H (1-hydroxy2,2,6,6-tetramethyl-4-oxo-piperidine, Enzo Life Sciences, Inc.) as a spin probe, EPR analysis (Miniscope 100 EPR spectrometer, Magnettech, Berlin, Germany) was performed to monitor the surface reactivity of the NBMs. The suspensions in ultrapure water or cell media of untreated or SHDS-treated NBMs (0.5 mg/ml) were diluted 1:1 in a 100 µM solution of Tempone-H, which was then swirled continuously in a glass container. A sample aliquot (50 µl) was used to record the EPR spectra. Microwave power was set at 7 mW, modulation amplitude to 1 G, scan time to 80 s, and two scans were carried out for each sample.

3.1.6 Transmission electron microscope (TEM) measurements

A 200 kV-operating FEI CM20 microscope was used to perform transmission electron microscope (TEM) analysis. One drop of a diluted sample was placed to a carbon-coated Cu grid allowing the solvent to evaporate to create TEM samples.

3.1.7 Protein corona analysis

NBMs were treated with SHDS in accordance with the following methodology. Both treated and untreated NBMs (0.5 mg/ml) were incubated for 24 h at 37 °C with agitation in DMEM with 10% FBS, 1% penicillin/streptomycin. Following the incubation, three centrifugation/dispersion cycles in PBS were used to separate the NBM-corona complex. Ferromagnetic spheres were used to separate the complex NBMs-corona for FNPs (unpublished data). After washing, the pellets were stripped using a loading buffer (Cell Signalling Technologies) in 0.1 M dithiothreitol and heated to 100 °C for SDS-PAGE. Following the centrifugation of the resulting solutions, the samples were loaded into a 10% acrylamide gel. The Mini-Protean (BioRad) machine was used to perform SDS-PAGE at 120 V until the dye front reached the gel end. The gels were dyed with Coomassie (Termo Scientific), and the Amersham Gel doc system was used to scan them. The samples in the gel were trypsinised and then treated with various solutions to remove the peptides from the gel matrix in preparation for the mass spectrometry analysis. The MaxQuant version 2.0.1.0 was used to process the raw mass spectrometry data [178]. The UniProt database was used to identify the peptides and proteins. The acquired LFQ intensities were analysed using Perseus software version 1.6.15.0 [179]. Data were log transformed, and values from a normal distribution were used to fill in the gaps left by missing values.

3.1.8 Cell cultures

American Tissue Culture Collection (ATCC) provided the Caco-2 epithelial colon cells, which were cultured in DMEM with 20% v/v FBS and 1% v/v penicillin/streptomycin. Cells between passages 33 and 47 were employed for the tests, and they were incubated in Dulbecco's Modified Eagle Medium (DMEM) supplemented with 10% v/v FBS and 1% penicillin/streptomycin. Cells were cultivated on Millicell®-96 cell culture inserts (Merck KGaA, Darmstadt, Germany) for 21 days to produce Caco-2 monolayer establishing a competent intestinal barrier model [180]. HCT116 cells, obtained from the European Collection of Authenticated Cell Cultures (ECACC, catalogue No. #91,091,005), were cultured, and exposed to NBMs in McCoy's 5a medium with 2 mM glutamine, 10% FBS, and 1% penicillin/streptomycin. Cells were used between passage 15 and 25. Colonic epithelial cell medium (HCoEpiCM) with 10% v/v Colonic epithelial cell growth supplement (HCoEpiCGS) and 1% v/v penicillin/streptomycin was used to cultivate human colonic epithelial cells (HCoEpiC), which were bought from CliniSciences (CliniSciences, Guidonia Montecelio, Italy). Experiments were performed between the passage 5 and 8.

3.1.9 Simulated human digestion system (SHDS)

Following the procedure employed by Sohal et al. [144], the production of simulated digestive fluids and the simulation of the human digestive system were carried out. **Table 3.1** provides an overview of each simulated digestive fluid composition. The organic and inorganic components of each fluid were individually prepared by adding them to ultrapure water and letting them dissolve under magnetic stirring. The two solutions were then combined in a 1:1 (v/v) ratio and stirred overnight. Just before starting the experiment, the active components were added, and the solution was vortexed to suspend them.

A 1 mg/ml NBM suspension was treated with SHDS using the same volume of simulated digestive fluids (**Figure 3.1**). After adding the simulated saliva fluid (SSF), the sample was shaken and incubated for 15 min at 37 °C. Simulated gastric fluid (SGF) was then added and incubated for 4 h after that. Finally, simulated intestinal (SIF) was added and incubated for an additional 4 h. SIF is made up of simulated duodenal fluid (SDF) and simulated biliary fluid (SBF) in a ratio of 2:1 v/v. The simulated digestive fluids ratio was 1:2:3. (**Figure 3.1**). If necessary, pH was adjusted between 6.5 and 7.5 at the end of the procedure using 1 M $NaHCO_3$, and the suspension was sterilised for 15 minutes using UV rays. For the purpose of determining the surface reactivity of the suspension, it was centrifuged at 11,000 rpm (Rotina 380 R, Hettich Zentrifuger), and the supernatant was discarded before the suspension in cell culture medium in a volume based on the desired concentration. To get the final concentration for other testing, the suspension was directly diluted with cell medium. Cells or intestinal barrier model were incubated for 24 h.

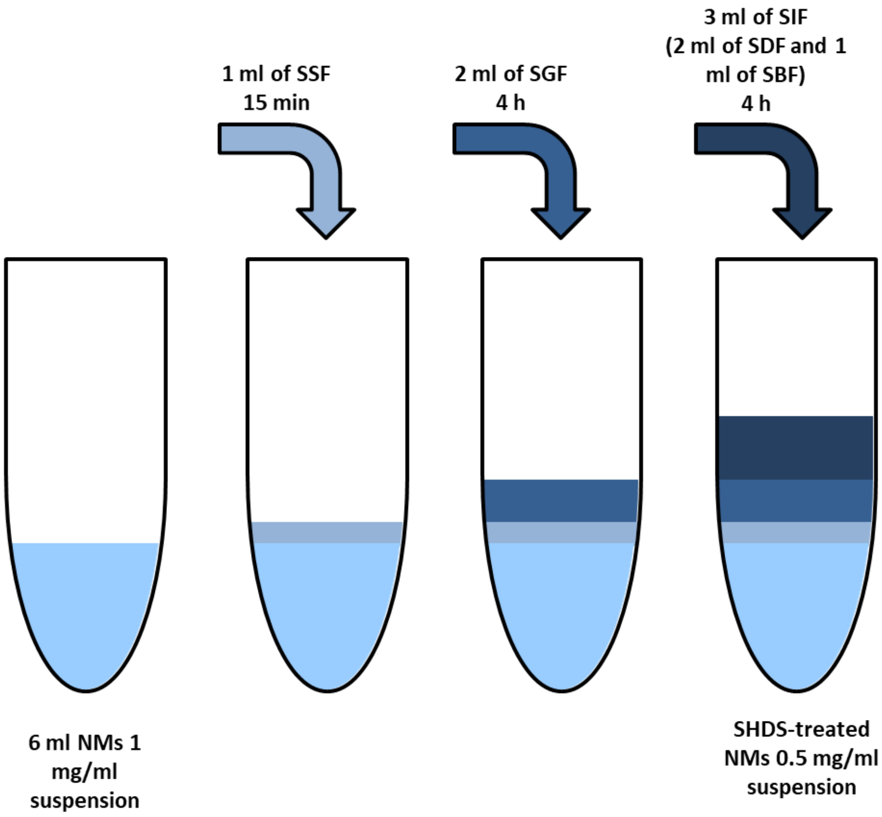

__Figure 3.1.__ Representative SHDS treatment.

Table 3.1. *Composition of simulated digestive fluids for the simulated digestion model (amounts based on 100 ml of fluid).*

Fluids	**Saliva**	**Gastric juice**	**Duodenal fluid**	**Bile**
pH	6.5 ± 0.1	1.4 ± 0.1	8.1 ± 0.1	8.0 ± 0.1
Inorganic fraction	89.6 mg KCl 20 mg KSCN 102.2 mg $NaH_2PO_4xH_2O$ 57 mg Na_2SO4 29.8 mg NaCl Milli-Q water	30.6 mg NH_4Cl 40 mg $CaCl_2x2H_2O$ 82.4 mg KCl 275.2 mg NaCl 30.6 mg $NaH_2PO_4xH_2O$ Milli-Q water	5 mg $MgCl_2x6H_2O$ 56.4 mg KCl 8 mg KH_2PO4 338.8 mg $NaHCO_3$ 701.2 mg NaCl Milli-Q water	37.6 mg KCl 578.5 mg $NaHCO_3$ 525.9 mg NaCl Milli-Q water
Organic fraction	20 mg urea Milli-Q water	8.5 mg urea 65 mg D-glucose 2 mg glucuronic acid 33 mg D-glucosamine hydrochloride Milli-Q water	25 mg urea Milli-Q water	10 mg urea Milli Q-water
Enzymes	5 mg mucin (porcine stomach) 1.6 mg uric acid 14.5 mg α-amylase (Bacillus subtilis)	300 mg mucin (porcine stomach) 100 mg albumin (bovine serum) 100 mg pepsin (porcine gastric mucosa)	300 mg pancreatin (porcine pancreas) 50 mg lipase from (Candida rugosa) 100 mg albumin (bovine serum)	600 mg bile (bovine) 180 mg albumin (bovine serum)

3.1.10 Viability assay

After treatment with NBMs, the cell viability—as a measure of mitochondrial activity—was assessed using the WST-1 assay. Its principle relies on the cleavage of the slightly red tetrazolium salt WST-1 (4-[3-(4-iodophenyl)-2-(4-nitrophenyl)-2H-5-tetrazolio]-1,3-benzene disulfonate) into a dark red formazan dye by metabolically active cells. WST-1 was added at 10% v/v in cell medium, and the absorbance was measured at 440 nm after 2 h for Caco-2 cells, 1 h and 30 min for HCT116 cells, 4 h for HCoEpiC cells, and 30 min for the intestinal barrier model using a Synergy HT Multi-Detection Microplate Reader (BioTek Instruments, Winooski, VT) or a Spectramax ID3 plate reader (Molecular Devices, for HCT116 cells only). The reference (630 nm) absorbance value was subtracted from absorbance obtained at 440 nm.

3.1.11 Genotoxicity assay

After immunostaining of the 53BP1 DNA repair protein, as previously described [181,182], genotoxicity was evaluated by counting the DNA double strand break repair foci. After being exposed to NBMs, cells were permeabilized with 0.2% v/v Triton X-100 produced in PBS containing 3% w/v bovine serum albumin and fixed with 4% v/v paraformaldehyde (PBS-BSA). PBS-BSA was used to block non-specific sites, followed by the dilution of a rabbit polyclonal anti-TP53BP1 antibody (Abnova, reference PAB12506) for 1 h in PBS-BSA, three PBS-BSA-washes lasting 5 min each, and a 1 h incubation with an anti-rabbit IgG Atto 633 antibody (Sigma-Aldrich, 41,176) for the remaining non-specific sites. The nuclei were stained with 0.3 g/ml Hoechst 33,342 (Sigma-Aldrich) for 20 min at room temperature after three washes in PBS-BSA containing 0.2% Triton X-100. Using a CellInsight CX5 High-Content Screening Platform, the number of cell nuclei and the average number of 53BP1 foci per cell nucleus were enumerated (Thermo Fisher Scientific). There were n=5 replicates in each of the three independent experiments that this experiment was replicated in.

3.1.12 Trans-Epithelial Electrical Resistance (TEER)

3.1.12 Trans-epithelial electrical resistance (TEER) was measured using the Millicell® ERS-2 voltohmmeter (Merck KGaA, Darmstadt, Germany) to assess the barrier development and integrity of the Caco-2 barrier model. The resistivity was calculated by subtracting the value of the cell-free inserts from the value of the cell-containing inserts and multiplying by the growth area. The resistance was measured in ohms. Only monolayers with values greater than 250 *cm^2 were exposed to NBMs.

3.1.13 Evaluation of barrier permeability

The intestinal barrier model permeability was assessed using the trans-epithelial passage of Lucifer Yellow (LY) fluorescent dye [183] in accordance with the NANoREG SOP (Standard Operating Procedure for evaluation of NPs impact on Caco2 cell barrier model). Hanks' Balanced Salt Solution (HBSS) was used to wash the cells and the basolateral (Bl) compartment of Millicell®-96 cell culture inserts after medium collection. Thereafter, in the apical (Ap) compartment, 50 µl/well of a 0.4 mg/ml LY solution in HBSS were added. After 2 h of incubation at 37 °C, a Synergy HT Multi-Detection Microplate Reader was used to read the relative fluorescence units (RFUs) (excitation: 504 nm, emission: 529 nm) and calculate the apparent permeability (P_{app}) and the percentage of fluorophore recovered from the lower chamber in cell-free inserts.

P_{app} was calculated with following formula:

$$P_{app} = ((\Delta Q/\Delta t)\cdot V)\cdot(1/AC_0)$$

where $\Delta Q/\Delta t$ ((mg/mL)/s) is the LY passage rate from the Ap to the Bl chamber, V is the Bl volume (cm^3), A (cm^2) is the area of the membrane, and C_0 (mg/mL) is the initial LY concentration in the Ap chamber.

3.1.14 NBMs absorption through the intestinal barrier by Nanoparticle Tracking Analysis (NTA)

Nanoparticle Tracking Analysis (NTA) (ZetaView, Particle Metrix GmbH, Germany) was used to count the number of particles in the initial suspension and in the Bl compartment of the Millicell®-96 cell culture inserts in order to assess the CNPs and FNPs passage through the Caco-2 intestinal barrier. Prior to examination, the samples were diluted in ultrapure water. Shutter value was set to 100 and sensitivity to 60. Under these conditions, no phenol red nor FBS interference could be found.

3.1.15 FNPs absorption through the intestinal barrier by colorimetric assay

Based on the procedures described by Jeinter [184] and Balivada and coworkers [185], the FerroZine™-based colorimetric assay was used to quantify FNPs in the Bl compartment. Briefly, 150 µl of the samples were incubated with 150 µl of 1.2 M HCl and 60 µl of 1 M ascorbic acid at 70 °C for 2 h in order to dissolve and reduce the iron present in FNPs. Subsequently, 300 µl of the resultant solution were incubated with 100 µl of 21 mM FerroZine™ (Thermo Fisher Scientifc), 200 µl of 1.5 M sodium acetate, 50 µl of 1 M ascorbic acid, and 350 µl of ultrapure water. An UV-Vis spectrophotometer (UVICON 930, Kontron Instruments, Basel, Switzerland) was used to detect the absorbance at 562 nm after 20 min of incubation at room temperature, and the concentration was determined using a calibration curve.

3.1.16 Quantitative Real-Time PCR (qRT-PCR)

The phenol/chloroform/ethanol procedure was used to extract the mRNA from the cells. Cells were lysed in 0.5 ml of RiboZol (VWR; Radnor, PA), incubated for 10 min at room temperature, and then 0.2 ml of chloroform was added. The samples underwent a 15 s shake, a 3 min incubation at room temperature, and a 15 min 12,000 g, 4 °C centrifugation. After transferring the aqueous phase to a fresh tube and adding 0.2 ml of isopropanol, the samples were incubated for 10 min at room temperature before being centrifuged at 12,000 g for 10 min at 4 °C. RNA pellets were then resuspended in RNAse-free water after two washes in ethanol 70%. RNA was quantified by reading the absorbance at 260 nm with the Take3 plate (Synergy HT Multi-Detection Microplate Reader). After that, RNA samples were subjected to a reverse transcription using the iScript cDNA synthesis kit (Bio-Rad, Segrate, Italy), according to the manufacturer’s instructions. qRT-PCR was carried out using as gene reference the ribosomal protein unit S14 coding gene to quantify the expression of the genes of interest reported in **Table 3.2**. Briefly, for each sample were added to the well 5 µl of iTaq Universal SYBR Green Supermix (Bio-Rad Laboratories), 2 µl of 5 µM primers mix and 3 µl of cDNA (5 ng/µl). Using a CFX96 Real-Time System (Bio-Rad Laboratories) the samples were run for 30 s at 95 °C, 5 s at 95 °C and 30 s at 60 °C for 42 cycles. Bio-Rad CFX Maestro software (Bio-Rad Laboratories) was used for the analysis.

3.1.17 Statistical analysis

ANOVA (ANalysis Of VAriance) with post-hoc Tukey Honestly Significant Difference Test Calculator for comparing multiple treatments [186], were used for statistical analyses by using Statistical Package for Social Science software (IBM SPSS Statistics v.19). $p < 0.05$ was considered significant.

Table 3.2. *Genes and respective sequences of qRT-PCR primers.*

Gene	Forward (5'-3')	Reverse (5'-3')
TJP1	CCCCACTCTGAAAATGAGGA	ACAGCAATGGAGGAAACAGC
OCLN	ATGCCATGGGACTGTCAACT	TTTGTGGGACAAGGAACACA
CLDN3	CCTGCGTCTGTCCCTTAGAC	CACGCGAGAAGAAGTACACG
CLDN5	GCTGTTTCCATAGGCAGAGC	CCCTGCCGATGGAGTAAAGA
TNF	TGGGATCATTGCCCTGTGAG	GGTGTCTGAAGGAGGGGGTA
IL6	GGTACATCCTCGACGGCATCT	GTGCCTCTTTGCTGCTTTCAC
IL10	AGACAGACTTGCAAAAGAAGGC	TCGAAGCATGTTAGGCAGGTT
IL22	GCTGCCTCCTTCTCTTGG	GTGCGGTTGGTGATATAGG
S14*	AGGTGCAAGGAGCTGGGTT	TCCAGGGGTCTTGGTCCTATTT

* Reference gene

3.2 Results

3.2.1 Properties of NBMs

Three colloidal formulations composed by elemental carbon nanoparticles (CNPs), lipid-surfactant nanoparticles (LSNPs) and PLGA-PEG coated magnetite nanoparticles (FNPs) and one powdered sample of hydroxyapatite nanoparticles (HNPs) were selected for this study.

Table 3.3 summarize the main properties of materials.

Dynamic Light Scattering (DLS) and Electrophoretic Light Scattering (ELS) were respectively employed to investigate the size distribution and the surface properties of the NBMs (**Table 3.3 and Figure 3.2 A and B**).

CNPs and FNPs appeared to be stable, monodisperse colloidal suspensions based on the low polydispersity index values (PDI) and the modest standard deviation (SD) of the size distribution (**Table 3.3**). Although particles or aggregates in the nanometric or sub-micrometric range were found, CNPs and FNPs were primarily formed of nanometric particles (100 nm) (**Figure 3.2A**).

Table 3.3. *Physico-chemical properties of samples.*

Samples	**Appearance**	**Concentration (mg/ml)**	**Z-average hydrodynamic diameter (nm)***	**ζ-potential (mV) ****	**pH ****
LSNPs Lipid-surfactant nanoparticles	Colloidal suspension	12	135.0 ± 0.5 PDI 0.244	-16.3 ± 1.5	5.46
CNPs Carbon nanoparticles	Colloidal suspension	1.2	130.8 ± 1.0 PDI 0.170	-52.6 ± 1.0	4.60
FNPs PLGA-PEG coated Fe_3O_4 nanoparticles	Colloidal suspension	2	83.2 ± 0.5 PDI 0.169	-40.8 ± 1.0	6.84
HNPs Hydroxyapatite nanoparticles	Powder	1	3126 ± 523 PDI 0.648	-2.0 ± 0.2	7.75

* DLS measurement, samples diluted in water (100 µg/ml).
**ELS and pH measurement, samples diluted in water (100 µg/ml).
PDI is referred to Polydispersity Index.

According to DLS, LSNPs showed a bigger size than CNPs and FNPs, mostly in the sub-micrometric range (**Figure 3.2A**). However, given that DLS techniques overestimate the abundance of particles with the biggest sizes, it might correspond to the presence of a small number of sub-micrometric particles. With clear sedimentation over time, HNPs generated in water unstable suspensions, showing in DLS analysis the presence of big particles with sizes close to the upper range of the instrument (**Figure 3.2A**).

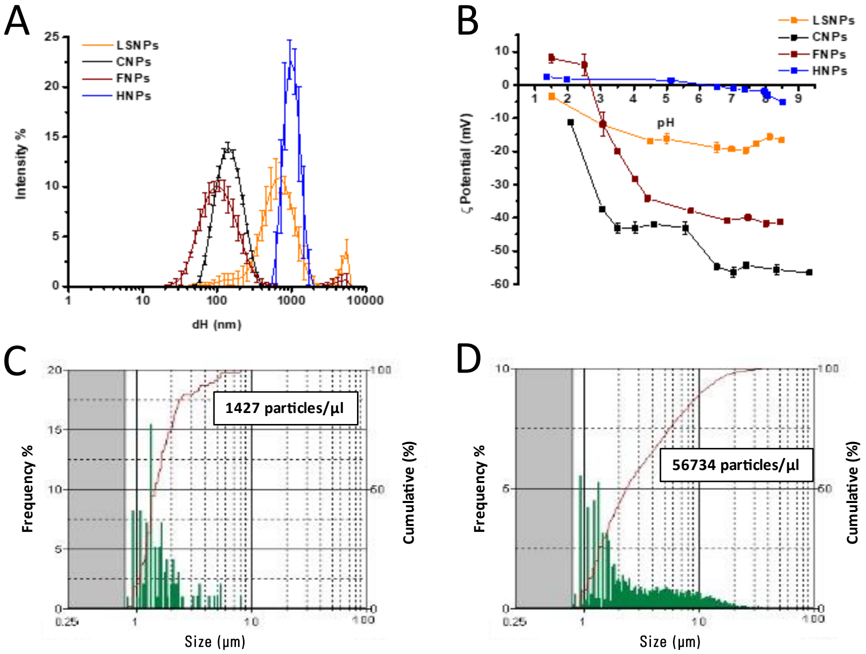

***Figure 3.2. NBMs size distribution**. **A)** DLS-measured hydrodynamic diameter distribution of the samples in water; Each line is the mean of three independent experiments +/- SD.; **B)** ζ-potential vs pH curve of the samples evaluated by ELS; **C, D)** Size distribution of **C)** LSNPs and **D)** HNPs evaluated by Sysmex FPIA3000 analyzer.*

LSNPs and HNPs were also subjected to FPIA (size range 1-150 µm) (**Figure 3.2 C and D**) to detect particles/aggregates larger than the maximum limit of detection of the DLS technique (5 µm) present in these suspensions. FPIA actually confirmed the presence of a few particles with diameters between 1 and 10 µm in LSNPs suspension (**Figure 3.2C**). In the case of HNPs, the particle sizes ranged widely, from 400 nm to 20 µm (**Figure 3.2A and D**). Further information on the four NBM structural features is discussed in following section after TEM analysis. The presence of negatively charged surface groups was evident in the LSNPs and CNPs negative ζ-potential values across the entire pH range (**Figure 3.2B**), as was expected. Only at extremely low pH levels FNPs exhibited positive ζ-potential values (**Figure 3.2B**), most likely as a result of the magnetite core involvement. At all pH values, HNPs showed ζ-potential values that were near to 0 mV, which is consistent with the instability of the suspensions (**Figure 3.2B**).

3.2.2 Effect of the Simulated Human Digestive System (SHDS) on the measured particles size.

After subjecting NBMs to SHDS, changes in the size distribution, surface modifications, and degradation by enzymatic digestion or dissolution were monitored.

First, integrating DLS and FPIA data, the changes in size distribution during the SHDS treatment was investigated comparing the hydrodynamic distribution in the different compartments with those measured in water **Figure 3.3**.

For LSNPs and CNPs in SSF, there was no change in the size distribution (**Figures 3.3A and B**), but for FNPs and HNPs, it was observed a shift in the distribution curve toward larger diameters (**Figures 3.3C and D**), which would indicate agglomeration or aggregation. All NBMs underwent to an important destabilisation in SGF, as indicated by both a shift in the diameters toward high values and an increase in the standard deviation of the measurements for LSNPs, CNPs, and FNPs (**Figure 3.3A-C**). HNPs also were destabilised, but the size shifted towards lower values (**Figure 3.3D**), in contrast to what observed for the others NBMs. This was expected given the media high ionic strength and low pH. In fact, in the case of HNPs, the particles are predicted to dissolve in the SGF since their solubility at acidic pH [187], and eventually to re-precipitate in the SIF in the end (**Figure 3.4**). Even in the SIF, the suspensions remained extremely unstable, and the final suspension visually revealed the presence of large aggregates (**Figure 3.5**). FPIA revealed the existence of micrometric particles, aggregates, or agglomerates, although in varying amounts between different NBMs suspensions (**Figure 3.3E-H**).

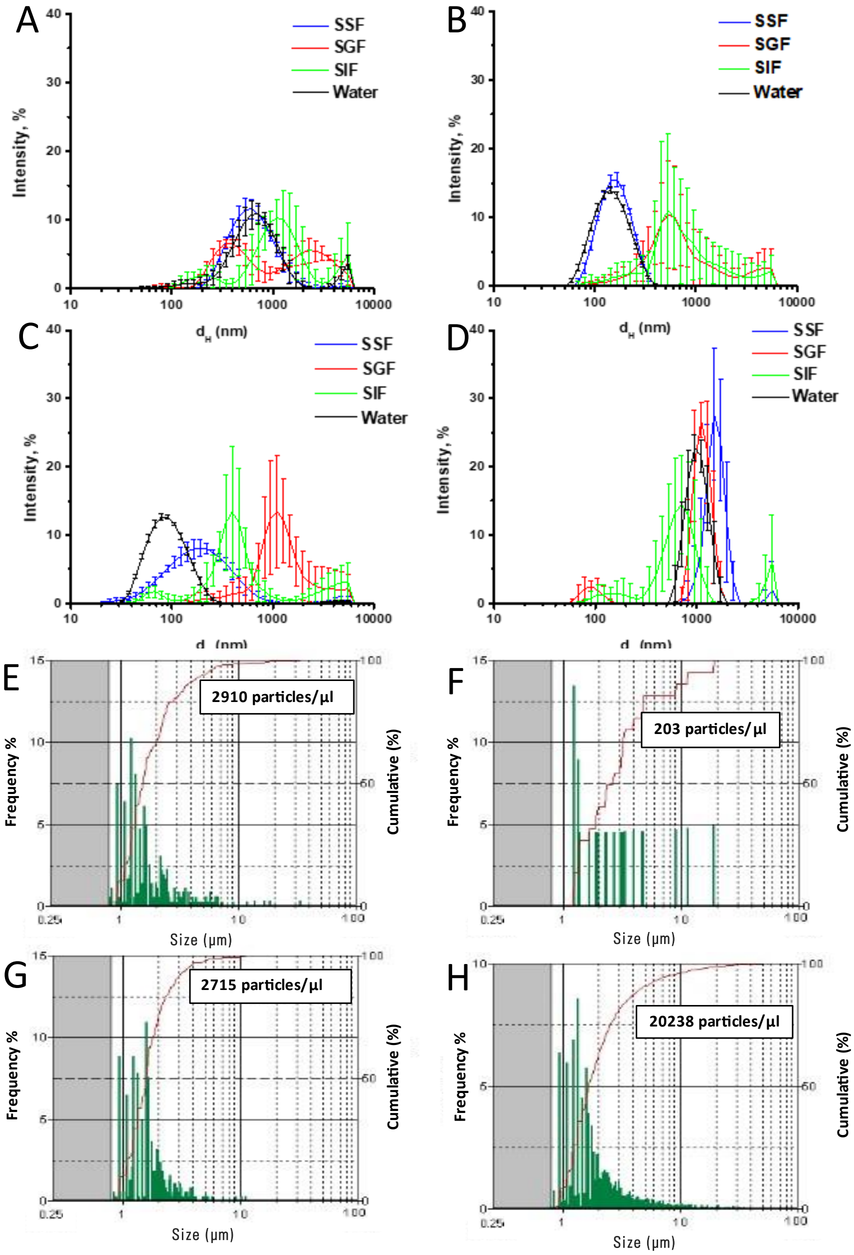

***Figure 3.3. SHDS-treated samples size distribution.** DLS patterns in the different compartment of the SHDS; **A**) LSNPs; **B**) CNPs, **C**) FNPs; **D**) HNPs and FPIA patterns after SHDS; **E**) LNPs; **F**) CNPs, **G**) FNPs; **H**) HNPs. In the box the number of particles analysed.*

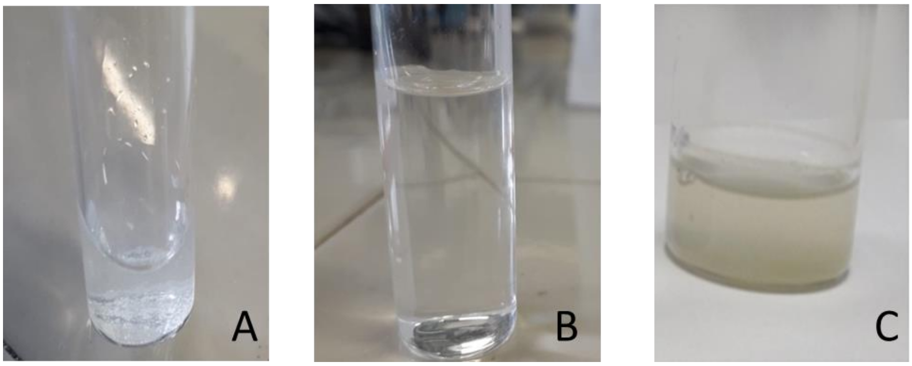

Figure 3.4. HNPs dissolution at acid pH. ***A****) HNPs suspension in water and* ***B****) in water at pH 1.4 for 30min;* ***C****) HNPs suspension at the end of treatment with SHDS.*

In contrast to the untreated material, LSNPs (**Figure 3.3E**) show a larger concentration of micrometric particles, whereas HNPs (**Figure 3.3H**) show a decrease. Moreover, the size distribution was even assessed by directly incubating the NBMs in the intestinal fluid (**Figure 3.6**).

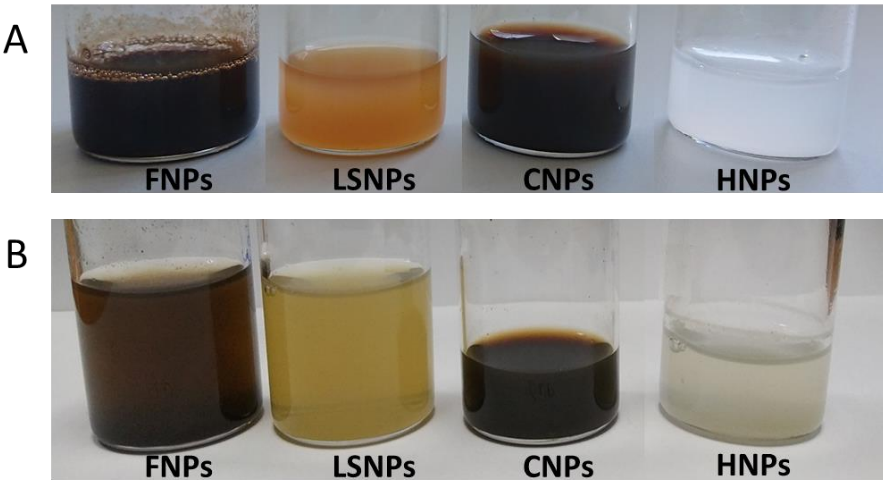

Figure 3.5. Samples *before* ***A****) and after* ***B****) treatment with the SHDS.*

While the suspension in this instance appeared more stable and less aggregated than it did following the SHDS, it is likely that the aggregation took place in the SGF and was permanent for all NBMs.

TEM analysis of the SHDS-treated and untreated NBMs was also performed (**Figure 3.7**).

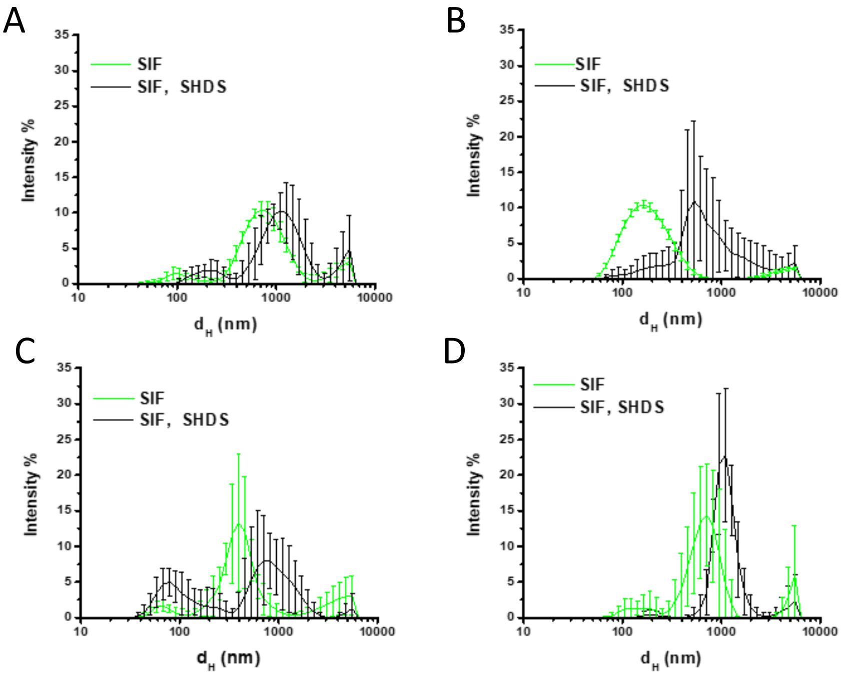

Figure 3.6. ***Size distribution*** *of the samples in SHDS final fluid with and without SHDS process of* ***A****) LSNPs;* ***B****) CNPs,* ***C****) FNPs;* ***D****) HNPs.*

Untreated LSNPs (**Figure 3.7A**) appeared to be made up of different-sized almost-spherical particles, supporting DLS analysis findings (**Figure 3.2A**). The SHDS-treated LSNPs (**Figure 3.7A'**) looked to be degrading and to be smaller in size, but they were arranged into big aggregates that were completely covered in biological material derived from the SHDS fluids.

According to the DLS data, untreated CNPs (**Figure 3.7B**) were spherical, evenly dispersed, and had a narrow size distribution centred around 120 nm, but SHDS treatment lead CNPs (**Figure 3.7B'**) to aggregate and become entangled with biological matter in a manner akin to that of LSNPs (**Figure 3.7A'**).

Figure 3.7C shows untreated FNPs, which look to be made up of tiny, spherical iron oxide particles encased in a PLGA-PEG polymer matrix. Due to the PLGA polymer biodegradable properties [188], the polymer matrix appeared to be eliminated after the SHDS (**Figure 3.7C'**). It was possible to see transparent spherical formations, which could have been caused by the biological matrix or by the polymeric residue that was still present after partial biodegradation. According to the findings of the DLS investigations, the breakdown of polymeric matrix, that confers colloidal stability to the FNPs, caused iron oxide particles highly aggregation (**Figure 3.3C**), while the shape of these particles did not change noticeably.

HNPs were visualised as large particles with a variety of forms, including rods, rectangles, and spheres (**Figure 3.7D**). The instability of the colloidal suspensions and the inconsistent findings in the DLS analysis can both be attributed to this shape/size diversity. Moreover, SHDS-treated HNPs (**Figure 3.7D'**) appear to have undergone a significant morphological change, with clear biological material surrounding them.

Since lipases are able to hydrolyse lipid nanoparticles [189] and LSNPs was found partially degraded in TEM analysis (**Figure 3.7A'**), to prove the involvement of lipase in this process, LSNP was incubated in a solution of lipase in water at the same pH as the intestinal fluid in order to study its susceptibility to enzymatic degradation. The size distribution was tracked for up to 24 h (**Figure 3.8**).

At 15 minutes, there was a change in the hydrodynamic diameter (d_H) distribution toward lower values, indicating degradation (**Figure 3.8A**); after 24 h, the mean d_H value dropped by around 8%. (**Figure 3.8B**).

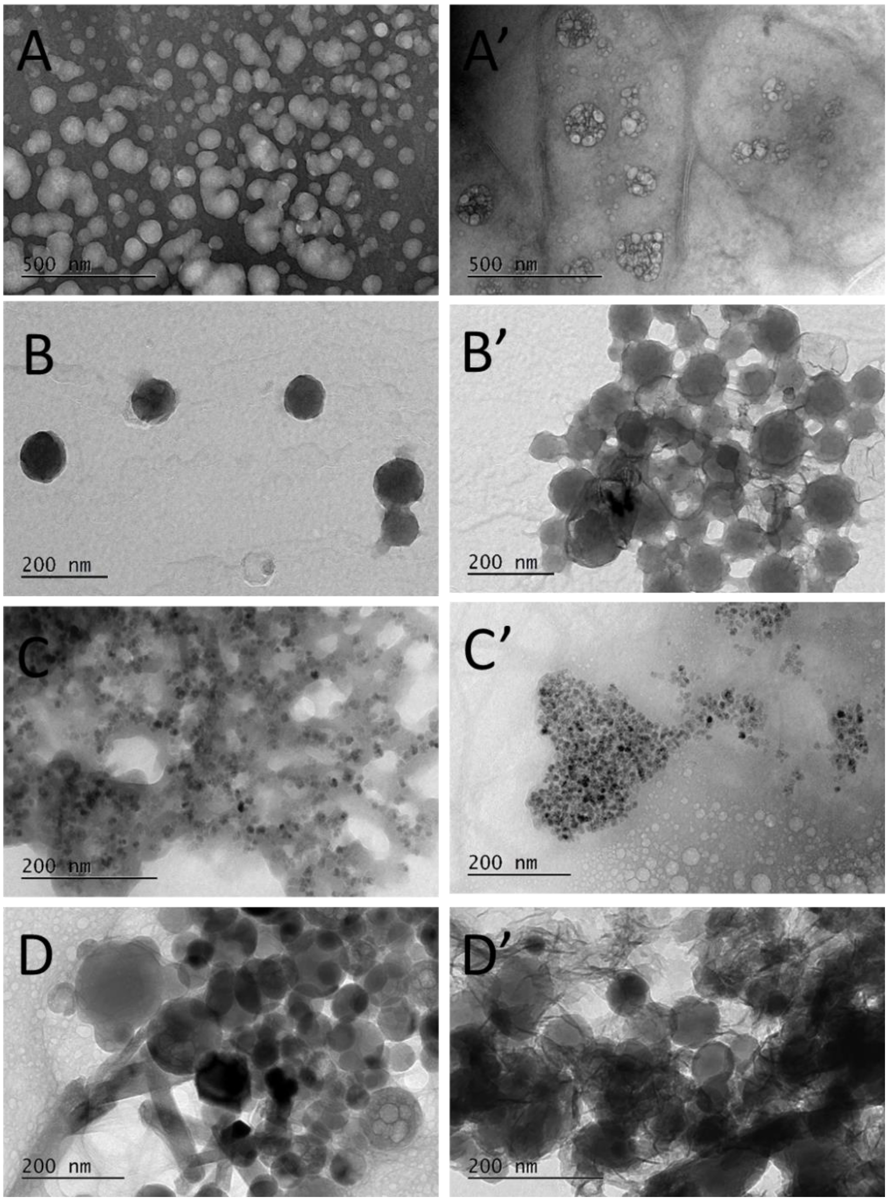

***Figure 3.7. Representative TEM images** of **A**) LSNPs; **B**) CNPs, **C**) FNPs; **D**) HNPs before digestion and **A'**) LSNPs; **B'**) CNPs, **C'**) FNPs; **D'**) HNPs after digestion. Adapted from Antonello et al., 2022* [190].

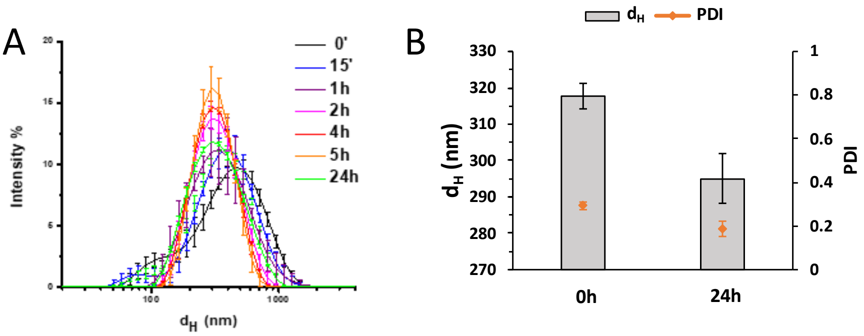

Figure 3.8. LSNPs degradation by lipases. A*) changing in size distribution during the contact of LSNPs with lipase (DLS);* ***B****) mean* d_H *before and after the treatment.*

3.2.3 Bio-molecular corona formation during SHDS

Because of CNPs and FNPs have a surface reactivity that can serve as a probe to measure the amount of surface coverage, the formation of a bio-molecular corona was studied on these NBMs.

The size distribution variations were monitored after performing the SHDS both with and without active components (proteins, enzymes, bile, and uric acid, **Table 3.1**) (**Figure 3.9**).

In comparison to values obtained in fluids with active components, a greater Z-average and PDI value was reported in both SGF and SIF. In addition, the suspensions were largely unstable, and as can be seen in **Figure 3.9**, the particles gradually deposited to the bottom of the flask. This demonstrates that a bio-molecular corona that stabilizes the colloids forms during the SHDS.

The NBMs were examined for their surface reactivity charge by EPR spectroscopy in a bid to determine the extent to which the surface was covered (**Figure 3.10**). After washing procedures designed to get rid of the soft corona, the studies were carried out.

By adjusting the pH of the suspension, the ζ-potential was determined in ultrapure water (**Figure 3.10A and B**). When compared to the untreated CNPs, the ζ-potential curves of the SHDS-treated CNPs were different, indicating the presence of biomolecules on the surface. The loss of the polymeric covering or the presence of a bio-molecular corona could be the cause of the treated FNPs shifting ζ-potential.

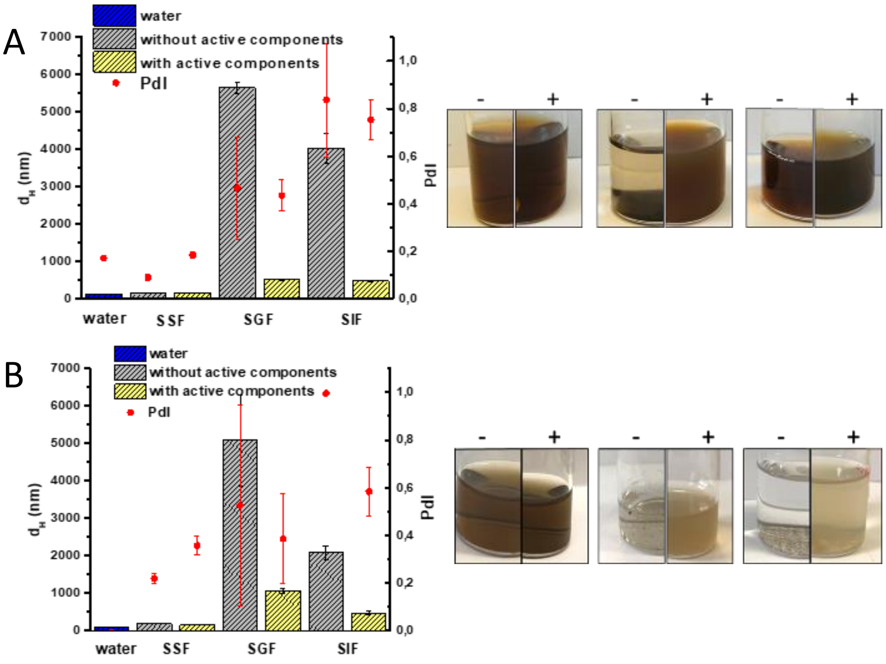

Figure 3.9. Role of proteins. *Mean d_H and PDI (left panels) and images of the suspensions (right panels) of **A**) CNPs; **B**) FNPs; in the various OGI compartments with or without proteins.*

The spin-probe TEMPONE-H was used to measure the surface reactivity. This general probe can react with reactive oxygen species, producing the stable radical TEMPONE that can be detected via EPR spectroscopy [191]. Therefore, it is appropriate to observe the surface reactivity of nanomaterials. The usual three-line signal of the TEMPONE radical could be observed in the presence of untreated CNPs (**Figure 3.10A'**) or FNPs (**Figure 3.10B'**). Both FNPs and CNPs surface reactivity diminished after being exposed to SHDS without completely vanishing, indicating that the solvent was still partially contacting the surface (**Figure 3.10**).

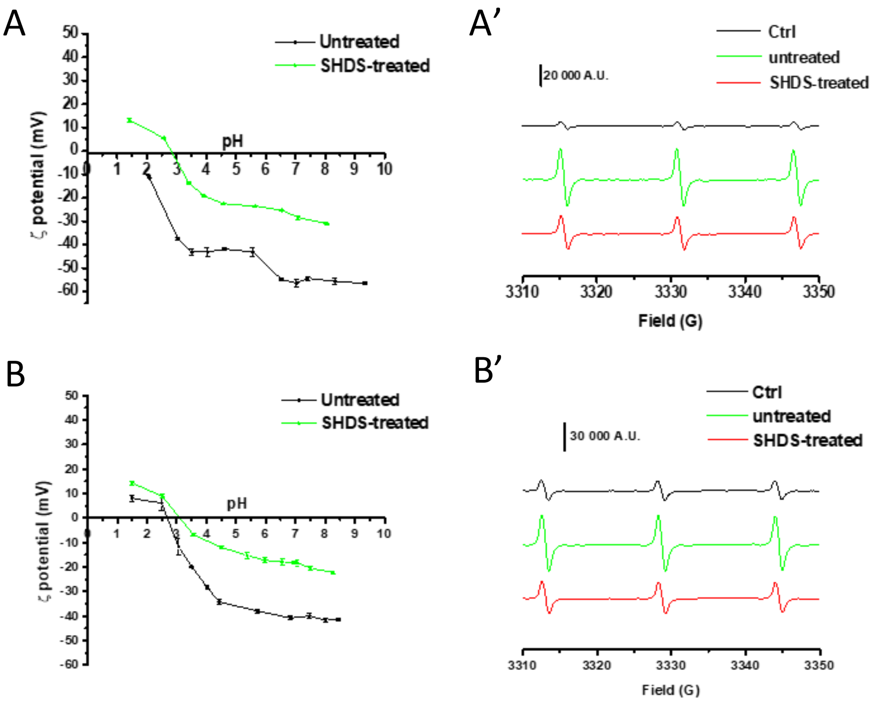

Figure 3.10. Extent of surface coverage and reversibility of the biocorona. *EPR spectra recorded on **A**) CNPs and **B**) FNPs treated with the SHDS in comparison with the pristine one, using spin-probe TEMPONE-OH; ζ-potential vs pH curve of NBMs treated with SHDS with and without proteins and washed (right panels). **A)** CNPs; **B)** FNPs.*

3.2.4 NBMs identity in cell culture medium and in SHDS

Proteins are among the components of cell medium, which is used in *in vitro* cellular testing. The interaction of particles with the medium components during incubation is probably what changes the biological identity of NBMs. First, it was determined how exposure to cell media altered the materials size distribution. **Table 3.4** reports the mean d_H values and PDI.

The size distribution of all NBMs in cell medium underwent an important change after being exposed to the SHDS.

Table 3.4. Mean d_H and PDI of NMs in DMEM+10% FBS (100 mg/ml), 24 h incubation.

Samples	Z-average (nm)	PDI
LSNPs	281.2 ± 9.3	0.418 ± 0.025
LSNPs-SHDS	202.1 ± 5.4	0.613 ± 0,076
CNPs	188.8 ± 2.4	0.083 ± 0.009
CNPs-SHDS	460.0 ± 31.5	0.487 ± 0.032
FNPs	169.8 ± 3.3	0.300 ± 0.039
FNPs-SHDS	849.0 ± 6.6	0.522 ± 0.064
HNPs	653.2 ± 18.6	0.337 ± 0.057
HNPs-SHDS	2435 ± 306	0.841 ± 0.223

The treated LSNPs in the cell medium were more stable over time than the untreated ones (**Figure 3.11A**), but they showed a larger range of sizes, with one population having a mean diameter that was less than that of the LSNPs in water, may be as a result of partial deterioration. Up to 24 h, both treated and untreated CNPs exhibited stability in cell media (**Figure 3.11B**). Nonetheless, a little shift in the sizes toward values greater than those of the particles in water was noted, which was more pronounced for the treated CNPs. Both treated and untreated FNPs (**Figure 3.11C**) and HNPs showed a clear time-dependent instability in cell medium (**Figure 3.11D**). In comparison to water, treated FNPs appear to be extensively aggregated, while untreated FNPs showed a little shift of the curve toward greater d_H.

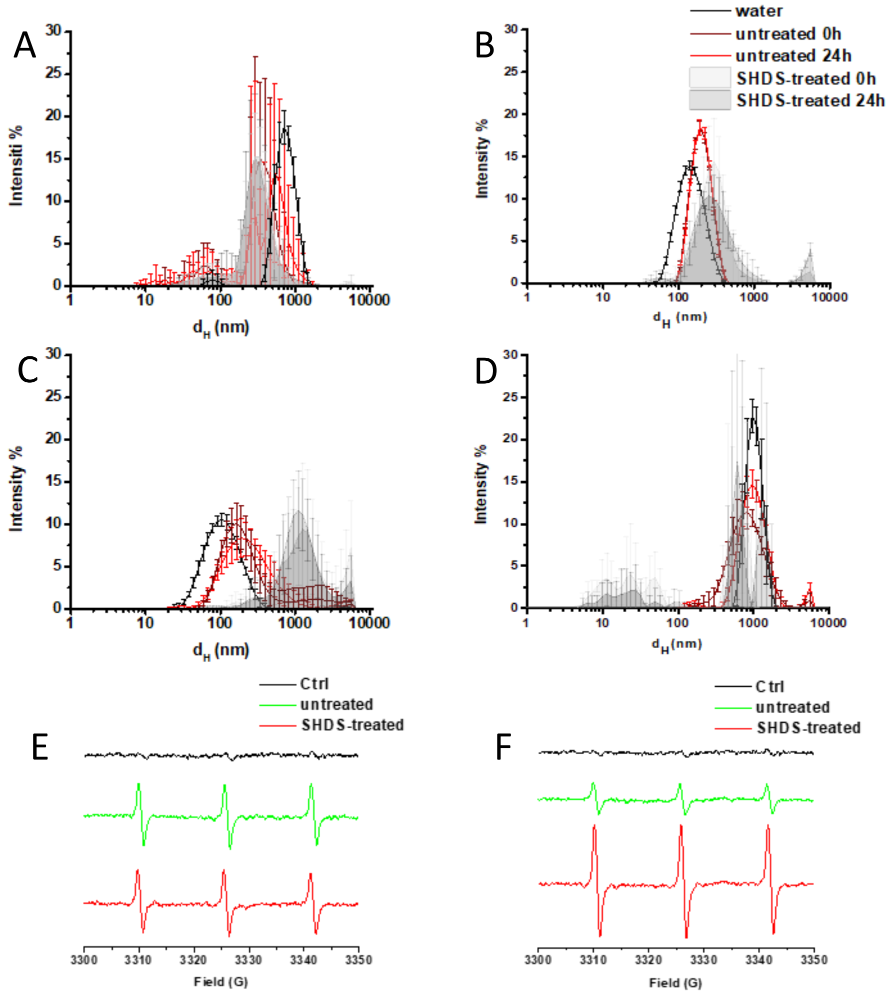

Figure 3.11. NBMs identity in cell media. *Size distribution of the samples in DMEM +10% FBS .* ***A)*** *LSNPs;* ***B)*** *CNPs;* ***C)*** *FNPs;* ***D)*** *HNPs. Representative EPR spectra recorded in a suspension of* ***E)*** *CNPs;* ***F)*** *FNPs pre-incubated in DMEM 10% FBS in the presence of the spin-probe TEMPONE-H.*

Instead, compared to water, untreated HNPs appeared to form slightly more stable colloids in cell medium, on the contrary numerous populations with a wide range of sizes appeared following SHDS. For all NBMs in cell media, the development of aggregates with sizes greater than the DLS detection limit was clearly discernible (**Figure 3.12**).

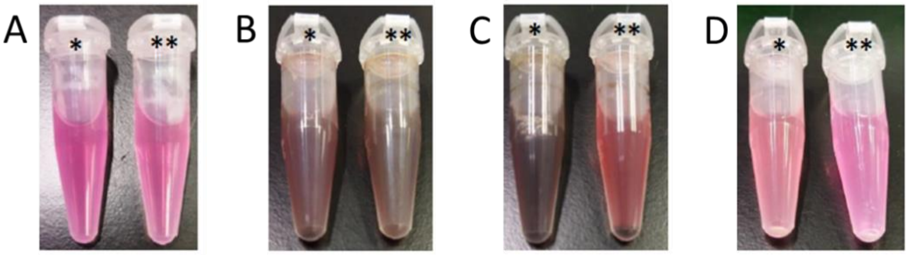

***Figure 3.12. Aspect of the suspension** of the (*) pristine and (**) digested **A)** LSNPs, **B)** CNPs, **C)** FNPs and **D)** HNPs in cell media. Adapted from Antonello et al., 2022* [190].

Using EPR spectroscopy, the surface reactivity of CNPs and FNPs in the cell medium was also determined (**Figure 3.11E and F**). Similar surface reactivity was seen in cell media for both treated and untreated CNPs, indicating that the particle surfaces are still in contact with the solvent as a result of an incomplete covering by the bio-molecular corona. The SHDS-treated sample in the case of FNPs showed an unexpectedly high level of surface reactivity, which may have been caused by the presence of some redox-active elements in the bio-molecular corona.

After incubation in cell medium, the composition of the hard protein corona for treated and untreated NBMs was also examined. Three steps of centrifugation were required to remove the soft corona in order to isolate the corona-NBM complex [192]. With the control sample, which contained only SHDS and DMEM 10% FBS and no NBMs (**Figure 3.13**), a protein background was found, indicating that the prolonged incubation period and the SHDS process caused protein aggregation. However, the NBMs-corona isolation approach did not allow for the separation of the protein corona from the background proteins that co-precipitated. Consequently, we only examined the effects of SHDS treatment for FNPs. In fact, a magnetic separation was used as an alternative technique for these NBMs to eliminate the soft corona.

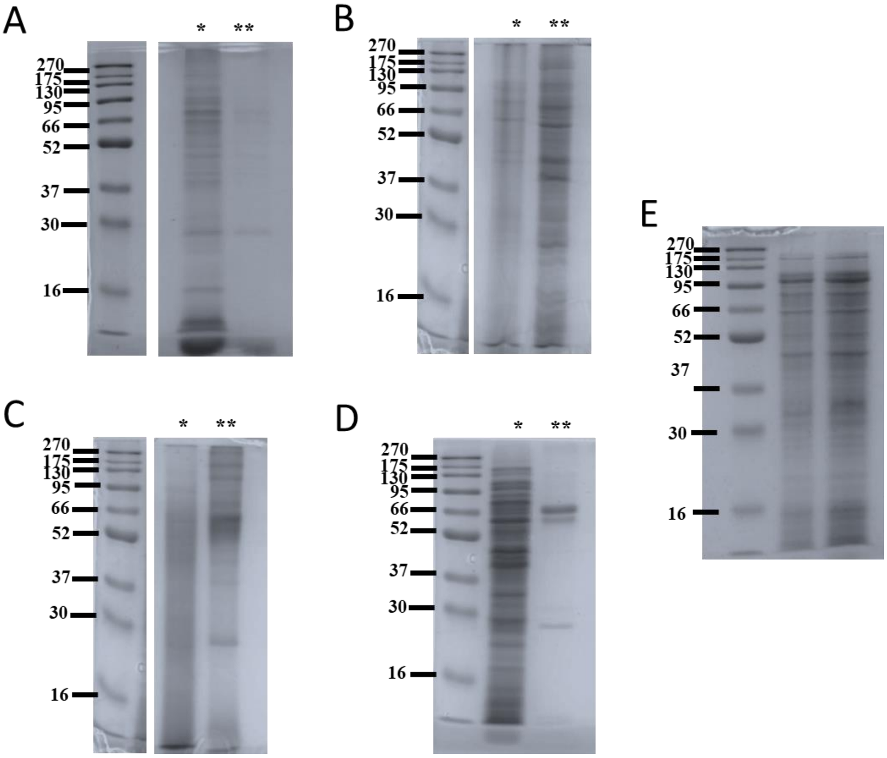

***Figure 3.13**. **SDS-PAGE gel showing the hard corona** of (*) treated and (**) untreated **A)** LSNPs, **B)** CNPs, **C)** FNPs and **D)** HNPs in cell media and obtained by centrifugation, and E) digested solution without NBMs. Adapted from Antonello et al., 2022* [190].

The SDS-PAGE examination of the hard corona is displayed in **Figure 3.14**. As treated and untreated samples show differing protein patterns, it is obvious that the SHDS treatment had an impact on the corona composition.

More than 200 proteins were identified for the corona of both SHDS-treated and untreated FNPs following proteomic mass spectrometric analysis (**Figure 3.14B**).

Tables 3.5 and 3.6 list the top 20 proteins by abundance. The quantity of proteins in the two samples was compared using label free quantification (LFQ) calculations made with Perseus.

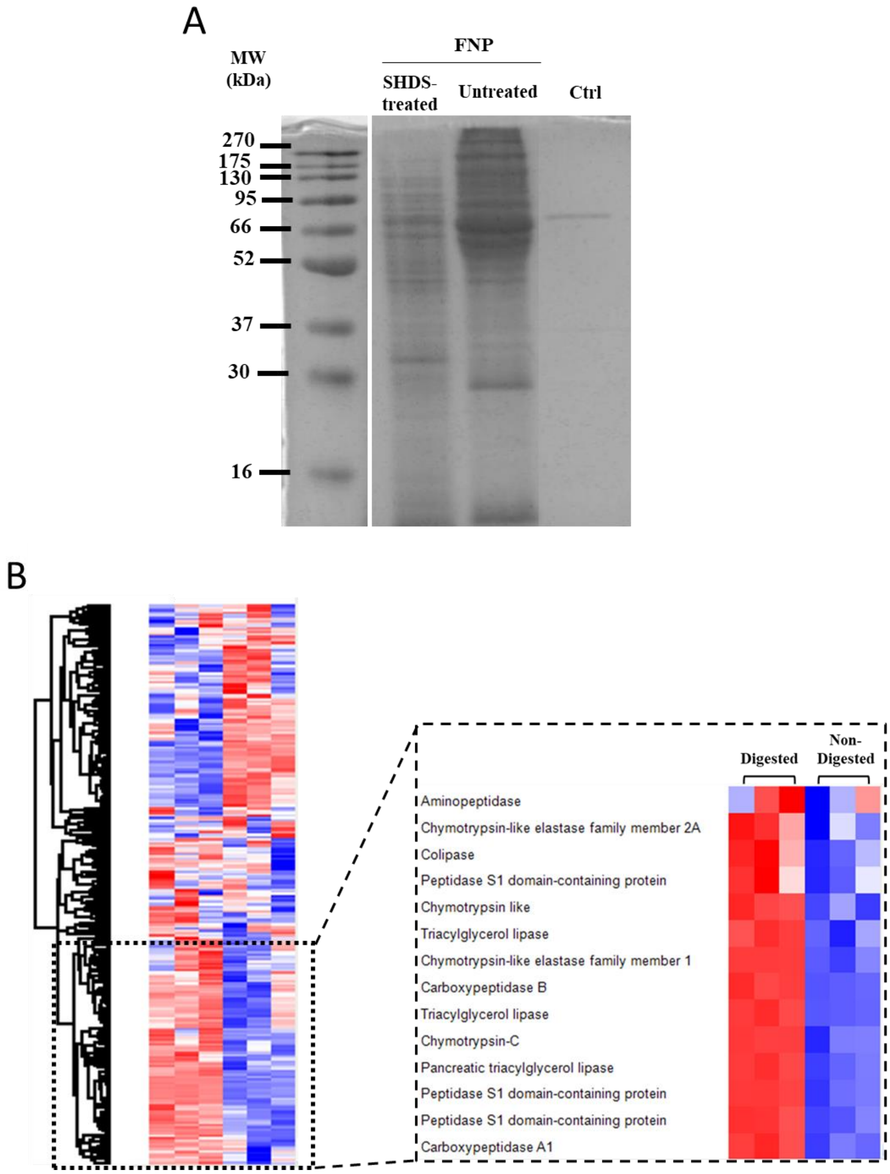

***Figure 3.14**. **Protein corona for FNP** exposure to DMEM+10% FBS for 24 hours, before and after SHDS treatment. **A)** SDS-PAGE. **B)** Heat map showing the relative abundance for every protein normalizing the mean value for the same row (for the same protein). Specific proteins from SHDS are highlighted in the square. Adapted from Antonello et al., 2022* [190].

Table 3.5. *Top 20 most abundant proteins for pristine FNPs. Modified from Antonello et al., 2022* [190].

	FNPs DMEM 10% FBS			
	LFQ ± SEM (x1E08)	**Protein Name**	**Protein ID**	**MW (kDa)**
1	8.11 ± 1.6	Bovine Haemoglobin foetal subunit beta*	P02081	15.9
2	4.81 ± 0.19	Bovine Alpha-1-antiproteinase*	P34955	46.1
3	3.99 ± 0.050	Bovine Alpha-2-HS-glycoprotein*	P12763	38.4
4	3.27 ± 0.34	Bovine Albumin*	P02769	69.3
5	3.22 ± 0.70	Bovine Haemoglobin subunit alpha*	P01966	15.2
6	2.67 ± 0.35	Bovine Apolipoprotein A-I*	P15497	30.3
7	2.45 ± 0.11	Bovine Inter-alpha-trypsin inhibitor heavy chain H2*	A0A3Q1LK49	96.8
8	2.35 ± 0.35	Bovine Angiotensinogen*	P01017	51.4
9	2.04 ± 0.18	Bovine Alpha-fetoprotein*	Q3SZ57	68.6
10	1.90 ± 0.16	Bovine Apolipoprotein A-II*	P81644	11.2
11	1.88 ± 0.14	Bovine Inter-alpha-trypsin inhibitor heavy chain H4	F1MMD7	101.5
12	1.87 ± 0.10	Bovine Alpha-1-microglobulin	F1MMK9	53
13	1.80 ± 0.17	Bovine Beta-2-glycoprotein 1*	P17690	38.3
14	1.54 ± 0.090	Bovine Alpha-2-macroglobulin	Q7SIH1	167.6
15	1.52 ± 0.15	Bovine Fetuin-B	Q58D62	42.7
16	1.46 ± 0.24	Bovine Vitronectin*	Q3ZBS7	53.6
17	1.46 ± 0.037	Bovine Complement C3	Q2UVX4	187.3
18	1.39 ± 0.12	Bovine Alpha-1B-glycoprotein	Q2KJF1	53.6
19	1.28 ± 0.11	Bovine Inter-alpha-trypsin inhibitor heavy chain H3	P56652	99.6
20	1.28 ± 0.11	Bovine Complement factor B	P81187	85.4

*Common proteins; **proteins from SHDS. LFQ was calculated with Perseus (n=3). SEM refer to the standard error of the mean for n=3.

Table 3.6. *Top 20 most abundant proteins for SHDS-treated FNPs. Modified from Antonello et al., 2022* [190].

	SHDS-FNPs + DMEM 10% FBS			
	LFQ ± SEM (x1E08)	**Protein Name**	**Protein ID**	**MW (kDa)**
1	12.4 ± 3.4	Bovine Alpha-2-HS-glycoprotein*	P12763	38.4
2	12.3 ± 1.8	Bovine Alpha-1-antiproteinase*	P34955	46.1
3	10.0 ± 0.90	Pig Peptidase S1 domain-containing protein**	I3LHI7	27.7
4	7.96 ± 0.32	Bovine Albumin*	P02769	69.3
5	6.84 ± 1.1	Bovine Haemoglobin foetal subunit beta*	P02081	15.9
6	4.03 ± 0.60	Bovine Apolipoprotein A-I*	P15497	30.3
7	3.42 ± 0.76	Bovine Histone H2A type 2-C	A1A4R1	14
8	2.45 ± 0.24	Bovine Haemoglobin subunit alpha*	P01966	15.2
9	2.43 ± 0.35	Pig Triacylglycerol lipase**	F1S4T9	51.6
10	2.42 ± 0.35	Pig HATPase_c domain-containing protein**	A0A287A9T4	83
11	2.32 ± 0.57	Bovine Serpin family G member 1	E1BMJ0	51.8
12	2.26 ± 0.42	Pig Carboxypeptidase A1**	P09954	47.2
13	2.02 ± 0.80	Bovine Angiotensinogen*	P01017	51.4
14	2.00 ± 0.13	Bovine Alpha-fetoprotein*	Q3SZ57	68.6
15	1.61 ± 0.85	Bovine Histone H2A	F2Z4G5	14.1
16	1.58 ± 0.10	Bovine Beta-2-glycoprotein 1*	P17690	38.3
17	1.58 ± 0.10	Bovine Inter-alpha-trypsin inhibitor heavy chain H2*	A0A3Q1LK49	96.8
18	1.39 ± 0.16	Bovine Apolipoprotein A-II*	P81644	11.2
19	1.30 ± 0.19	Pig Peptidase S1 domain-containing protein**	I3LJ52	26.9
20	1.14 ± 1.7	Bovine Vitronectin*	Q3ZBS7	53.6

*Common proteins; **proteins from SHDS. LFQ was calculated with Perseus (n=3). SEM refer to the standard error of the mean for n=3.

Several serine proteases from SHDS were detected in the top 20 most prevalent for the treated sample. The corona of both samples, however, included proteins that were noted for being abundant on the FBS [193], particularly alpha-2-HS-glycoprotein, apolipoprotein AI and AII, bovine haemoglobin alpha and beta chains, and alpha-1-antiproteinase. The latter is a serine protease inhibitor known as alpha-1-antiproteinase, alpha-1-antitrypsin, alpha-1-proteinase inhibitor, or serpin A1. **Figure 3.15** compares the protease concentrations in treated and untreated samples.

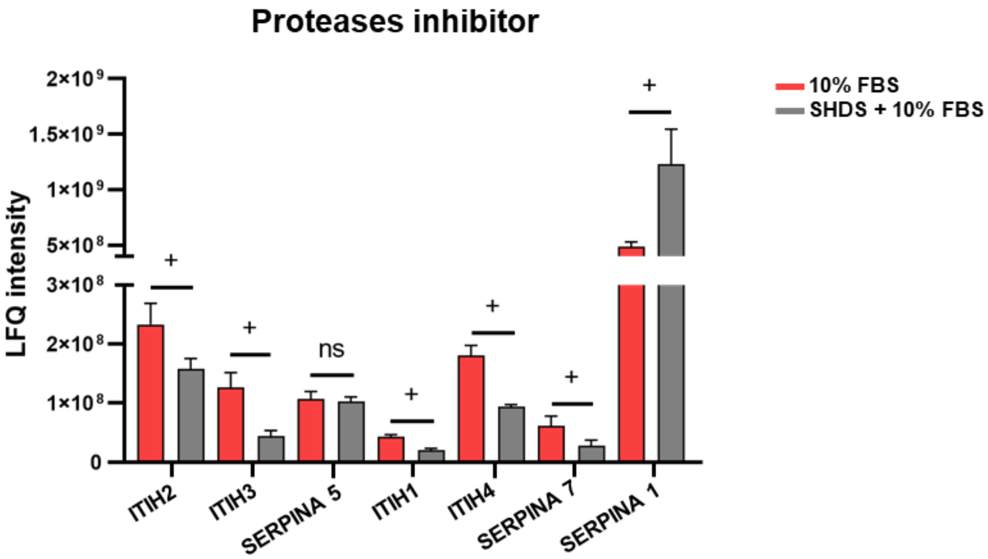

Figure 3.15**.** ***LFQ intensity*** *for different proteases inhibitor for FNPs non-treated and pre-treated with SHDS. n=3; +p<0.05. ITIH2***:*** *Inter-alpha-trypsin inhibitor heavy chain H2; ITIH3: Inter-alpha-trypsin inhibitor heavy chain H3; SERPINA 5: Plasma serine protease inhibitor; ITIH1: Inter-alpha-trypsin inhibitor heavy chain H1; ITHI4: Inter-alpha-trypsin inhibitor heavy chain H4; SERPINA 7: Serpin peptidase inhibitor, clade A (Alpha-1 antiproteinase, antitrypsin), member 7; SERPINA 1: Alpha-1-antiproteinase. Edited from Antonello et al., 2022* [190].

3.2.5 Effects of SHDS on the viability of epithelial intestinal Caco-2 cells, HCT116 cells and primary Human Colonic Epithelial cells

A dose-dependent viability experiment employing a dose range of 0 to 150 g/ml was carried out on Caco-2 and HCT116 cells to investigate the effect of

SHDS treatment on the NBMs biocompatibility/cytotoxicity. This range was determined by the toxicity of OGI fluids tested separately at the same dilutions as those used to dilute NBMs, which showed that OGI fluids are not significantly cytotoxic up to dilution equivalent to 150 g/ml NBMs (**Figure 3.16A**).

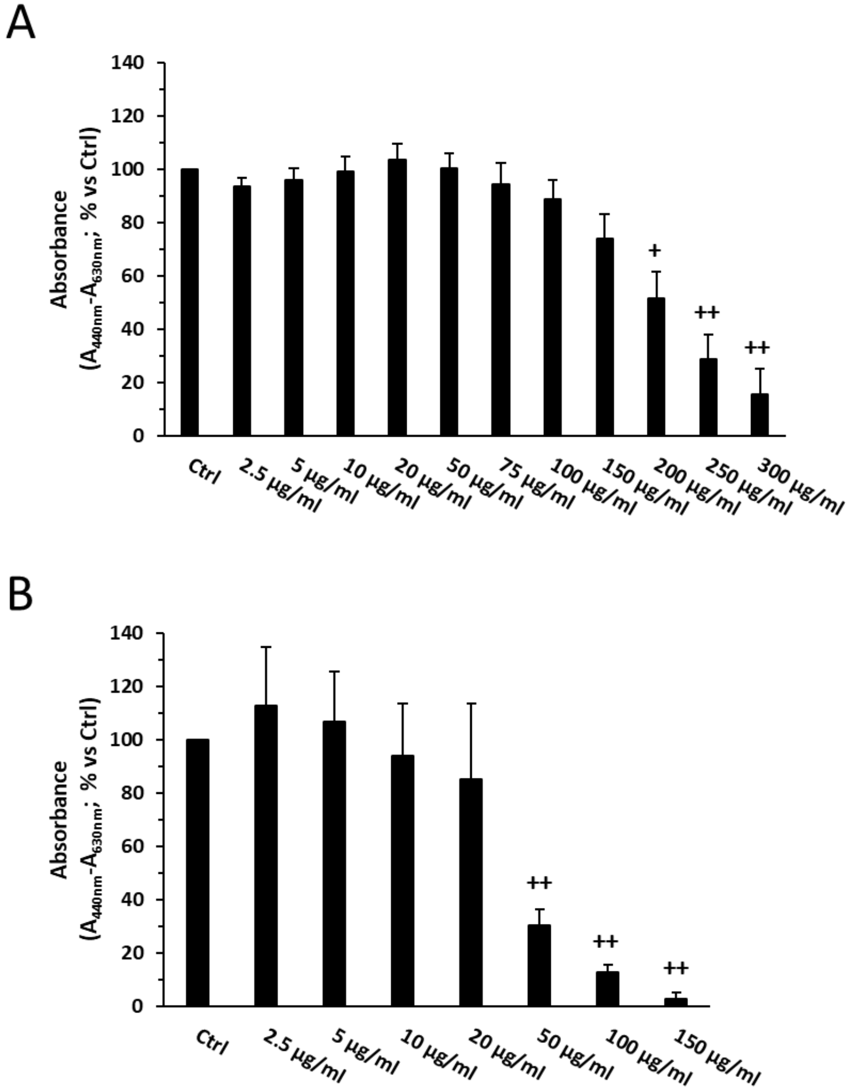

***Figure 3.16. Cells viability** of **A)** Caco-2 cells and **B)** HCoEpiC cells after 24h of incubation with OGI fluids.*
n=3
+p<0.05 vs Ctrl; ++p<0.01 vs Ctrl

Untreated LSNPs up to 100 µg/ml showed very minimal toxicity in Caco-2 and HCT116 cells. However, following SHDS treatment, both Caco-2 and HCT116 cells showed considerable cytotoxicity for doses greater than 75 µg/ml and 20 µg/ml, respectively (**Figure 3.17A**). Contrarily, neither the untreated nor the SHDS-treated CNPs were toxic, and SHDS had no effect on the biocompatibility profile of this NBM in both the two cell lines (**Figure 3.17B**). Untreated FNPs showed the maximum level of cytotoxicity on Caco-2 cells, starting to exert toxicity at 10 µg/ml, but SHDS, in contrast to the other NBMs, had a cytoprotective effect. In fact, treated FNPs became toxic at 75 µg/ml (**Figure 3.17C**). For HNPs, a similar effect of toxicity masking was seen; while untreated HNPs exhibited toxicity starting at 50 µg/ml, treated HNPs did not exhibit toxicity at any of the concentrations examined (**Figure 3.17D**). Neither untreated nor SHDS-treated FNPs and HNPs significantly produced cytotoxicity in HCT116 cells (**Figure 3.17C and D**).

Models of gastrointestinal cells like Caco-2 and HCT116 are frequently employed [194]. However, because they are immortalized, they should be less susceptible to outside stimuli. For this reason, we also evaluated the impact of NBMs in primary non-transformed intestinal epithelial cells (HCoEpiC). All the NBMs, in general, demonstrated toxicity at lower doses than on Caco-2 and HCT116 cells (**Figure 3.18**). The higher susceptibility of HCoEpiC to SHDS fluids, which are toxic at lower concentrations (50 µg/ml) than in immortalized cells (**Figure 3.16B**), can help to explain this finding. Taking this into account, we chose to analyse the NBMs in a concentration range (2.5–20 µg/ml) that was just below the first toxic concentration of SHDS fluids.

HNPs were the only NBM that demonstrated a lower cytotoxicity after SHDS towards both Caco-2 (**Figure 3.17D**) and HCoEpiC cells (**Figure 3.18D**). SHDS treatment increased the cytotoxicity of LSNPs and CNPs (**Figure 3.18A and B**), while there was no observable cytotoxicity difference between SHDS-treated and untreated FNPs (**Figure 3.18C**) (**Figure 3.18D**).

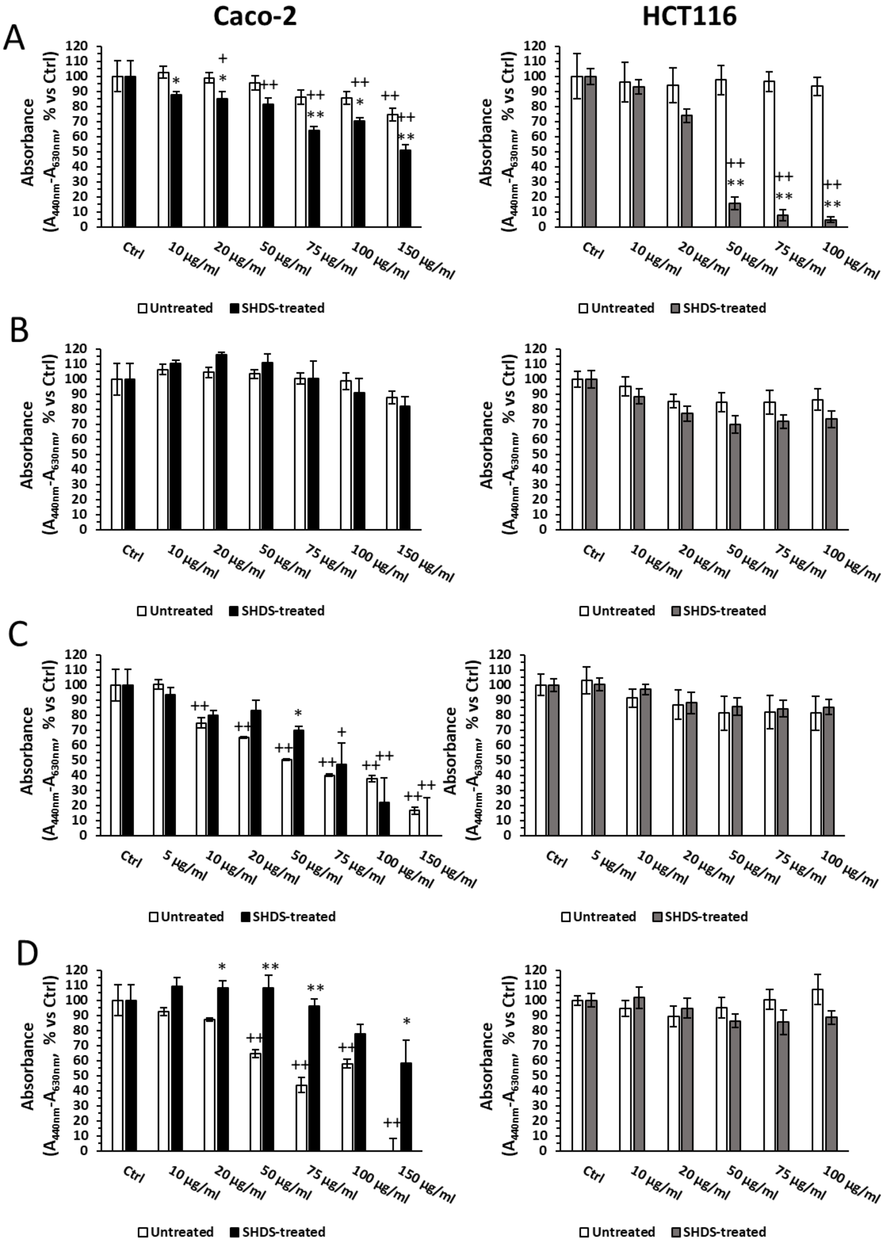

Figure 3.17. Cells viability *of Caco-2 (in black) and HCT116 (in gray) cells after incubation with pristine and SHDS-treated* ***A)*** *LSNPs ,* ***B)*** *CNPs,* ***C)*** *FNPs and* ***D)*** *HNPs. +p<0.05 vs Ctrl, ++p<0.01 vs Ctrl; *p<0.05 vs pristine; **p<0.01 vs pristine. Adapted from Antonello et al., 2022* [190].

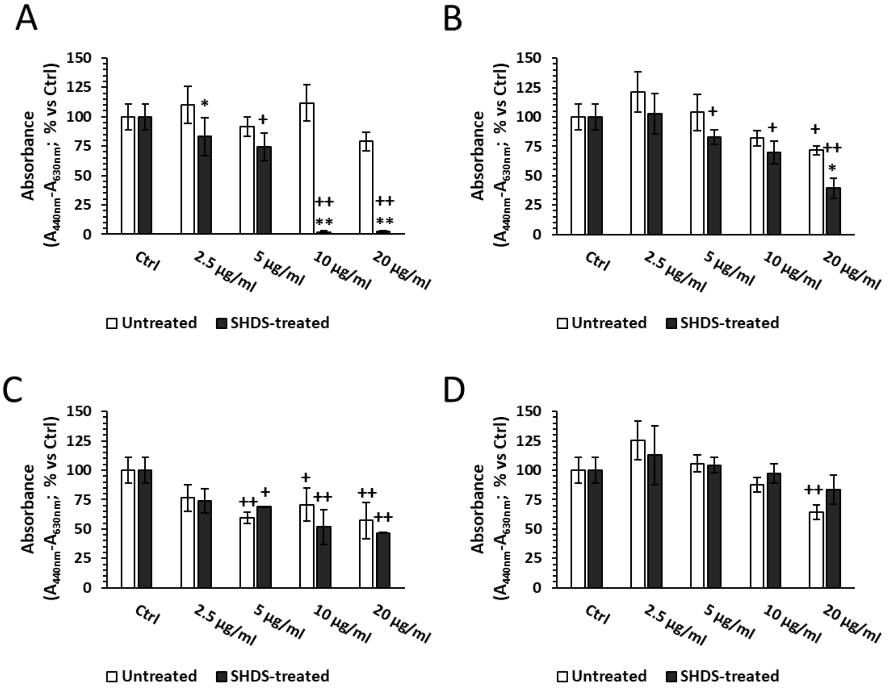

***Figure 3.18**. HCoEpiC viability after incubation with pristine and SHDS-treated **A)** LSNPs, **B)** CNPs, **C)** FNPs and **D)** HNPs. +$p<0.05$ vs Ctrl, ++$p<0.01$ vs Ctrl; *$p<0.05$ vs pristine; **$p<0.01$ vs pristine.*

These findings indicate that the nature of NBMs, which can go through various alterations throughout SHDS, has an impact on the behaviour of epithelial intestine cells. Furthermore, the selection of an *in vitro* model to assess cytotoxicity is crucial, as shown by the disparate sensitivity of Caco-2 cells, HCT116 cells, and primary non-transformed cells.

Subsequently, HCT116 cells were used to test the genotoxicity of NBMs that, although being a cancer-derived cell line, contain wild-type p53 as opposed to Caco-2 cells. Counting 53BP1 DNA repair foci revealed that none of the tested NBMs increased the number of DNA strand breaks in a manner that was statistically different from the positive control, which consisted of cells treated for 24 h to 50 µM etoposide (**Figure 3.19**).

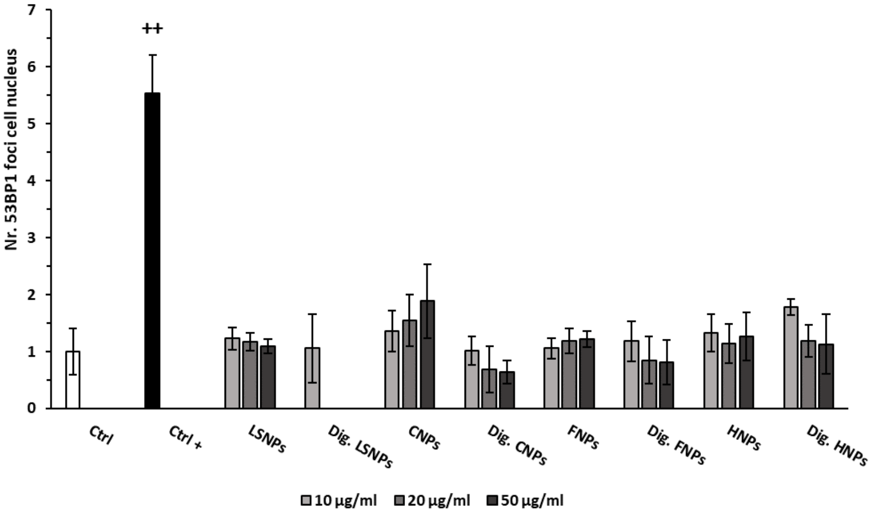

Figure 3.19. NM genotoxicity. *DNA strand breaks were quantified using 53BP1 immunostaining and foci counts, each focus reflecting the presence of a DNA double strand break. HCT116 were exposed for 24 h to 10, 20 or 50 µg/mL of FNP, CNP, LSNP or HNP NMs, either pristine or digested, except for the digested form of LSNP, which was tested only at 10 µg/mL due to cytotoxicity higher than 30% at the two other concentrations. Positive control: HCT116 cells exposed for 24 h to etoposide (black bar). Only the positive control significantly increases the nr. of 53BP1 foci.*
+p<0.05 vs Ctrl; ++p<0.01 vs Ctrl
Adapted from Antonello et al., 2022 [190].

3.2.6 Effects of SHDS on viability and permeability of Caco-2 intestinal barrier model

Lastly, using the 21-day differentiated Caco-2 model, we examined the impact of NBMs on viability, permeability, and inflammatory parameters in a reliable intestinal barrier model.

Caco-2 cells start differentiating after 21 days, when they have reached complete confluence after growing on porous membrane inserts [149]. Because it replicates intestinal physiology, this model is accepted as a reliable representation of the intestinal barrier and is frequently employed in permeability evaluation tests [195,196]. Hence, for all SHDS-treated and untreated NBMs, we examined the effects on cell viability and barrier permeability using this model. In order to highlight the differences in terms of the toxicological features of NBMs, before and after the simulated digestive process, we decided to analyse the greatest non-toxic dose of NBMs obtained *in vitro* on Caco-2 undifferentiated cells. This is because there is no published data about the physiological doses in patients exposed to these NBMs, but there are also no reports of severe acute toxicity. The greatest concentration of SHDS-treated NBMs (150 g/ml for CNPs and HNPs, 50 g/ml for LSNPs and FNPs) that did not significantly cause toxicity in undifferentiated Caco-2 cells were therefore used to incubate barrier-forming cells for 24 hours (**Figure 3.17, left panel**).

Neither untreated nor SHDS-treated NBMs displayed toxicity in the viability assays (**Figure 3.20A**).

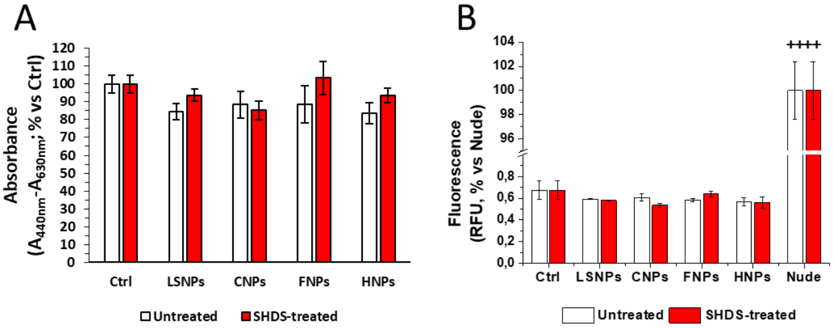

Figure 3.20. Caco-2 barrier A) viability and B) permeability*. +p<0.05 vs Ctrl, ++p<0.01 vs Ctrl; *p<0.05 vs pristine; **p<0.01 vs pristine.*

As NBMs toxicity may affect barrier integrity and cause inflammation [197], we then assessed integrity measures in terms of functional assays, TEER and TJ levels, and the production of pro- and anti-inflammatory cytokines.

In our model, the absence of permeability fluctuation, as determined by the LY permeability assay, was paralleled by the absence of toxicity (**Table 3.7**, **Figure 3.20B**). Additionally, in both untreated and NBM-treated barriers, the TEER values were always greater than 600 Ωcm^2 (**Table 3.8**).

Table 3.7. *Apparent permeability (Papp) values of Caco-2 barrier model after 24 h of incubation.*

	Untreated Papp (cm/s)	**SHDS-treated Papp (cm/s)**
Ctrl	$2.61 \times 10^{-7} \pm 2.71 \times 10^{-8}$	$2.67 \times 10^{-7} \pm 1.40 \times 10^{-8}$
LSNPs	$2.32 \times 10^{-7} \pm 5.60 \times 10^{-9}$	$2.26 \times 10^{-7} \pm 3.20 \times 10^{-9}$
CNPs	$2.38 \times 10^{-7} \pm 1.83 \times 10^{-8}$	$2.09 \times 10^{-7} \pm 3.37 \times 10^{-9}$
FNPs	$2.29 \times 10^{-7} \pm 1.08 \times 10^{-8}$	$2.50 \times 10^{-7} \pm 1.35 \times 10^{-8}$
HNPs	$2.21 \times 10^{-7} \pm 9.92 \times 10^{-9}$	$2.18 \times 10^{-7} \pm 1.45 \times 10^{-8}$

24 h of incubation with 50 µg/ml of LSNPs and FNPs, and 150 µg/ml of CNPs and HNPs. n=3; mean+/-SEM.

Table 3.8*. Trans-Epithelial Electrical Resistance (TEER) values of Caco-2 barrier model after 24 h of incubation.*

	Untreated TEER (Ω*cm^2)	**SHDS-treated TEER (Ω*cm^2)**
Ctrl	619.5 ± 44.2	657.3 ± 25.3
LSNPs	642.3 ± 31.7	661.5 ± 21.2
CNPs	674.1 ± 53.4	632 ± 23.1
FNPs	665.7 ± 37.8	653.2 ± 24.9
HNPs	623.7 ± 19.2	642.5 ± 23.6

Importantly, each NBM displayed a distinct pattern of upregulation of one or more TJ-related genes (**Figure 3.21**). Untreated LSNPs, FNPs, and HNPs downregulate the occludin encoding gene (OCLN) (**Figure 3.21B**), as well as the zonula occludens-1 (TJP1), claudin 3 (CLDN3), and claudin 5 (CLDN5) encoding genes, to a lesser extent (**Figure 3.21D**). Only TJP1 and CLDN5 expression was increased by SHDS-treated LSNPs, TJP1, OCLN, and CLDN5 expression was increased by SHDS-treated FNPs, and all these genes expression was enhanced—albeit to varying degrees—by SHDS-treated HNPs. It is interesting to note that CNPs were the only NBM to stimulate the expression of all TJs-encoding genes examined, in both the untreated (apart from CLDN5) and the SHDS-treated forms (**Figure 3.21**).

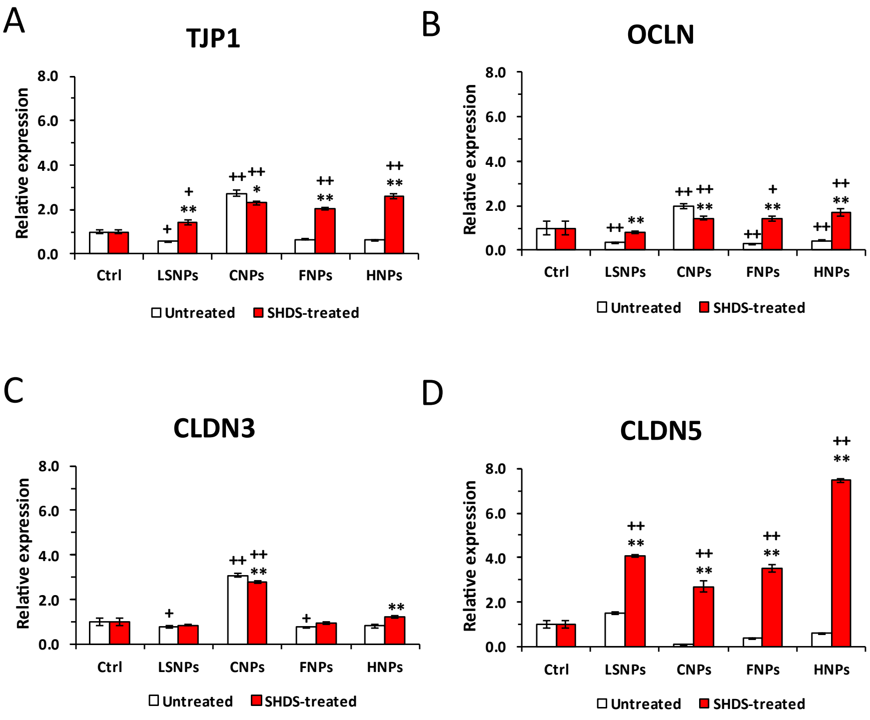

Figure 3.21. Tight junction proteins gene expression *in Caco-2 barrier model after incubation with NBMs* ***A)*** *TJP1 ,* ***B)*** *OCLN,* ***C)*** *CLDN3 and* ***D)*** *CLDN5. +p<0.05 vs Ctrl, ++p<0.01 vs Ctrl; *p<0.05 vs pristine; **p<0.01 vs pristine.*

The upregulation of TJs genes may indicate that intestinal cells generated a compensatory response in reaction to potentially cytotoxic NBMs. The functional outcome in terms of permeability (**Figure 3.20B**) indicates that this reaction was successful in preventing the deterioration of barrier integrity.

The gene expression of two pro-inflammatory cytokines involved in the pathogenesis of inflammatory bowel disease, TNF-α and IL-6 [198], was also examined. These cytokines were contrasted to IL-10, which is known for its role in reducing inflammation in inflammatory bowel disease [199], and IL-22, which promotes intestinal regeneration after injuries [200] and maintains the integrity of the intestinal epithelium [201].

None of the untreated NBMs significantly raised the expression of the cytokines genes (**Figure 3.22**), which is consistent with the low influence TJ-genes were subjected to (**Figure 3.21**).

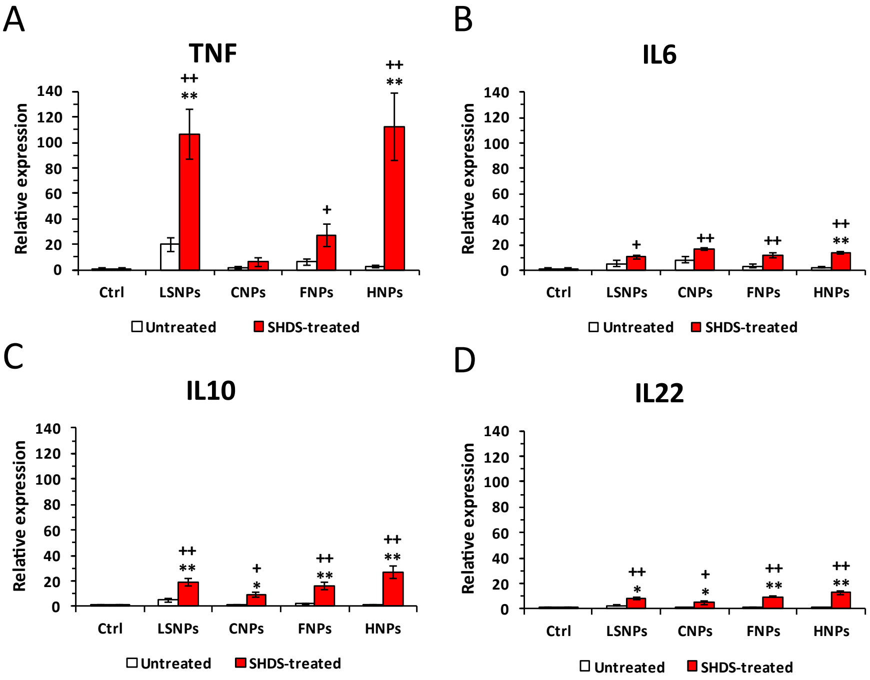

***Figure 3.22. Inflammation-related gene expression** in Caco-2 barrier model after incubation with NBMs **A)** TNF , **B)** IL6, **C)** IL10 and **D)** IL22. +p<0.05 vs Ctrl, ++p<0.01 vs Ctrl; *p<0.05 vs pristine; **p<0.01 vs pristine.*

The expression of the pro-inflammatory TNF-α encoding gene was raised by SHDS-treated LSNPs, FNPs, and HNPs but not by SHDS-treated CNPs (**Figure 3.22A**). All the SHDS-treated NBMs upregulated the IL-6 encoding gene (**Figure 3.22B**), but they also upregulated the IL-10 and IL-22 encoding genes, two anti-inflammatory/immune-suppressive cytokines, suggesting a balance between pro-inflammatory and anti-inflammatory processes that may help to maintain the integrity of the intestinal barrier.

3.2.7 NBM intestinal barrier crossing

The LY test results indicated that the studied NBMs, in both their pristine and treated forms, are unable to pass the barrier by paracellular translocation. The model was treated with CNPs and FNPs, and NTA was used to track the particle concentration in the Bl compartment of the Caco-2 barrier in order to monitor any potential transcellular translocation. These samples were chosen because high refractive index samples are more suitable for the procedure. After treatment with both pristine and SHDS-treated CNPs and FNPs, no particles were discovered in the Bl compartment, indicating that, based on their minimal detectable concentration, the absorption through the barrier is less than 1.25 and 2.5%, respectively, of the Ap concentration for pristine ones, and 2% and 25%, respectively, for digested ones. These findings were verified for FNPs using the FerroZine™ assay, which demonstrated that neither untreated nor treated samples contained detectable iron corresponding to concentrations greater than 1.25% of the Ap concentration.

All the results contained in this chapter are summarized in **Table 3.9**.

Table 3.9. *Resume of the results of Chapter 3.*

Endpoint	Results
Properties of NBMs	NBMs with different chemical nature differ from each other by size distribution and surface charge
Effect of SHDS on NBMs size	After SHDS treatment all NBMs tested showed a micrometric fraction, a biological coating and appeared aggregated. HNPs and LSNPs were partially degraded from acidic pH and lipase respectively
Bio-molecular corona formation during SHDS	After SHDS, CNPs and FNPs appeared more stable and acquired different surface charge and reactivity as compared to pristine particles
NBMs identity in cell culture medium and in SHDS	In cell culture medium, both pristine and SHDS-treated particles showed different hydrodynamic diameter, size distribution, stability, and surface reactivity than particles in water or dispersant. FNPs presented on the surface bovine serum proteins and proteins from SHDS fluids
Effects of SHDS on the viability of intestinal cells	The particles had different effects on cell viability on Caco-2, HCT116 and HCoEpiC cells. HCoEpiC were the more sensible cells as they are primary cells. No genotoxicity was found for all particles tested on HCT116 cells
Effects of SHDS on Caco-2 intestinal barrier model	No change in viability, permeability, and integrity of the barrier for all particles tested. Different particles and SHDS-treated particles showed different trends of regulation of TJs-associated genes. Only SHDS-treated particles up-regulated inflammation-related genes
NBM intestinal barrier crossing	No detectable barrier crossing was found for CNPs and FNPs

3.3 Discussion

Nanomaterial exposure is growing more and more likely as a result of the extensive use in numerous industrial sectors, including the food and pharmaceutical industries. As a consequence, the number of studies examining the risk posed by NBMs is growing dramatically [202–204]. Despite being an important route of exposure to both NMs and NBMs, ingestion has received little attention thus far. This is probably due to the complexity of the physiology of the OGI tract and the absence of models and markers of NBMs toxicity.

To better simulate the complex gut structure and physiology, several alternative cellular models have recently been proposed [153,154,205–208]. However, the majority of current studies only expose cells to pristine NBMs, omitting the changes that they go through along the OGI tract [209]. To detect such biotransformation, many *in vitro* digestion-simulating systems have recently been proposed [144,210,211]. The impact of the biotransformation throughout the OGI tract on the toxicity of nanomaterials against intestinal cells, however, has received very little attention [94,212–215] although lately the interest on this topic is rising with the contribution of some studies [216,217].

Here we reveal that the bioactivity of NBMs towards intestinal epithelial cells is significantly altered by the application of a SHDS, which in turn depends on the chemical nature of the NBMs.

3.3.1 NBMs acquire a new identity in the OGI tract

The fact that the physical and chemical characteristics of NBMs, such as size and surface properties, greatly influence their bioactivity, like toxicity, is currently well established [218–220].

Size mostly influences cellular uptake and dosimetry. In fact, smaller particles can enter cells more easily via diffusion through the cell membrane or active processes like caveolae- and clathrin-mediated endocytosis [221]. The kinetics of interaction with cells and the effective dose, on the other hand, are modified by size because it influences particle sedimentation and diffusion [222,223].

Several different types of NBMs, including lipid nanoparticles [224], silver nanoparticles [225,226], titanium dioxide nanoparticles [94,227], silica nanoparticles [228], amorphous magnesium-calcium phosphate nanoparticles [229], gold nanoparticles [230], and others [231,232], have been shown to aggregate or agglomerate after interacting with simulated gastric or intestinal fluids. As the size of the four NBMs under investigation has significantly increased (**Figures 3.3**), our study supports earlier reports. Regardless of the chemical nature of the NBMs, this process, which primarily takes place in the stomach compartment, is irreversible. All NBMs actually look aggregated in cell medium, and in these forms, they have a higher possibility of interacting with the intestinal cells *in vivo*. As shown for stable zero-valent iron [233], gold [234], and silver nanoparticles [235][235], the stomach fluid low pH and high ionic strength appear to be the primary driving forces for aggregation, whereas the proteins appear to impede the process only partially.

NBMs go through other transformational processes besides aggregation. Since dissolution, enzymatic degradation, or coating degradation were observed, it appears that HNPs, LSNPs and FNPs aggregates are made up of transformed primary particles that are smaller than the original ones. This finding is in line with other investigations that have shown that extremely acidic pH can dissolve pH-sensitive NBMs [234–236] and that enzymes and proteins can contribute to NBMs dissolution by breaking down their components [237–240].

The alteration of the NBMs surface chemistry is a crucial factor. Both colloidal stability and interaction of nanoparticles with membranes are impacted by surface charge [241–243]. The NBMs surface, on the other hand, works as a scaffold for protein and biomolecules binding, resulting in the acquisition of a biological identity [244–248] that appears to determine NBMs affinity for certain cell types and particular receptors [221,249]. The specific bio-fluid in which NBMs are dispersed has a significant impact on the content of the bio-corona and subsequent NBMs activity [250–253].

Our research clearly reveals that proteins and other components form a hard corona to establish an irreversible bond to the surface. There were noticeable variations between FNPs that had not been pre-treated with the SHDS and FNPs that had. A protein coating actually forms around the hydroxyapatite nanoparticles, delaying their degradation, as previously shown by Choki and colleagues, who also noted the protective role of proteins [254]. A diminished release of Ag^+ ions from silver nanoparticles when coated with bovine serum albumin has also been shown by Levak and co-workers and Martin and colleagues [255,256]. Yet, the protein corona alters the surface charge of CNPs and FNPs while only partially inhibiting their surface reactivity. This finding indicates that the particle surfaces may still be partially exposed to the solvent and able to interact directly with cell surface. The nature of the materials has an impact on this effect. In fact, we have already reported that the treatment with SHDS fully suppressed the surface reactivity in the case of TiO_2 [94].

3.3.2 Effect of the biotransformation on the toxicity of NBMs toward intestinal cells

The treatment with SHDS had a significant impact on how NBMs interacted with Caco-2 cells. Yet, the outcome varies based on the NBMs type and model/endpoint. The treatment increased the toxicity of LSNPs toward undifferentiated Caco-2 cells, most likely due to the release of the surfactant generated by the outermost layers breakdown induced by the SHDS (**Figure 3.17**), but not of CNPs, and decreased the cytotoxicity of FNPs and HNPs. The pattern in primary intestinal epithelial cells was distinct. In this instance, SHDS increased the toxicity of CNPs and FNPs while maintaining a toxicity trend similar to Caco-2 cells for LSNPs and HNPs (**Figure 3.18**). This result is consistent with that of other non-transformed cell lines, such as CCD-841, which demonstrated a greater drop in viability following treatment with silicon nanoparticles with isothiocyanate caps than Caco-2 cells [257]. Nevertheless, the literature does not report any specific mechanism of increasing sensitivity to NBMs in specific cell types, thus we cannot exclude induced variations other than inflammation and cell viability loss, such as affection of cellular ultrastructure (e.g., cytoskeleton rearrangement, TJs perturbation). However, our findings indicate that the use of primary epithelial cells helps in obtaining a more comprehensive understanding of the effects of NBMs in humans: by combining the findings from immortalized cells, which are by nature useful for preliminary and extensive screening, with the findings from a model more resembling the physiological cells found in the human OGI tract, more accurate information about the NBM biocompatibility arise.

Interestingly, while all NBMs clearly perturbed the TJs, neither treated nor pristine NBMs were cytotoxic in the differentiated Caco-2 cells or changed the permeability of the intestinal barrier. This could be seen as a compensatory mechanism, as it happens in various diseases [258] or in response to IL-10, a cytokine whose expression is increased by the NBMs in our model, known to preserve the integrity of the intestinal barrier [259]. In order to limit the damage induced by NBMs, intestinal cells likely respond by increasing specific genes encoding for the main TJ proteins, preventing the loss of TJs, and maintaining the barrier intact. While it is true that the pro-inflammatory cytokines TNF-α and IL-6, which are also stimulated by NBMs, promote the disruption of the intestinal barrier [259], IL-10 is also elevated; this balance may help the barrier integrity to recover after being first damaged by inflammation. In samples that had been treated, the gene for TJs protein was considerably more clearly induced. This might be because, as shown for FNPs, proteases originating from the SHDS are present in the hard corona. In fact, it has been suggested that the protease/antiprotease balance is crucial for maintaining and controlling intestinal permeability [260]. However, the high concentration of protease inhibitors derived from the cell medium could offset this impact. Since the protein corona composition is anticipated to depend on the chemical nature of the NBM, this theory should not necessarily hold true for the other NBMs that have been investigated. On the other hand, it has been noted that TiO_2 nanoparticles upregulated paracellular permeability in mice by decreasing TJ genes expression *in vivo* and *ex vivo* [261]. Sometimes, NBMs like TiO_2 or SiO_2 are combined with dietary additives [262] or bacterial toxins like lipopolysaccharide [263] and they diminish TJs, including adherence and gap junction proteins. We came to the conclusion that the increase in TJs elicited by NBMs was adequate to avoid any loss of barrier integrity because no increase in the permeability of LY was found in our experimental settings for any of the NBMs tested. It is also known that Caco-2 cells exposed to silica nanoparticles undergo an initial disruption of the actin cytoskeleton and TJs architecture, followed by a recovery phase of actin remodelling and TJs reassembly [138]. It is possible that the integrity of the intestinal barrier that we measured was the result of a complete process of barrier reparation after an initial damage.

As predicted, neither untreated nor treated FNPs or CNPs were able to pass through the barrier through the transcellular or paracellular pathways.

It has been widely documented that because NBMs are non-self components, exposure of the intestinal barrier to NBMs causes local inflammation, which is supported by the presence of numerous lymphoid tissues linked to the intestinal mucosa [264] and/or by changes in the gut microbiota [265]. Moreover, epithelial cells naturally produce cytokines and chemokines that play a key role in regulating immune cell activation and preserving the equilibrium of the microbiota [266]. Dysbiosis, pathogenic infection, or inflammatory bowel illness can all be induced by abnormal cytokine production from epithelial cells [266]. We therefore assessed how the production of pro-inflammatory and anti-inflammatory cytokines as the last biocompatibility criteria of NBMs. We found As suggested by suggested by the increase in the expression of typical pro-inflammatory cytokines TNF-α and IL-6, as well as in the anti-inflammatory cytokine IL-10 and in IL-22, related to intestinal epithelial regeneration, we likely have inflammatory events induced by NBMs exposure that are paralleled by a compensatory gene expression of anti-inflammatory and pro-regenerative cytokines. This equilibrium, together with the increased expression of TJs related genes, probably contributes to prevent barrier deterioration and integrity loss. Our findings agree with those of Colombo and colleagues, who found that commercial ZnO NPs boost the production of IL-6 and IL-8 in the Caco-2 barrier model while retaining barrier integrity [267]. Similar to this, polyvinyl chloride particles have been shown to stimulate IL-1β secretion while maintaining the viability and integrity of the Caco-2/HT29-MTX/THP-1 barrier [268]. However, none of this research takes into account the changes that occur during the digestion of NBMs. Indeed, we saw a much higher increase in TJs and cytokines in the case of digested NBMs, which is probably related to the substantial changes that NBMs underwent after SHDS. Yet, these alterations are nonetheless linked with a conserved barrier integrity, as seen by the lack of increased permeability in the Caco-2 barrier exposed to digested SHDS-treated NBMs. Interestingly, CNPs confirmed their status as the NBMs less modified during OGI transit and more biocompatible after oral consumption by being thelower modulators of TJs and cytokines even after SHDS treatment.

3.4 Conclusions

The findings presented in this chapter show that the transit along the OGI tract and the biotransformation of NMBs significantly influences their biocompatibility on intestinal cells. Due to the numerous effects of the observed biotransformation on NBMs bioactivity, no common trend between the various NBMs was found. The results of the current study indicate that using OGI simulating systems that have undergone rigorous validation would enhance the possibility of *in vitro* models to accurately predict the behaviour of NBMs *in vivo*.

The results enclosed in this chapter have been published in Particle and Fibre Toxicology in the paper " Changes of physico-chemical properties of nano-biomaterials by digestion fluids affect the physiological properties of epithelial intestinal cells and barrier models ". [190]

4 Comparison between *in vitro* and *in vivo* effects on gut of nutraceutical nanoformulations

This chapter enclose a study that was conducted as a part of the European project BIORIMA with the aim to compare the *in vitro* model developed in **Chapter 3** whit an *in vivo* situation. It was carried out in collaboration with University of Rome Tor Vergata.

4.3 Materials and methods

4.3.1 Materials and reagents

Plasticware for cell culture was obtained from Falcon (Becton Dickinson, Franklin Lakes, NJ), FBS and cell culture media were from Invitrogen Life Technologies (Carlsbad, CA).

All reagents were purchased from Sigma-Merck if not otherwise specified.

4.3.2 Nanomaterials

As previously described in **Chapter 3**, **section 3.1.2**, LSNPs were produced by Nanovector srl Turin, Italy, and are made of water (Citrate/Phosphate buffer pH 5), glycerol, soy lecithin, glyceryl citrate/lactate/oleate/linoleate (E-472), glycerol monostearate (E-471), polysorbate 20, ascorbyl palmitate, sodium benzoate, α-tocopheryl acetate, strawberry favour, sucralose and loaded or not with Melatonin (0.1% w/w).

4.3.3 Cell cultures

The human colon adenocarcinoma cell line Caco-2 provided by ATCC (Manassas, VA, USA) were expanded and maintained in DMEM (Thermo Fisher Scientific; Waltham, MA, USA) supplemented with 20% v/v FBS, and 1% v/v penicillin/streptomycin. For the viability assay, cells were seeded 24 h before the incubation with NMs in cell media at 10% v/v FBS with a density of 2.5 ×

10^3 cells/well on Falcon ® 96-well Polystyrene Microplates (Corning Life Sciences, Chorges, France). For the viability and permeability assay on Caco-2 barrier model, cells were seeded on Transwell™ inserts (1 µm diameter pore-sizes, growth area of 4.2 cm^2, Corning Life Sciences, Chorges, France) 24 h before the treatment in cell media at 10% v/v FBS with a density of 38×10^4 cells/insert and cultured for 21 days to let them differentiate in adult enterocytes-like cells. The culture medium was changed twice a week until time of use.

All cell cultures were kept in a humidified incubator at 37°C in a 5% CO_2 atmosphere.

4.3.4 Simulated Human Digestion System (SHDS)

The preparation of the simulated fluids and the procedure of SHDS were the same of previous explained in **Chapter 3** in **section 3.1.9**.

4.3.5 Cell exposure to NMs or melatonin

Caco-2 cells were exposed for 24 h to pristine and SHDS-treated NMs the day after cell seeding. Before the exposure the desired concentrations of NMs (2.5, 5, 10, 20, 50, 100 and 150 µg/mL) or the corresponding concentration of melatonin (MLT) (0.42, 0.83, 1.66, 4.2, 8.3, 12.5 µg/mL) were obtained by diluting them in cell culture media.

Caco-2 cells previously cultured on Transwell™ inserts were incubated with pristine and SHDS-treated NMs or MLT for 24 h. Before incubating the cells with NMs, the culture medium was replaced with 1.5 ml of medium containing the NMs or MLT at the desired concentration (50 µg/mL or the respective amount of MLT).

4.3.6 Cell viability

Cell viability measurements was performed as described in **Chapter 3** in **section 3.1.10**.

4.3.7 Trans-Epithelial Electrical Resistance

The TEER was measured as reported in **Chapter 3** in **section 3.1.12**.

4.3.8 Barrier permeability assessment

Similar to the previous chapter, to assess whether a change in permeability of Caco-2 barrier model occurred at the end of the NMs exposure time (24 h), the passage of LY was used following the NANoREG protocol (Standard Operating Procedure for evaluation of NMs impact on Caco-2 cell barrier model).

Briefly, the Bl and Ap medium of each well were removed, and the wells were washed three times with pre warmed (37°C) Hanks' Balanced Salt Solution (HBSS, Thermo Fisher Scientific; Waltham, MA, USA). After the washing steps, inserts were transferred into new 6-wells plates containing 1.5 mL of HBSS in the Bl compartment. At this point 0.5 mL of HBSS with 0.4 mg/mL of LY were inserted in the Ap compartment and incubated for 2 h at 37 °C in 5 % CO_2 incubator.

After the incubation time, the Bl medium was collected and it was loaded in duplicate into black 96-well plates to read the fluorescence using a Synergy HTX microplate reader (Bio-Tek Instruments) (excitation at 428 nm, emission at 536 nm).

The percentage of LY that has crossed the barrier in the wells containing cells has been compared with that of cell-free insert and the apparent permeability (P_{app}) was calculated. The P_{app} is expressed as cm/s and was calculated using the following equation:

$$P_{app} = ((\Delta Q/\Delta t)\cdot V)\cdot(1/AC0)$$

where $\Delta Q/\Delta t$ ((mg/mL)/s) is the NMs transport rate from the Ap to the Bl chamber, A (cm^2) is the area of the membrane (which in our case was 4.2 cm^2), and C0 (mg/mL) is the initial NMs concentration in the Ap chamber.

4.3.9 Mice exposure to NMs

Ten female CD1 mice were treated by oral gavage with High (H) or Low (L) concentrations (i.e., 750 mg and 7.5 mg) of NMs with (+) and without (-) MLT, respectively, three times a week for six weeks. As a negative control, four female mice were treated with citrate buffer as a vehicle. Gut samples were taken from three distinct tracts of the small intestine (duodenum, jejunum, and ileum).

4.3.10 Quantitative Real Time PCR (qRT-PCR)

The phenol/chloroform/ethanol procedure was used to extract the mRNA from the cells. Cells were lysed and tissues were homogenised in RiboZol (VWR; Radnor, PA), incubated for 10 min at room temperature, and then chloroform was added.

The samples were centrifuged for 15 min at 12,000 g at 4 °C after being shaken for 15 s and incubated at room temperature for 3 min. After transferring the aqueous phase to a clean tube and adding isopropanol, the samples were incubated for 10 min at room temperature before being centrifuged at 12,000 g for 10 min at 4 °C. After centrifuging RNA pellets at 12,000 g for 5 min at 4 °C and twice with ethanol 70% v/v, they were resuspended in RNAse-free water. A Take3 plate (Synergy HT Multi-Detection Microplate Reader) was used to measure the amount of RNA by reading the absorbance at 260 nm. RNA samples were reverse transcripted using the iScript cDNA synthesis kit (Bio-Rad, Segrate, Italy), as per manufacturer's instructions.

qRT-PCR was used to estimate the expression levels of the genes listed in **Tables 4.1** (murine) and **4.2** (human) respectively. For each sample, 5 µl of the Bio-Rad Laboratories iTaq Universal SYBR Green Supermix, 2 µl of a mix of 5 µM primers, and 3 µl of cDNA (5 ng/µl) were used. Using a CFX96 Real-Time System (Bio-Rad Laboratories), samples were run 42 cycles for 30 s at 95 °C, 5 s at 95 °C, and 30 s at 60 °C. The analysis was done with the help of the program Bio-Rad CFX Maestro (Bio-Rad Laboratories).

Table 4.1. *Genes and primers used for human cells.*

GENE	5'-FORWARD-3'	5'-REVERSE-3'
TNF	TGGGATCATTGCCCTGTGAG	GGTGTCTGAAGGAGGGGGTA
IL6	GGTACATCCTCGACGGCATCT	GTGCCTCTTTGCTGCTTTCAC
IL10	AGACAGACTTGCAAAAGAAGGC	TCGAAGCATGTTAGGCAGGTT
IL22	GCTGCCTCCTTCTCTTGG	GTGCGGTTGGTGATATAGG
***S14**	AGGTGCAAGGAGCTGGGTT	TCCAGGGGTCTTGGTCCTATTT

* Reference gene

***Table 4.2**. Genes and primers used for murine tissues.*

GENE	5’-FORWARD-3’	5’-REVERSE-3’
TNF	CCTCTCATGCACCACCATCA	GCATTGCACCTCAGGGAAGA
ILB1	AAGGGGACATTAGGCAGCAC	ATGAAAGACCTCAGTGCGGG
IL6	AGCCCACCAAGAACGATAGTC	GCATCAGTCCCAAGAAGGCA
IL10	ACCTGGTAGAAGTGATGCCC	ACACCTTGGTCTTGGAGCTT
IL22	GACAGGTTCCAGCCCTACAT	TCGCCTTGATCTCTCCACTC
NOS2	AGGTTGTCTGCATGGACCAG	GCTGGGACAGTCTCCATTCC
CLDN3	GGTGACAGACGACACACAGT	GTCCATTCGGCTTGGACAGT
CLDN4	TGGTGTGCTGAGTGACTGAC	GGGTCAAGCACAGTCATTGC
CLDN2	AGGAATTGCCCAGAAGCCAA	GGTTTAGCAGGAAGCTGGGT
CLDN5	TTAAGGCACGGGTAGCACTC	CAACGATGTTGGCGAACCAG
OCLN	TCTTTCCTTAGGCGACAGCG	AGATAAGCGAACCTGCCGAG
TJP1	AGAGCTACGCCTGGAGATTC	TGTCCTATTTCCAGCTCCCG
MUC3	GCAGAAGGGCGATAAGTGGT	GCTGACATTTGCCGTAGCTG
***ACTB**	TGAAGTGTGACGTTGACA	TAGAAGCACTTGCGGTGCACG

* Reference gene

4.3.11 Statistical Analysis

For the statistical analysis, ANOVA (ANalysis Of VAriance) with post-hoc Tukey Honestly Significant Difference Test Calculator for comparing multiple treatments [186] was used by using Statistical Package for Social Science software (IBM SPSS Statistics v.19). $p < 0.05$ was considered significant.

4.4 Results

4.4.1 LSNPs cytotoxicity assessment

Taking into consideration the results obtained and discussed in **Chapter 3**, simulated digestion might improve the effects on cell viability of LSNPs. For this reason, we tested their biocompatibility on undifferentiated Caco-2 cells, before and after SHDS treatment, in a concentration range between 5 and 150 µg/ml, based on the highest concentration of simulated digestive fluids alone that do not affect Caco-2 cells viability (**Chapter 3, section 3.2.5, Figure 3.16**). To exclude any possible interference of loaded MLT, also its corresponding concentrations were tested. As shown in **Figure 4.1A**, MLT had not influence on cell viability in the whole concentration range, both in pristine form and in SHDS-treated one. Instead, LSNPs both with and without MLT, became toxic starting from 100 µg/ml only after SHDS treatment (**Figure 4.1B**). While in the pristine form LSNPs did not affect cell viability in presence of MLT, however in the absence of MLT they exerted their toxicity on Caco-2 cells at the highest concentration tested (**Figure 4.1B**), likely due to the lack of MLT that is recognized as a homeostasis maintenance factor on intestinal epithelium [269].

These data also confirm the findings presented in **Chapter 3, section 3.2.5**.

The highest non-toxic concentration (i.e., 50 µg/ml) was then employed to investigate the effects on Caco-2 intestinal barrier model.

After 24 h of exposure, cell viability was measured by using WST-1 assay: in all conditions tested the viability remained unchanged (**Figure 4.2A**).

Instead, to verify if LSNPs affected the integrity of the barrier, TEER as well as the LY passage were measured. If the LY assay did not show significant differences between control and treated barrier both calculating the percentage (**Figure 4.2C**) and the P_{app} (**Table 4.3**), TEER showed an increased value when the barrier was exposed to pristine MLT (**Figure 4.2B**), confirming the beneficial role of the latter on intestinal epithelium.

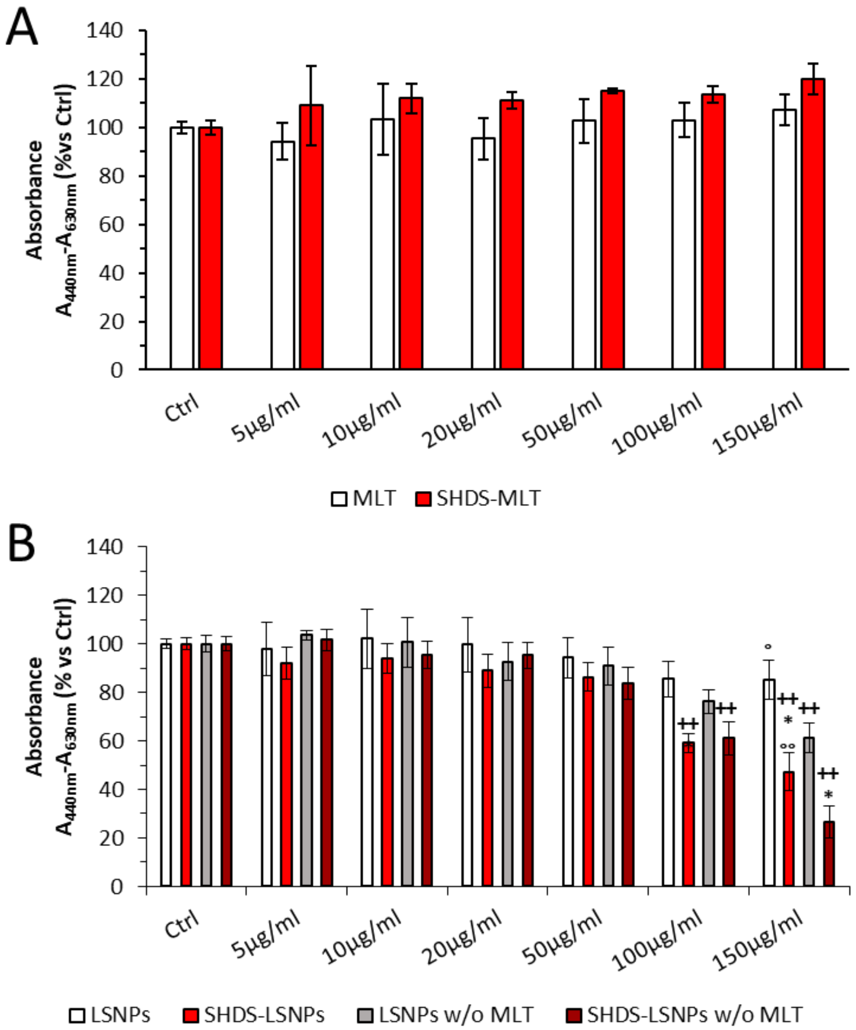

Figure 4.1. Caco-2 cell viability *after 24 h of exposure to* ***A)*** *melatonin and* ***B)*** *pristine and SHDS-treated LSNPs with or without MLT. ++$p<0.01$ vs Ctrl; *$p<0.05$ vs pristine; °$p<0.05$ vs w/o MLT; °°$p<0.01$ vs w/o MLT.*

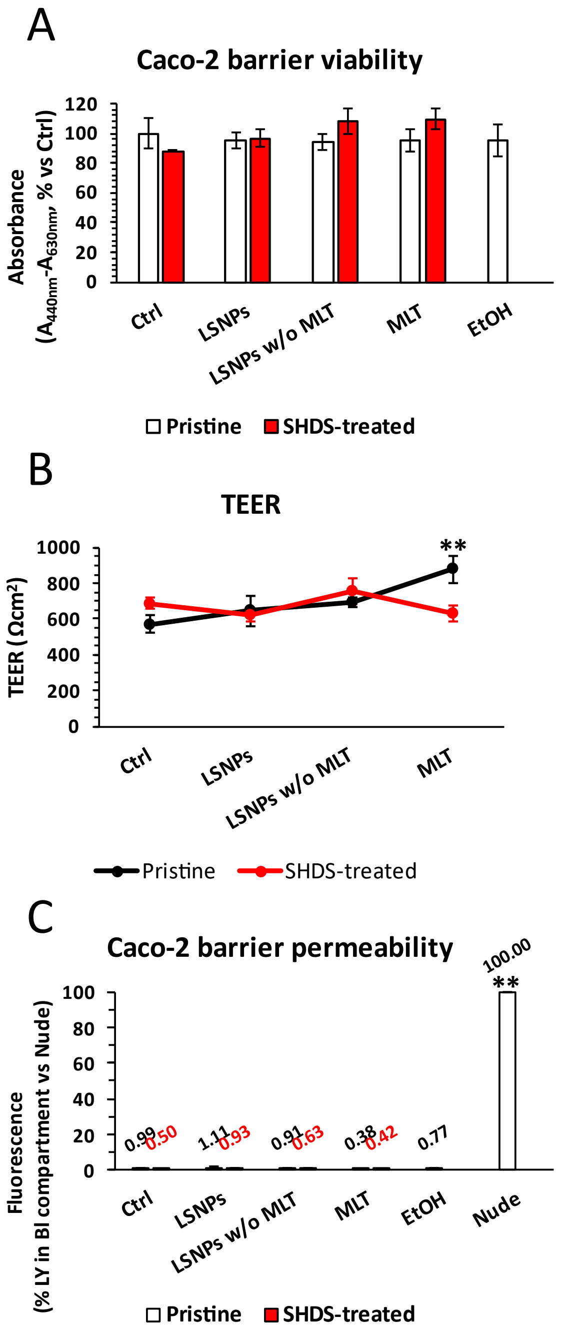

Figure 4.2. *Caco-2 barrier model* ***A)*** *cell viability,* ***B)*** *Trans Epithelial Electrical Resistance, and* ***C)*** *permeability after 24 h of incubation with NBMs. **p<0.05 vs Ctrl.*

Table 4.3. Apparent permeability of Caco-2 barrier model after 24 h of exposure with NBMs.

P_{app} (cm/s x 10^{-8})		
	Pristine	**SHDS-treated**
Ctrl	8.6 ± 4.5	7.4 ± 1.6
LSNPs	5.7 ± 1.2	7.2 ± 4.6
LSNPs w/o MLT	6.8 ± 3.7	7.1 ± 2.4
MLT	7.8 ± 2.2	7.6 ± 4
EtOh	6.8 ± 3.5	

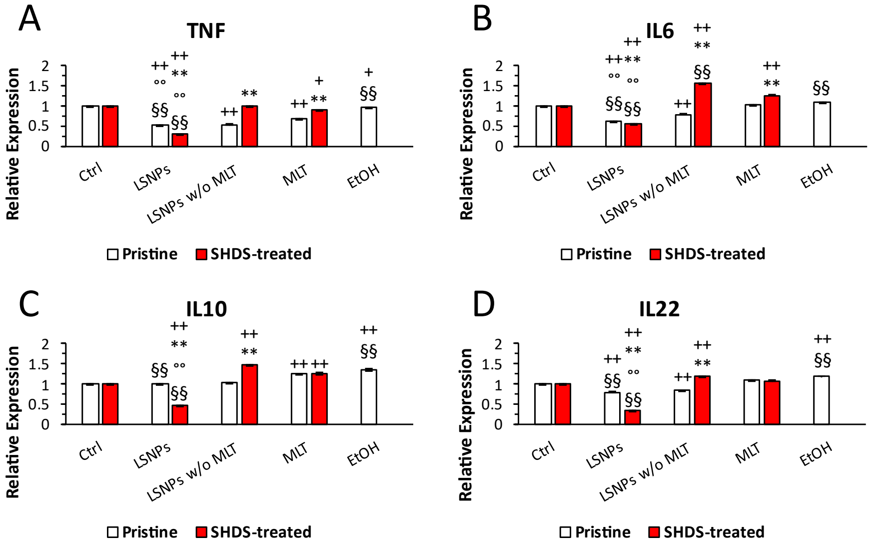

Figure 4.3. Gene expression of inflammation-related genes in Caco-2 barrier model. A) *TNF,* ***B)*** *IL6,* ***C)*** *IL10, and* ***D)*** *IL22. +p<0.05 vs Ctrl; ++p<0.01 vs Ctrl; **p<0.01 vs pristine; °°p<0.01 vs w/o MLT; §§p<0.01 vs MLT.*

To get a complete picture of the LSNPs effects on Caco-2 barrier, the expression of two pro-inflammatory cytokines genes (i.e., TNF and IL6) and of two anti-inflammatory cytokines genes (i.e., IL10 and IL22) was investigated.

If for TNF there was no evidence of up-regulation for all tested conditions (**Figure 4.3A**), IL6 was decreased after the exposure to SHDS-treated LSNPs without MLT (**Figure 4.3B**).

At the same time, this exposure condition seems to induce the concomitant up-regulation of anti-inflammatory IL10 and, albeit at a lesser extent, of IL22 (**Figure 4.3C and 4.3D**), that might be the responsible of the absence of loss in barrier integrity despite the induced inflammation response.

4.4.2 LSNPs effects on mice's gut

In parallel to the *in vitro* experiments, the effects of LSNPs on the gut in terms of barrier integrity and inflammation were investigated on an animal model using CD1 mice. They were exposed to two different concentrations of LSNPs with and without MLT three times a week for 6 weeks. At the end of the treatment, the mice were sacrificed and three different segments of the intestine (i.e., duodenum, jejunum, and ileum) were resected and analysed by qRT-PCR for encoding genes of TJ proteins, a mucin, pro- and anti-inflammatory cytokines.

For all TJ proteins, with the exception of TJP1, the exposure to higher concentration of LSNPs without MLT resulted in an important down-regulation for all of three intestinal sections analysed (**Figure 4.4**). Instead, TJP1 showed to be up-regulated in jejunum and ileum (**Figure 4.4A**). When the same particles were administered at lower concentration, they maintained the same effect on almost all TJ proteins in duodenum and ileum but they increased their expression in jejunum (**Figure 4.4**). Instead, LSNPs with MLT induced an overexpression of all TJ proteins in jejunum both for higher and lower doses in a concentration-dependent manner (**Figure 4.4**), while for the other two intestinal segments almost all TJs genes did not undergo to important variation excepted for CLDN2, CLDN3 and CLDN4 that were slightly up-regulated in duodenum (**Figure 4.4C, D and E**), OCLN, CLDN2 and CLDN5 that were slightly overexpressed in ileum (**Figure 4.4B, C and F**), and TJP1 and CLDN3 that were slightly down-regulated in duodenum and ileum, respectively (**Figure 4.4A and D**).

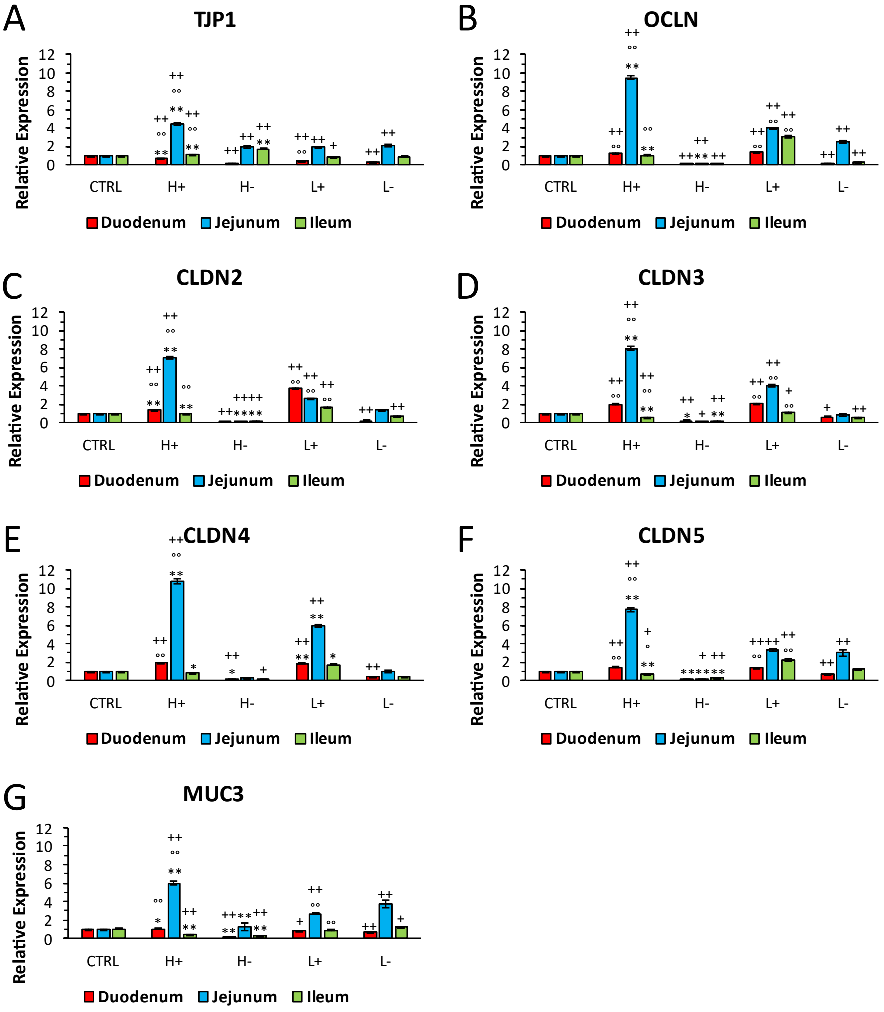

Figure 4.4. Gene expression of intestinal barrier integrity-related genes in mice. A) *TJP1,* ***B)*** *OCLN,* ***C)*** *CLDN2,* ***D)*** *CLDN3,* ***E)*** *CLDN4,* ***F)*** *CLDN5, and* ***G)*** *MUC3.*
H: LSNPs with (+) and without (-) MLT higher concentration
L: LSNPs with (+) and without (-) MLT lower concentration
*+p < 0.05 vs Ctrl; ++p < 0.01 vs Ctrl; °p<0.05 vs w/o MLT; °°p<0.01 vs w/o MLT; *p<0.05 vs lower concentration; **p<0.01 vs lower concentration.*

MUC3 followed the trend of TJ genes: in duodenum it was decreased after treatment with LSNPs without MLT in a dose-dependent manner; in jejunum it was always overexpressed, apart for the higher concentration of LSNPs without MLT; in ileum it was down-regulated at higher concentration of LSNPs both with and without MLT (**Figure 4.4G**).

Parallelly to these changes in the expression of genes involved in intestinal barrier integrity, also the inflammation-related genes underwent a different regulation.

All analysed inflammation-involved cytokines were down regulated, albeit at different extent, after exposure to higher concentration of LSNPs without MLT (**Figure 4.5**), similarly to what were found for TJ proteins genes (**Figure 4.4**).

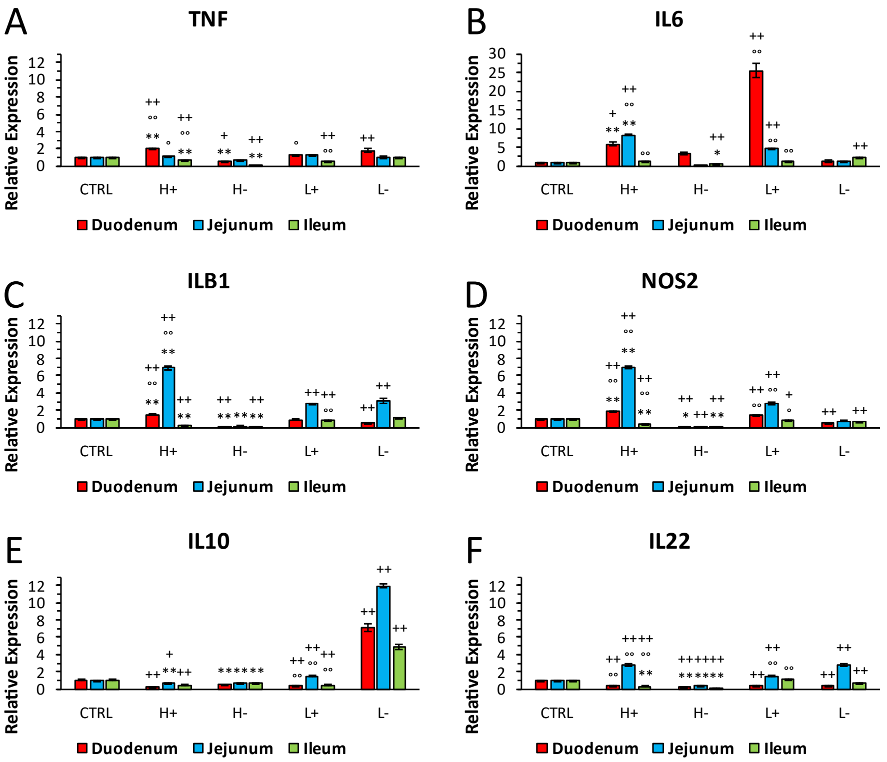

Figure 4.5. Gene expression of intestinal barrier inflammation-related genes in mice.
***A)** TNF, **B)** IL6, **C)** ILB1, **D)** NOS2, **E)** IL10, and **F)** IL22.*
H: LSNPs with (+) and without (-) MLT higher concentration
L: LSNPs with (+) and without (-) MLT lower concentration
*+p < 0.05 vs Ctrl; ++p < 0.01 vs Ctrl; °p<0.05 vs w/o MLT; °°p<0.01 vs w/o MLT; *p<0.05 vs lower concentration; **p<0.01 vs lower concentration.*

Instead, the lower dose of the same particles led to an up-regulation of the pro-inflammatory cytokines genes TNFα in duodenum and IL1B in jejunum (**Figure 4.5A and C**), as opposed to the overexpression of anti-inflammatory cytokines genes IL22 in jejunum and IL10 in all intestinal segments analysed (**Figure 4.5E and F**). In presence of loaded MLT, in contrast, TNF in duodenum (**Figure 4.5A**), IL1B in jejunum (**Figure 4.5C**) and IL6 in both (**Figure 4.5B**), only countered in jejunum by an overexpression of IL22 (**Figure 4.5F**).

Finally, NOS2 gene, which is reported to play a role in the attenuation of inflammatory response in IBD [270–272], was up-regulated in jejunum only for LSNPs with MLT (**Figure 4.5D**).

4.5 Discussion

This work, as a part of the European project BIORIMA, was aimed to investigate the possible effects of ingested LSNPs, developed as nutraceutical formulation to vehicle the melatonin to the gut and improve its adsorption.

In the last years the human exposure to NMs has been increasing thanks to their widespread employment due to their unique properties, which make them versatile and therefore easily usable in different fields, particularly in the healthcare [57,273–275].

Despite ingestion is one of the main routes of voluntary or involuntary human exposure to NMs, nowadays a validated *in vitro* model to study the NMs biocompatibility towards the gut is not still available. The main reason of this lack is likely identifiable in the complexity of the digestive system, which makes it hard to reproduce *in vitro* all the important features of this apparatus. In particular, it is difficult not only to mimic the intricate structure of the intestinal tissue, but also the possible modifications to which the NMs undergo during the digestion process due to the interaction with the different environmental conditions found along the gastro-intestinal tract (i.e., agglomeration/aggregation, degradation, bio-corona formation) that could affect the particles-cells interaction, making the data inconclusive respect to that obtained *in vivo*.

For this reason, we evaluated both *in vitro* and *in vivo* the gut effects of two nano-formulations applying a simulated human digestion system before their exposure to Caco-2 intestinal cells and intestinal barrier model.

It is now proven that lipid-based particles are susceptible to degradation during the digestive process by lipolysis to different extent depending on their structure and composition [238–240]. An example is represented by the work of Zöller and colleagues in which they observed a partially digestion by lipases and pancreatin of all tested lipidic particles, albeit to different extent depending on the particles composition. In particular the study reports a great resistance to enzymatic degradation in presence of PEG polymers [240]. Similar findings were reported by Ban and co-workers who made lipidic particles more resistant to the digestive process by PEGylating them [238].

Similarly, in this thesis work, we observed important SHDS-induced modifications in LSNPs structure, as already disclosed in the previous chapter (**Chapter 3, section 3.2.2**). Moreover, we hypothesised that the simulated digestion-induced the LSNPs-contained surfactant (**section 4.3.2**) release from the outermost layers of the particles under the lipase activity can affect the cell viability at higher concentrations (**Chapter 3**). In fact, after degradation some components of lipid-based NPs could be released in the surrounding environment and may also have toxic effects [239]. The type and amount of released surfactants will be determinate by high performance liquid chromatography in future investigation.

Confirming all these previous findings, in this part of the thesis we observed a loss in Caco-2 cells viability at higher doses only for SHDS-treated LSNPs, in line with our previous findings (**Chapter 3, section 3.2.5**). Conversely, in the absence of loaded MLT not only the induced toxicity increased, but also the pristine LSNPs affected cell viability. MLT was found to be a gut homeostasis maintenance factor thanks to its antioxidative and anti-inflammatory properties [269,276,277]. In fact, it was demonstrated that the MLT administration is able to restore the physiological conditions in mice after sleep deprivation, dextran sodium sulphate or sodium diclofenac-induced gut damage [269,278,279]. Moreover, in clinical study on IBD the co-administration of MLT with the conventional treatments was able to enhance the beneficial effects of the latter in patients during the active phase of these pathologies [280], while administering MLT in the remission phase helped to maintain the remissive condition for a longer time [281].

Therefore, the MLT beneficial effects can be responsible for the lower cytotoxicity of LSNPs in comparison to LSNPs w/o MLT. In fact, when we moved to Caco-2 barrier model we observed neither viability nor permeability perturbation in all conditions tested, except for free MLT which increased the barrier TEER value: this was likely due to its beneficial roles on the intestine that could improve the junction between cells. Indeed, the MLT ability in TJs genes regulation is greatly demonstrated. An example is the work of Lin and co-workers in which they observed an increased expression of TJ proteins in mic after treatment with MLT [282]. Similarly, another study reported that the reduction of TJ proteins induced by sleep deprivation in mice can be counteracted by MLT administration that upregulated TJ genes [276].

To complete the picture, we also investigate the possible LSNPs involvement in inflammation by measuring the expression of genes encoding for two pro-inflammatory cytokines found to be related to IBD and irritable bowel syndrome (IBS) i.e., TNF-α and IL-6 [282,283,284] and two anti-inflammatory cytokines produced in response to gut inflammation i.e., IL-10 and IL-22 [284,286,287].

We observed an increased expression of TNF only for SHDS-treated LSNPs w/o MLT, probably due to the SHDS-induced surfactant release. If this hypothesis was true, also the particles loaded with MLT would have shown the same effect. However, considering the MLT ability to modulate the inflammation-related genes [277,288] this incongruence between our experimental findings and the previous hypothesis could be explained. In fact, as observed by Akcan and co-workers, MLT is able to reduce the TNF-α serum levels in rat [277]. Moreover, TNF-α is a well-known intestinal barrier hyperpermeability inducer as demonstrated by *in vitro* studies on Caco-2 cells [289] and by clinical studies in which an anti-TNF-α treatment reached good outcomes in IBD patients [290]. Despite we observed a TNF expression increase after the exposure of Caco-2 barrier to SHDS-treated LSNPs w/o MLT, no TEER nor LY crossing were found, as previously discussed. At the same time, also IL10 and IL22 underwent an up-regulation in our model. Both cytokines encoded by these two genes are involved in intestinal barrier inflammation prevention [291,292]. Moreover, IL-10 is related to the control of abnormal immune response in the gut [293,294] and is produced in response to pro-inflammatory factor modulating them [295], while IL-22 promotes epithelial cells proliferation and has a protective role in IBD [296]. Therefore, the concomitant up-regulation of anti-inflammation-related gens IL10 and IL22 could explain the barrier integrity maintenance in spite of TNF induction.

To understand if the *in vitro* findings can reflect a realistic intestinal response to the two nano-formulations studied, the same outcomes were investigated on CD1 mice after three weeks gavage treatment with LSNPs loaded or not with MLT.

After evaluating the gene expression of TJs-related proteins, a mucin, and pro- and anti-inflammatory factors, we generally observed a greater effect in the jejunum with respect to the duodenum and ileum, where we found no alterations in the expression of the analysed genes. This trend can be explained by the fact that jejunum is the intestinal tract responsible of lipid absorption and metabolism, and the huge presence of specialised membrane receptors [297] can lead to a major interaction with LSNPs than in duodenum and ileum.

In general, LSNPs w/o MLT at higher dose down-regulated most of TJ and inflammation related genes, while at lower dose the situation is the opposite, suggesting an induced tissue damage that at higher concentration cannot be thwarted. For LSNPs with MLT we observed for both lower and higher concentrations a general overexpression of the same genes. The mechanism underlying the overexpression of TJ and inflammation related genes at lower concentration could be the initial induction of an inflammatory process, where the up-regulation of pro-inflammatory cytokines genes in turn stimulates the production of anti-inflammatory cytokines, as already was observed *in vitro* and *in vivo* in IBD models [298]. Since IL10 and IL22 are protective of intestinal barrier physiology [291,292], their production could induce the TJ genes up-regulation avoiding intestinal barrier damage. MLT which, as previously mentioned, is able to compensate a gut barrier damage restoring the physiology by modulating pro-inflammatory genes and enhancing anti-inflammatory genes can explain the protection against tissue damage at LSNPs higher concentration, [276,277]. At the same time, MLT has the ability to up-regulate the TJ encoding genes [276,282] leading to a maintenance or a restoration of intestinal barrier structure. In fact, LSNPs at higher concentration showed a general gene up-regulation of both pro- and anti-inflammatory cytokines and even of TJs and mucin.

The *in vivo* results were similar to what was observed on Caco-2 barrier model, in particular after LSNPs treatment with SHDS for which, in the absence of MLT, we found an overexpression of pro-inflammatory TNF-α encoding gene in conjunction with the up-regulation of anti-inflammatory IL10 and IL22 with any variation in cell viability and barrier integrity.

All together these *in vitro* and *in vivo* findings suggest that LSNPs at high concentrations can damage the gut tissue structure by inducing inflammation, but the presence of MLT lead to the activation of compensatory mechanisms restoring the gut structure and physiology.

4.6 Conclusions

In this study we obtained a good alignment between *in vitro* and *in vivo* results. Despite few differences, our *in vitro* model where LSNPs were subjected to SHDS reflected well the effects of ingested nano-formulations obtained in mice, highlighting the importance of considering the modifications caused by the digestion process in the nano-materials biocompatibility/toxicity evaluation. The observed differences could be caused by the impossibility to know the effective intestinal nanomaterials doses. Hence, further studies are needed in order to better mimic a real exposure *in vitro* in future evaluations. Moreover, the cellular model could be improved by adding different cell types and intestinal conditions such as flow and pressure in order to recapitulate the intestinal-like environment and structure that is important for the particles-tissue interaction.

5 Advanced *in vitro* gut models to study the effects of ingested microplastics

This chapter enclose the work in the context of the European project PlasticsFatE that was carried out in collaboration with Gaiker Technology Center where I was hosted for a period abroad. The aim of this chapter is to improve the previous developed *in vitro* model to make it closer to the real situation assessing the possible intestinal effects of microplastics.

5.3 Materials and methods

5.3.1 Materials and reagents

Cell cultures plasticware was from Falcon (Becton Dickinson, Franklin Lakes, NJ), while FBS and culture media were purchased from Invitrogen Life Technologies (Carlsbad, CA).

If not otherwise specified, reagents were from Sigma-Merck.

5.3.2 Micro-plastics

High-density polyethylene (HDPE) micro-particles are commercial product of Clariant AG (Muttenz, CH) and were dispersed in a solution of 0.25% w/v bovine serum albumin (BSA) in ultrapure water. To obtain a stable suspension, the dispersion was sonicated in an ultrasound bath for 30 min and then the bigger and aggregated particles were removed by transferring the suspension in a fresh bottle.

5.3.3 Biofilm formation on MPs

Vibrio parahemoliticus was seeded on blood agar and the day after an inoculum of 10^9 CFU in Tryptic soy broth (TSB, Merck KGaA, Darmstadt, Germany) was prepared to dilute it at 10^8 CFU in Marine Broth (Fisher Scientific, Göteborg, Sweden) in which 1 mg/ml MPs was dispersed. The bacteria were grown 48 h by adding fresh Marine Broth at 24 h of incubation with MPs. At the end of the incubation, the suspension was filtered (filter porous dimension 5 µm) in order to separate the unattached bacteria to the MPs with formed biofilm. Even if with the equipment at our disposal we are not able to discriminate if this incubation results in a complete biofilm formation with specific features such as the presence of a matrix or in a simple bacteria attachment.

To recover the MPs, the filter was turned, and the medium was flowed through. As HDPE MPs have a size average of 5 µm, we are not able to ascertain that the smallest particles are retained by the filter and therefore recovered for exposure to the cells.

5.3.4 Simulated Human Digestion System (SHDS)

Unlike the system used in **chapter 3** and reported in **section 3.1.9**, for this study we follow the INFOGEST protocol [156] slightly modified by the European project consortium as to harmonize the methods used in the whole PlasticsFatE project.

The simulated fluids were prepared as explained in the work of Brodkorb and co-workers [156] and their content is reported in **Table 5.1**. Briefly, a concentrated stock solution of each salt was prepared and then the correct volume was added to ultrapure water to reach the 1.25X concentration of simulated saliva fluid (SSF), simulated gastric fluid (SGF), and simulated intestinal fluid (SIF). Just before the experiment, the correct amount of active components and the correct volume of $CaCl_2$ fresh stock solution were added to the different simulated fluids. Starting from a precise sample volume, the SSF 1.25X was added; employing a 1M HCl solution the pH was adjusted to 7 before bringing to final volume to reach the SSF 1X concentration. The sample was incubated for 2 min at 37 °C under agitation. After the incubation time, the SGF 1.25X was added to the mixture and the suspension was brought to pH 3 and final volume reaching a 1X concentration of SGF.

Table 5.1. *Content of simulated digestive fluids.*

Components	**SSF**	**SGF**	**SIF**
Salts	mM	mM	mM
KCl	15.1	6.9	-
KH_2PO_4	3.7	0.9	0.8
$NaHCO_3$	13.6	25	85
NaCl	-	47.2	38.4
$MgCl_2(H_2O)_6$	0.15	0.12	0.33
$(NH_4)_2CO_3$	0.06	0.5	-
HCl	1.1	15.6	8.4
$CaCl_2(H_2O)_2$	1.5	0.15	0.6
Active components	mg/ml	mg/ml	mg/ml
Mucin	0.23	0.42	-
α-amylase	0.167	-	-
Pancreatin	-	-	31
Rabbit gastric extract*	-	8	-
Bile	-	-	11.7

*Rabbit gastric extract (RGE) was from Lipolytech (Marseille, France)

The mixture was incubated at 37 °C under agitation for 2 h. Finally, SIF 1.25X was added to the sample and HCl 1M and ultrapure water were added to achieve pH 7 and final volume getting the SIF 1X concentration. The sample was then incubated for a further 2 h at 37 °C under agitation.

5.3.5 Scanning Electron Microscope (SEM) analysis

To visualise the particles at the Scanning Electron Microscope (SEM), the samples were filtered on a paper filter (pores 5µm) and then dehydrated until the critic point incubating them in ethanol at increasing concentrations (30-100%), and in hexamethyldisilazane. After an overnight solvent evaporation, the samples were covered by gold under argon atmosphere and analysed by using a SEM (EVO 50, Zeiss, Spain).

5.3.6 Cells culture

Caco-2 (ATCC) (passage 30-43) and HT29-MTX cells (passage 51-58) (ECACC) were grown and maintained in DMEM 1% v/v P/S, 1% v/v non-essential amino acids (NEAA), 1% v/v Sodium Pyruvate supplemented with 20% and 10% v/v of FBS respectively. Raji B (ATCC) and THP-1 cells (passage 8-25) (ATCC) were conditioned to grow in DMEM 10% v/v FBS. All cell cultures were passed 2 or 3 times a week and were maintained at 37 °C in humidity conditions with 5% CO_2.

5.3.7 Wheat Germ Agglutinin staining

Fluorescein isothiocyanate (FITC)-labelled wheat germ agglutinin (WGA) was used due to its strong affinity for sialic acid and N-acetylglucosamine residues found in M-cells to validate the production of M cells by the Caco-2/Raji B co-culture. After two PBS washes, 4% formaldehyde was used to fix the cells for 25 minutes at room temperature. After three PBS washes, the cells were treated with a 5.0 µg/ml WGA-FITC conjugate in PBS for 15 min at room temperature. After that, PBS was used to wash the cells twice. The polycarbonate inserts were meticulously removed, put on a microscope slide with Fluoroshield™ with 4′,6-diamidino-2-phenylindole (DAPI), covered with a glass coverslip, and left to dry at 4 °C for 24 hours before visualization with fluorescence microscope (Leica DC100, Leica Microsystems GmbH, Wetzlar, Germany).

5.3.8 Alcian Blue Staining

Alcian blue staining was employed to demonstrate that the Caco-2/HT29-MTX co-culture model produced mucus. Briefly, PBS was used to wash the Caco-2/HT29-MTX co-culture twice, and 4% formaldehyde was used to fix it for 25 minutes at room temperature. The cells were stained with 10 mg/ml Alcian blue (in 3% acetic acid) for 30 min at room temperature after being rinsed three times with PBS. The inserts were carefully removed and placed onto a microscope slide. A glass coverslip was placed over the cells, and they were then observed under a microscope (Leica DC100, Leica Microsystems GmbH, Wetzlar, Germany).

5.3.9 Cells exposure to MPs/NPs

Caco-2 cells were seeded as mono-culture in 96-well plates 72 h before the experiment at a density of 5 x 10^4 cells/well in order to reach a 100% confluence. Moreover, Caco-2 and HT29-MTX cells (ratio 9:1) were seeded in 96-well plates at a density of 2.88 x 10^4 cells/well and grown as co-culture for 21 days as to let them reach the completed maturity (i.e., enterocyte-like phenotype for Caco-2 and the production of a physiological-like mucus layer for HT29-MTX). After the growth phase, the cultures were exposed to increasing concentration of pristine or SHDS-treated MPs in a range of 1-100 µg/ml or the tantamount amount of dispersant diluting them in cell culture medium (i.e., DMEM 10% v/v FBS, 1% v/v P/S, 1% v/v Sodium pyruvate and 1% NEAA) without phenol red. The cells were exposed for 4 h a day for 4 weeks in the chronic experiments and from 24 h during the acute experiments. **Figure 5.1** show the workflow of co-culture model exposure to HDPE MPs.

Caco-2 and HT29-MTX cells were even co-cultured on 24-well or 12-well membrane porous cell culture inserts (STEMCELL Technologies, Canada or VWR International, Pennsylvania) and on LB2 chambers of IV-Tech millifluidic device (IV-Tech, Massarosa, Pisa, IT) – that have the same growth area of 12-well cell culture inserts – at a density of 9 x 10^4 cells/cm^2 in a ratio 9:1 for 21 days. At day 14, 1 x 10^5 Raji B cells were added to the Bl compartment of each insert to allow the Caco-2 differentiation into M-cells [299]. After removing Raji B cells, the obtained barrier model was exposed to 100 µg/ml of pristine or SHDS-treated MPs, or to the equivalent amount of dispersant diluting them in cell culture medium (i.e., DMEM 10% v/v FBS, 1% v/v P/S, 1% v/v Sodium pyruvate and 1% v/v NEAA) without phenol red. The exposure took place 4 h a day for 5 days to simulate sub-chronic conditions. For the millifluidic experiments (**Figure 5.2**) the circulating volume was 5 ml for Ap compartment and 15 ml for Bl compartment, while the flow was set at 200 µl/min and 100 µl/min for Ap and Bl compartment respectively to reach the physiological pressure [300].

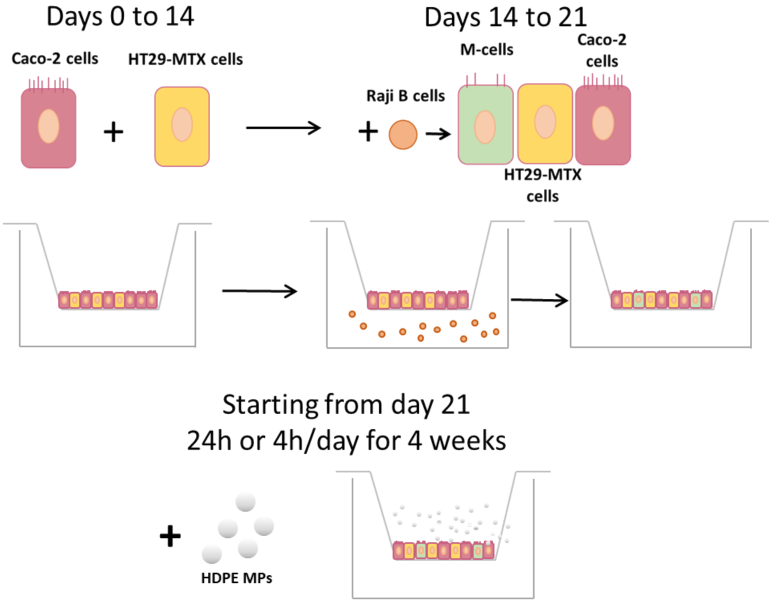

Figure 5.1. *Schematic representation of co-culture intestinal model exposure to HDPE MPs workflow.*

Moreover, undifferentiated Caco-2 cells in 96-well plates and the tri-co-culture barrier model (i.e., Caco-2/HT29-MTX/Raji B cells) on 24-well cell culture inserts were exposed for 24 h to different concentrations (1, 10, 100 µg/ml) of pristine or SHDS-treated MPs before (V-) or after (V+) the formation of *Vibrio Parahemoliticus* biofilm.

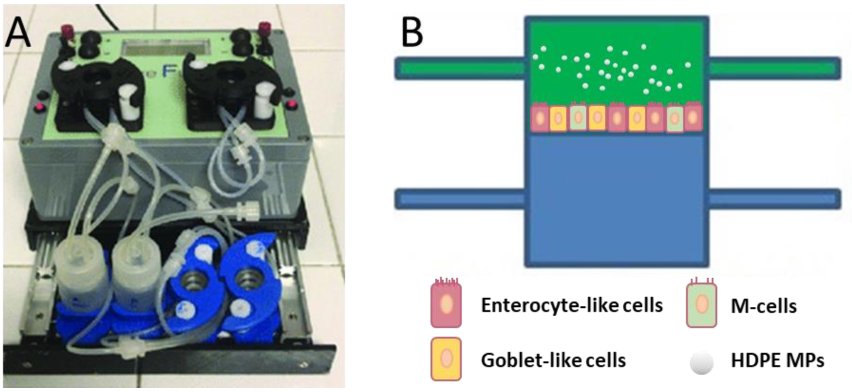

Figure 5.2. Millifluidic device. A) *Image of millifluidic system and* ***B)*** *schematic representation of the exposure experiment in a cell of the millifluidic system. Modified from IVTech web page* [301].

5.3.10 Cell viability

Cell viability was measured as metabolic activity using the Alamar Blue® Cell Viability Reagent (Thermo Fischer Scientific, Massachusetts). This kit exploits the ability of the cells to reduce the active principle into resorufin, a red coloured and fluorescent compound, detectable via absorbance or fluorescence reading.

The reagent was added to fresh cell culture medium at 10% v/v and cells, after replacing the medium, were maintained in incubator for 4 h. After the incubation time, the absorbance (570 nm) or the fluorescence (ex. 560 nm; em. 590 nm) was read and the value obtained for dead cells (treated for 15 min with 0.2% Tryton X-100) was subtracted.

5.3.11 Barrier permeability assessment

The protocol used to investigate the variation in barrier permeability was similar to that used in **chapters 3** and **4,** respectively described in **section 3.1.13** and **4.1.8**, in accordance with NANoREG protocol (Standard Operating Procedure for evaluation of
NPs impact on Caco2 cell barrier model), but with slight modifications. In brief, cell culture medium was collected for further investigation and cells and well were washed with HBSS. Then, 0.1 mg/ml LY solution in HBSS was added in the Ap compartment and cells were incubated for 1 h at 37 °C. After incubation, the fluorescence was read (excitation: 504 nm, emission: 529 nm) as RFUs employing a Synergy HT Multi-Detection Microplate Reader to calculate the apparent permeability (P_{app}) and the percentage of fluorophore recovered from the lower chamber in cell-free inserts.

P_{app} was calculated using the following equation:

$$P_{app} = (VB \times C1) / (A \times t \times C0)$$

*w*here *VB* is the volume of HBSS in the basal compartment, *C0* and *C1* are concentrations in mg x mL-1 of respectively the initial solution and the Bl compartment, *A* is the area of cell culture insert, and *t* is time in hours.

5.3.12 Trans Electrical Epithelial Resistance (TEER)

TEER was measured as described in **chapters 3** and **4** and described in sections **3.1.12** and **4.1.7** using the Millicell® ERS-2 voltohmmeter (Merck KGaA, Darmstadt, Germany) to evaluate the barrier development and integrity of the barrier model. The resistivity was calculated starting from the value in ohms of the cell-containing inserts by subtracting the value of the cell-free inserts and multiplying by the growth area, according to the method reported in **section 3.1.12**.

5.3.13 Cytokines release assessment

Induction of inflammation was evaluated by employing enzyme-linked immunosorbent assays (ELISAs). IL-6, IL-8, TNF-α, IL-10, and IL-22 were measured in cell culture medium at different time points of incubation with MPs, following the manufacturer instruction (Thermo Fischer Scientific, Massachusetts).

5.3.14 Statistical Analysis

The statistical analysis was performed via ANOVA (ANalysis Of VAriance) with post-hoc Tukey Honestly Significant Difference Test Calculator for comparing multiple treatment [186]. by using Statistical Package for Social Science software (IBM SPSS Statistics v.19) and by GraphPad Prism® software. $p < 0.05$ was considered significant.

5.4 Results

5.4.1 Evaluation of *Vibrio parahaemolyticus* biofilm formation on MPs surface and the effect of the simulated digestive system

MPs are able to act as scaffold for bacterial colonies allowing them to make a solid structure called biofilm [114].

To verify if the studied MPs could be a good support for this structure, the formation of *V. parahaemolyticus* biofilm on the MPs surface was evaluated by SEM analysing the particles before and after incubation with the bacteria. **Figure 5.3A** shows the pristine particles, which have different size, confirming the inhomogeneity of the sample. Moreover, with a great magnification we could appreciate that MPs appear irregular in shape (**Figure 5.3B**). After two days of incubation with *V. parahaemolyticus*, it is possible to see the presence of the bacteria to the surface of MPs, as shown in **Figure 5.3B’**.

Since it is not possible by SEM to correctly define the amount of bacteria present in a certain volume of MPs suspension, the CFUs were quantified by sample filtration followed by plating on blood agar the particles trapped in the filter or the filtrate.

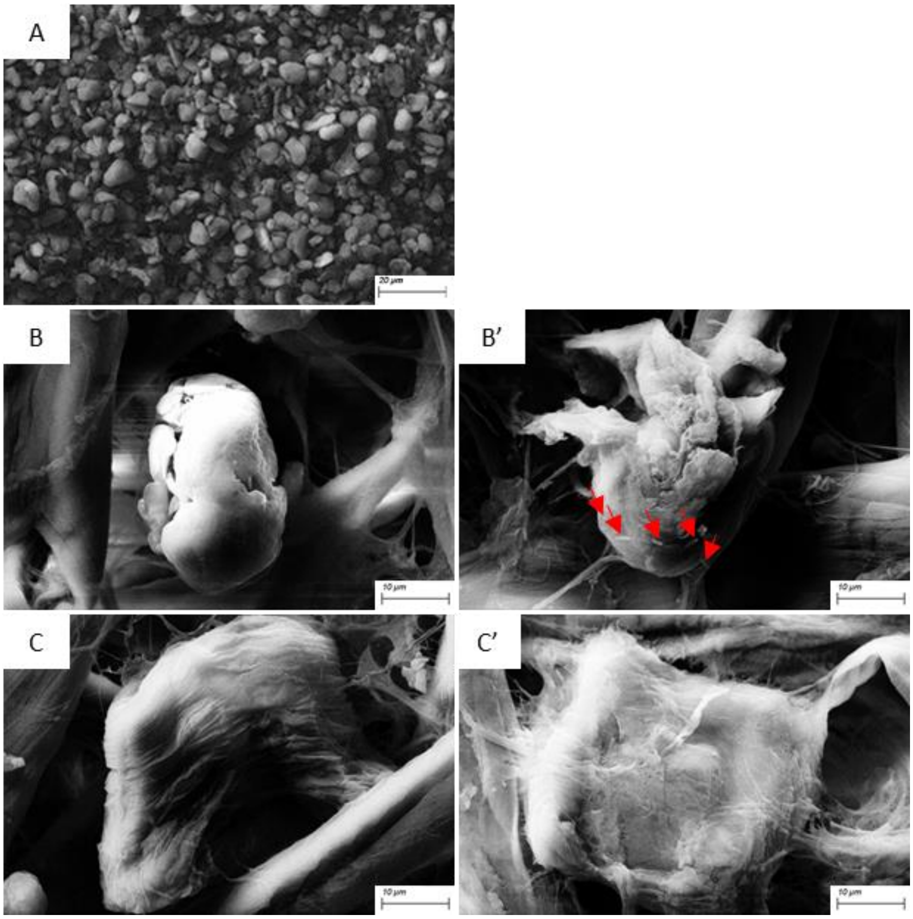

***Figure 5.3. Representative SEM images** of **A)** pristine HDPE MPs (lower magnification), pristine HDPE MPs (higher magnification) **B)** before and **B')** after incubation with V. parahaemolyticus, and SHDS-treated HDPE MPs **C')** with and **C)** without previous incubation with V. parahaemolyticus. The bacteria are indicated with red rows.*

Table 5.2 reports the quantification of bacteria on the MPs surface and in the filtrate supernatant. In samples with *V. parahaemolyticus* biofilm we counted an average number of 4.59 x 10^7 bacteria on the filtered MPs, while in the dispersant the amount was two orders of magnitude higher (**Table 5.2**). We did not saw any colony formation plating the samples without biofilm.

It is demonstrated that MPs disseminated in the environment may by ingested through food intended for human consumption (e.g., fish and seafood) [91,302–304]. After ingestion, the particles are submitted to the digestive process that could make surface and structural changes, as previously described in **Chapter 3**. The digestive fluids can also interact with the MPs attached bacteria, modifying the previous formed biofilm.

To investigate this possibility, MPs and MPs with *V. parahaemolyticus* biofilm were subjected to SHDS and then examined by SEM and by plating them to obtain a qualitative and quantitative analysis respectively.

These samples showed the presence of an organic matrix not only on the particles surface, but even on the surrounding support (**Figure 5.3C**) likely made up by active components of simulated digestive fluids. It is evident the decrease in bacteria attached to the MPs surface for the sample with biofilm, which moreover appear covered by the organic matrix (**Figure 5.3C'**). It is possible that the bacteria were detached to the MPs and partially killed by the SHDS treatment, but even they could be between the MPS surface and the organic matrix coating.

The counting of CFUs confirms the partial death of *V. parahaemolyticus* after SHDS treatment that happens also for free bacteria in the dispersant with a reduction in number of almost 50% (**Table 5.2**).

***Table 5.2**. CFU number on 100 µg/ml suspension of MPs.*

CFU/100 µg/ml MPs	HDPE MPS	HDPE MPs supernatant
- SHDS	$4.59 \times 10^{7} \pm 7.5 \times 10^{6}$	$2.58 \times 10^{9} \pm 5.9 \times 10^{8}$
+ SHDS	$2.74 \times 10^{4} \pm 1.9 \times 10^{4}$	$1.17 \times 10^{5} \pm 1.03 \times 10^{5}$

The data are reported as mean ± SEM. n≥3.

5.4.2 Advanced intestinal gut model validation

The most used *in vitro* intestinal model in toxicity assessment is represented by 21 days grown Caco-2 cells, which are able to differentiate forming a monolayer and assuming an enterocyte-like phenotype including the formation of TJs [149].

Despite this, enterocyte-like cells do not completely represent the gut epithelium that is made up from different specialized cell types. Among these, goblet cells and M-cells are able to produce mucus and to transport particles through the intestinal barrier, respectively [151,305–308]. In the toxicity assessment of ingested particles, it is important to consider the possible mucus-particles interaction that can enhance or hinder the epithelium reaching and interaction by the particles [309,310]. Moreover, thanks to the presence of TJs, the particles, due to their size, are unable to cross the intestinal epithelium by paracellular way unless the barrier is damaged. The enterocyte transcytosis is not possible for the bigger particles [311], which instead can cross the intestinal epithelium by M-cells [306,312] passing into the circulatory stream and having the possibility of reaching other locations in the body.

To make the gut model structure more realistic, in this study we decided to improve the intestinal *in vitro* model used in **Chapter 3** and **4** by adding to the Caco-2 culture also mucus-producing cells and M-cells.

To obtain the desired model, the HT29 cell-line treated with methotrexate (HT29-MTX) that allow their differentiation into goblet-like cells able to produce mucus in a physiological way and amount after 21 days of co-culture in a ratio 9:1 with Caco-2 cells was chosen as mucus-producing cells [306,313].To obtain M-cells we added lymphocytic Raji B cells in the Bl compartment the last 7 days of cell culture because they are well-known to be able to stimulate Caco-2 cells to acquire M-cell phenotype [306].

After 21 days of cellular growth on porous membrane inserts, the production of mucus and the successful differentiation into M-cells were verified by cells staining and microscope analysis.

As shown in **Figure 5.4A**, the mucus was found in cell monolayer when HT29-MTX cells were present in the co-culture (central and right panels), not when Caco-2 were cultured alone (left panel).

Similarly, M-cells were not found in Caco-2 monoculture (upper panels) and in Caco-2/HT29-MTX co-culture (central panels) (**Figure 5.4B**). Only after 7 days of incubation with Raji B cells (lower panels), the presence of M-cells was observed in the intestinal model (**Figure 5.4B**).

As further confirmation, the measurement of TEER was assessed observing a drastic decreasing of this value when the model was incubated with Raji B cells (**Table 5.3**), confirming the successful Caco-2 differentiation into M-cells which form a few amount of TJs [314,315], causing a reduction in TEER value.

Table 5.3. Transepithelial electrical resistance *of mono-, bi-, or tri-culture gut model.*

	Caco-2	**Caco-2/HT29-MTX**	**Caco-2/HT29-MTX/Raji B**
TEER (Ω x cm^2)	1113 ± 119.7	1065.75 ± 61.95	202.75 ± 3.25

Data are mean ± SEM. n=3

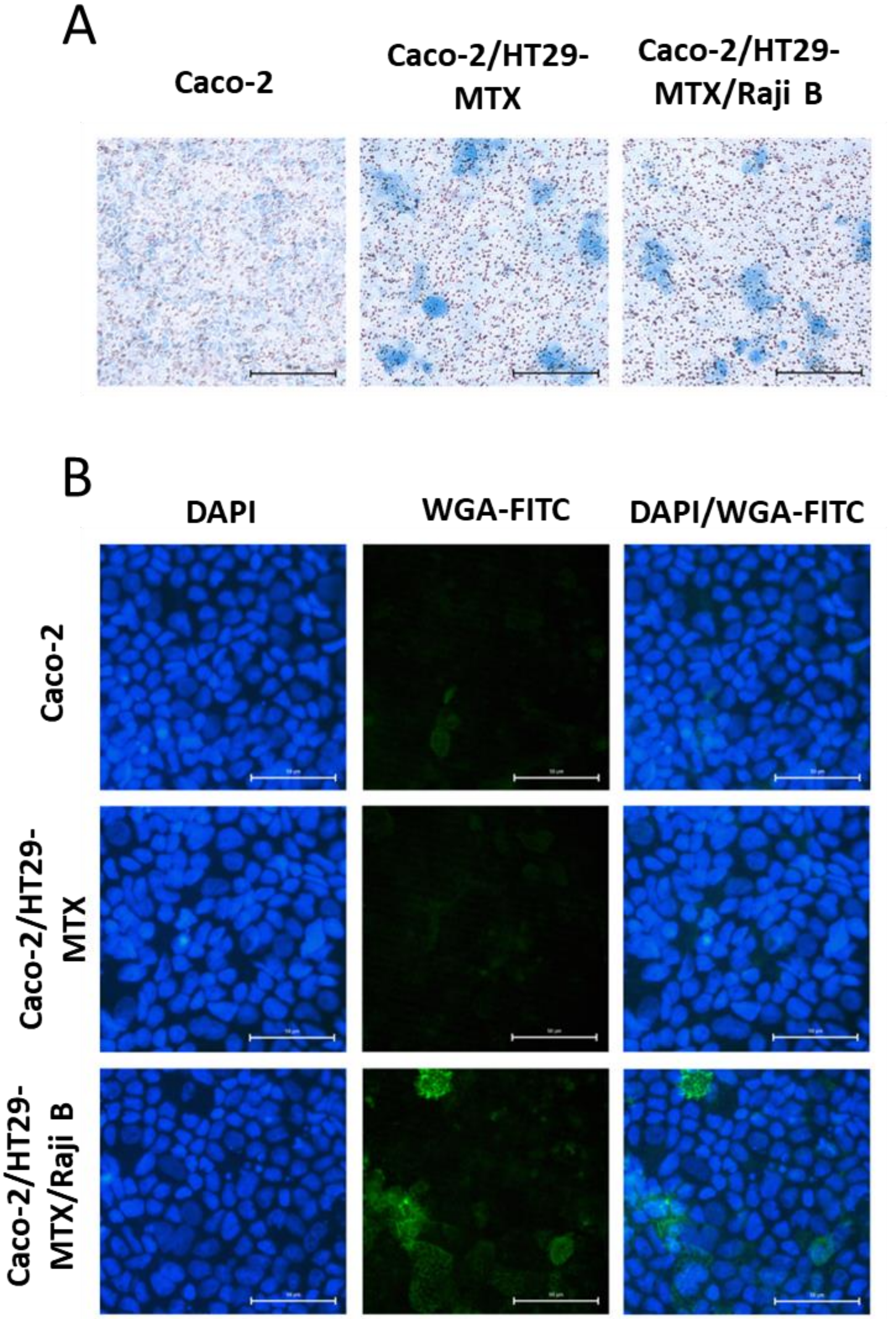

***Figure 5.4. Microscope analysis** of **A)** Mucus stained with Alcian Blue and **B)** M-cells stained with WGA-FITC (green). The nucleus was stained with DAPI (blue).*
Bar = 50 µm.

5.4.3 MPs evaluation as bacterial vehicle to the gut

As previously specified, MPs can be a vehicle of pathogens to the human gut thanks to their easy colonization by bacteria.

For this reason, we investigated the intestinal effects of bacteria-colonized MPs in case they are ingested.

We explored the acute exposure for 24 h on undifferentiated Caco-2 cells of pristine and SHDS-treated MPs in the absence or presence of *V. parahaemolyticus* biofilm.

The particles, previous incubated with the bacteria to allow the biofilm formation, were separated from free bacteria by filtering them from the supernatant and then recovering them in fresh medium to start the incubation with cells.

For pristine particles we did not observed any variation in cell viability (**Figure 5.5A),** but in the presence of *V. parahaemolyticus* the MPs became toxic with a significative dose-dependent trend of cytotoxicity starting from the lowest tested concentration (1 µg/ml) (**Figure 5.5A**).

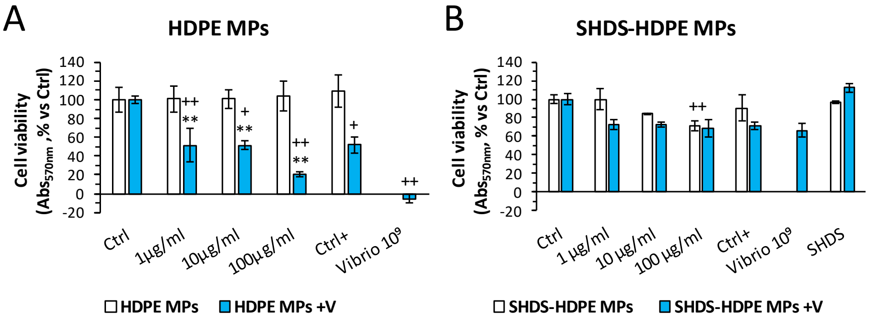

Figure 5.5. Caco-2 cell viability *after 24 h of incubation with* ***A)*** *pristine MPs with (+V) or without V. parahaemolyticus biofilm and* ***B)*** *SHDS-treated MPs with (+V) or without V. parahaemolyticus biofilm.*

V. parahaemolyticus 10^9 *CFU/ml represent the concentration in the filtrate.*

Ctrl + = V. parahaemolyticus 10^7 *CFU/ml*

SHDS = SHDS fluids concentration corresponding to the higher SHDS-MPs concentration used.

*Mean ± SEM. n=3. + p< 0.05 vs ctrl, ++ p< 0.01 vs ctrl, ** p<0.01 vs w/o biofilm.*

This cytotoxicity was accompanied by a dose-dependent induction of inflammation detected as IL-8 release (**Figure 5.6A**), that was absent for MPs without bacteria for the exception of highest concentration of MPs for which the IL-8 release was significatively increased, but always to a lower extent than in presence of the biofilm (**Figure 5.6A**). IL-6 and TNF-α release were also investigated as inflammatory indicators, but they were not detected (data not shown).

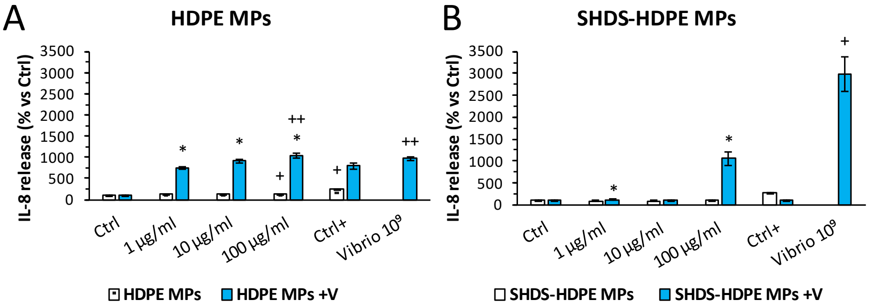

***Figure 5.6. Caco-2 IL-8 release** after 24 h of incubation with **A)** pristine MPs with (+V) or without V. parahaemolyticus biofilm and **B)** SHDS-treated MPs with (+V) or without V. parahaemolyticus biofilm.*

V. parahaemolyticus 10^{9} CFU/ml represent the concentration in the filtrate.

Ctrl + = V. parahaemolyticus 10^{7} CFU/ml
Mean ± SEM. n=3.
*+ $p< 0.05$ vs ctrl, ++ $p< 0.01$ vs ctrl, * $p< 0.05$ vs w/o biofilm.*

When MPs were subjected to SHDS a toxic effect with similar extent in the whole concentration range in presence of biofilm was detected (**Figure 5.5B**), along with a dose-dependent loss in cell viability for particles without bacteria that become significative at the highest concentration (**Figure 5.5B**). In the absence of biofilm the toxicity was not coupled to IL-8 release, on the contrary when bacteria were present, we found a significant IL-8 production at the highest concentration (**Figure 5.6B**). As for pristine particles, also in this case it was not found IL-6 and TNF-α release (data not shown). The lower toxicity and induction of inflammation of SHDS-treated MPs in presence of the bacterial biofilm could be explained by the reduction in number of viable bacteria on the MPs surface after treatment with SHDS (**Table 5.2**).

To confirm these results, we moved to an intestinal model that more closely represents the gut structure involving not only enterocyte-like cells, but even goblet cells and microfold ones, which validation is disclosed in the previous section (**5.2.2**).

Differently from what was observed on the simpler model, after 24 h of exposure no differences in cell viability were found for all conditions tested in the whole concentrations range (**Figure 5.7**).

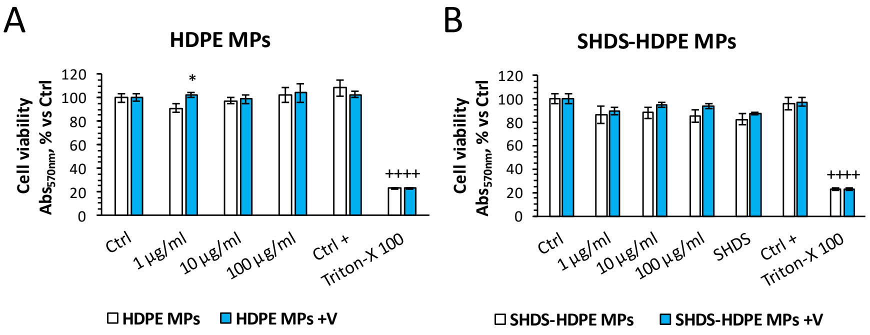

***Figure 5.7. Caco-2/HT29-MTX/M-cells co-culture model cell viability** after 24 of incubation with **A)** pristine MPs with (+V) or without V. parahaemolyticus biofilm and **B)** SHDS-treated MPs with (+V) or without V. parahaemolyticus biofilm.*

Ctrl + = V. parahaemolyticus 10^7 *CFU/ml*
SHDS = SHDS fluids concentration corresponding to the higher SHDS-MPs concentration used.
Mean ± SEM. n=3.
*++ p< 0.01 vs ctrl, * p< 0.05 vs w/o biofilm.*

These results were not paralleled by changes in TEER values (**Figure 5.8**) and LY passage (**Figure 5.9**), indicating the maintenance of the integrity and permeability of the barrier.

Unexpectedly, pristine MPs in presence of bacterial biofilm induced an increase in barrier integrity (**Figure 5.8**) accompanied by a decrease in barrier permeability (**Figure 5.9**), however these effects disappeared when the particles were subjected to SHDS. The possible activation of inflammatory processes was also investigated by measuring the release of some pro-inflammatory cytokines in the Bl compartment.

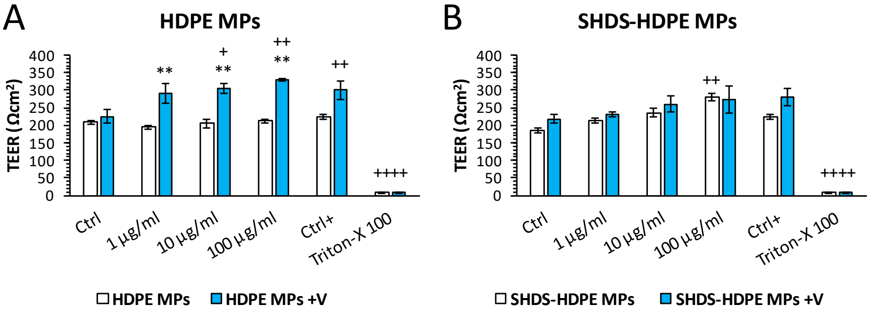

Figure 5.8. Caco-2/HT29-MTX/M-cells co-culture model barrier integrity *measured as TEER after 24 of incubation with* ***A)*** *pristine MPs with (+V) or without V. parahaemolyticus biofilm and* ***B)*** *SHDS-treated MPs with (+V) or without V. parahaemolyticus biofilm.*

Ctrl + = V. parahaemolyticus 10^7 *CFU/ml*
Mean ± SEM. n=3.
*+ p< 0.05 vs ctrl, ++ p< 0.01 vs ctrl, ** p<0.01 vs w/o biofilm.*

In accordance with what we observed on undifferentiated Caco-2 cells, only IL-8 was detected in the Bl supernatant, but not IL-6 and TNF-α. The condition for which IL-8 was released in a greater manner was MPs without biofilm after SHDS treatment that induced the IL-8 production in relation with the MPs concentration, albeit in a non-significative manner (**Figure 5.10**). Moreover, SHDS treatment slightly increased the release of this cytokine also in presence of bacteria at the highest MPs concentration (**Figure 5.10**).

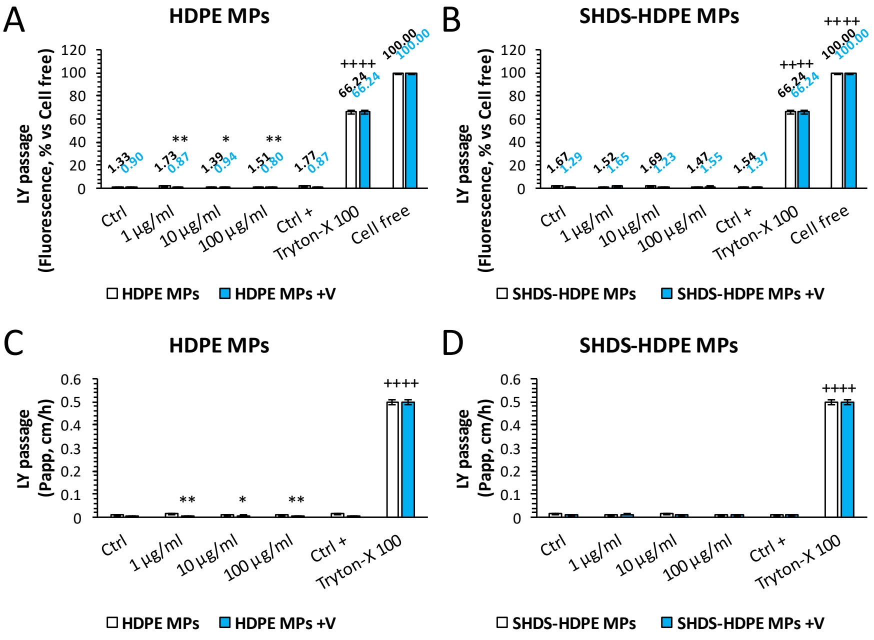

***Figure 5.9. Caco-2/HT29-MTX/M-cells co-culture model barrier permeability** after 24 of incubation with **A, C)** pristine MPs with (+V) or without V. parahaemolyticus biofilm and **B, D)** SHDS-treated MPs with (+V) or without V. parahaemolyticus biofilm, expressed as **A, B)** percentage vs Cell free inserts or **C, D)** Papp cm x h.*

Mean ± SEM. n=3. Ctrl + = V. parahaemolyticus 10^7 CFU/ml
*++ p< 0.01 vs ctrl, * p< 0.05 vs w/o biofilm, ** p<0.01 vs w/o biofilm.*

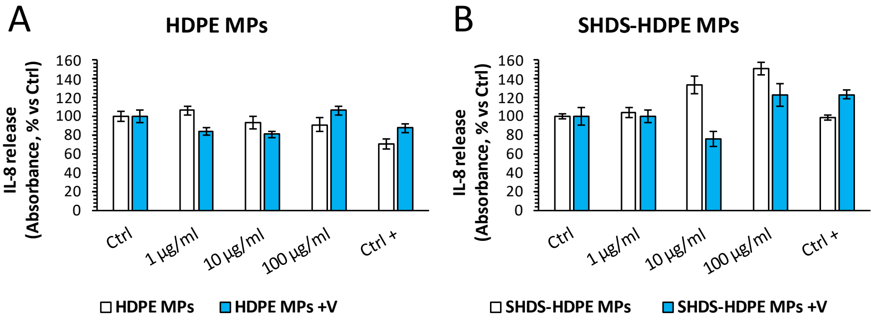

***Figure 5.10. Caco-2/HT29-MTX/M-cells co-culture model pro-inflammatory cytokines release** after 24 of incubation with **A)** pristine MPs with (+V) or without V. parahaemolyticus biofilm and **B)** SHDS-treated MPs with (+V) or without V. parahaemolyticus biofilm.*

Ctrl + = V. parahaemolyticus 10^7 CFU/ml
Mean ± SEM. n=3.

5.4.4 Assessment of MPs chronic exposure consequences on intestinal barrier models

As MPs are ubiquitous, humans are continuously exposed to them. In consequence, we also explored the intestinal chronic exposure incubating the cells for 4 h a day for 4 weeks with pristine and SHDS-treated MPs. Unfortunately, in this case it was not possible to study the effects of bacterial biofilm as bacteria grow fast, affecting the cell culture during a small time.

Since, undifferentiated Caco-2 cells cannot be maintained in culture for a such long time, therefore we chose to perform cell viability and inflammation on 21 days-grown Caco-2/HT29-MTX co-culture exposed to MPs in a concentration range between 1 and 100 µg/ml.

Before this, we verified the absence of toxicity induction following the exposure of SHDS fluids alone at the corresponding concentrations used for SHDS-MPs exposure (**Figure 5.11A**).

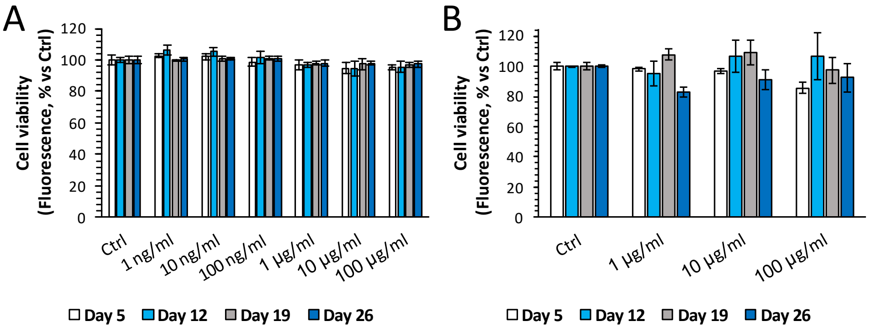

Figure 5.11. Cell viability** of* ***A) *Caco-2/HT29-MTX, and* ***B)*** *Caco-2/HT29-MTX/M-cells co-culture models after 4 hours-daily exposure with SHDS fluids only. Mean ± SEM. n=3.*

After exposure to pristine or SHDS-treated MPs we did not find any significant variation in cell viability along the whole period and for all concentrations tested (**Figure 5.12**).

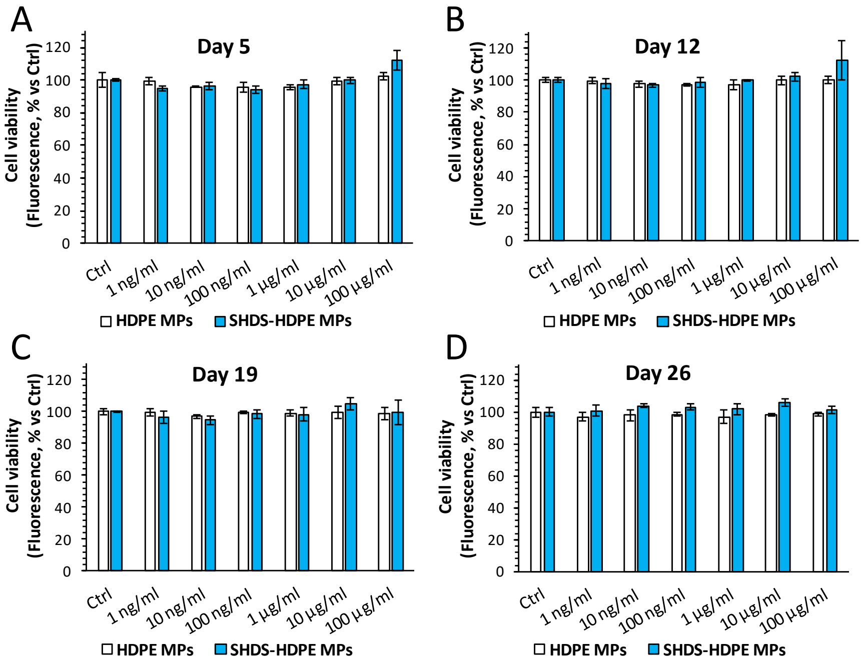

***Figure 5.12. Caco-2/HT29-MTX co-culture model cell viability** after **A)** 5 days, **B)** 12 days, **C)** 19 days, and **D)** 26 days of 4 hours-daily exposure with pristine or SHDS-treated MPs. Mean ± SEM. n=3.*

Considering these findings, we moved to the more complex co-culture model previously described in **section 5.2.2** to evaluate if the compartmentalisation and the presence of M-cells could influence the outcome of cell survival and inflammation. Since no variation in analysed parameters was observed for the lower concentrations, we decided to investigate the effects only of the 3 highest concentrations (i.e., 1-100 µg/ml).

At the end of each week of exposure, the cell viability was assessed by using Alamar Blue reagent. As for the simpler model, the absence of SHDS fluids-induced cytotoxicity was previously verified (**Figure 5.11B**). Consistently with Caco-2/HT29-MTX co-culture results, no decrease in cell viability was found for both pristine and SHDS-treated MPs in the whole concentration range (**Figure 5.13**).

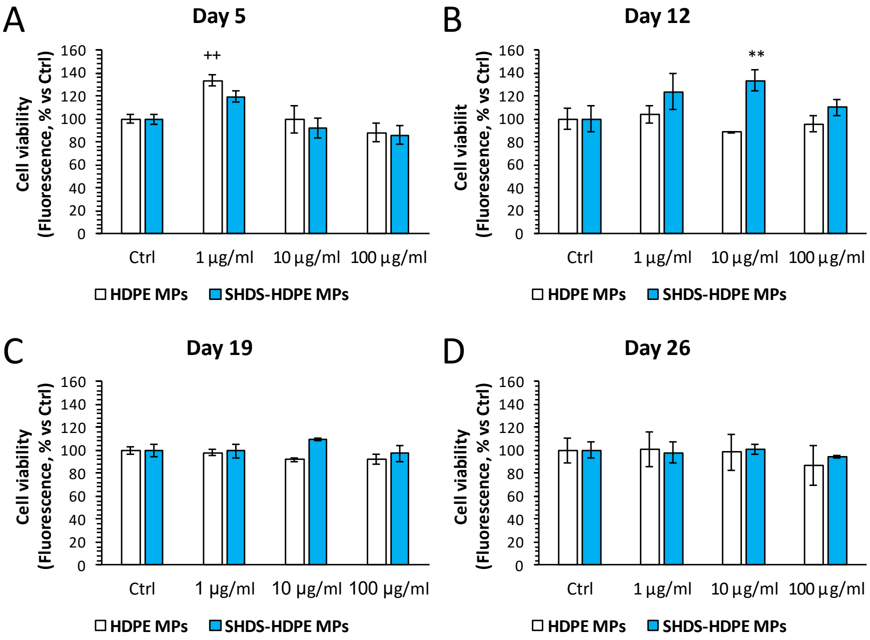

Figure 5.13. Caco-2/HT29-MTX/M-cells co-culture model cell viability *after* ***A)*** *5 days,* ***B)*** *12 days,* ***C)*** *19 days, and* ***D)*** *26 days of 4 hours-daily exposure with pristine or SHDS-treated MPs. Mean ± SEM. n=3.*
*++ p< 0.01 vs ctrl, ** p<0.01 vs pristine MPs.*

The barrier integrity was also evaluated without observing any decrease in this parameter (**Figure 5.14**), even if the TEER showed a dose-dependence increased values during the first 2 weeks of exposure (**Figure 5.14A and B**). Interestingly, this increase was higher when the particles were treated with SHDS. The values were then stabilised at the value of the control in the last 2 weeks (**Figure 5.14C and D**).

The BI release of pro-inflammatory cytokines IL-8, IL-6, and TNF-α was investigated as markers of inflammation, without finding significant variation in IL-8 in the whole range of time and concentration (**Figure 5.15**). In accordance with previous results, no detectable levels of IL-6 and TNF-α were found.

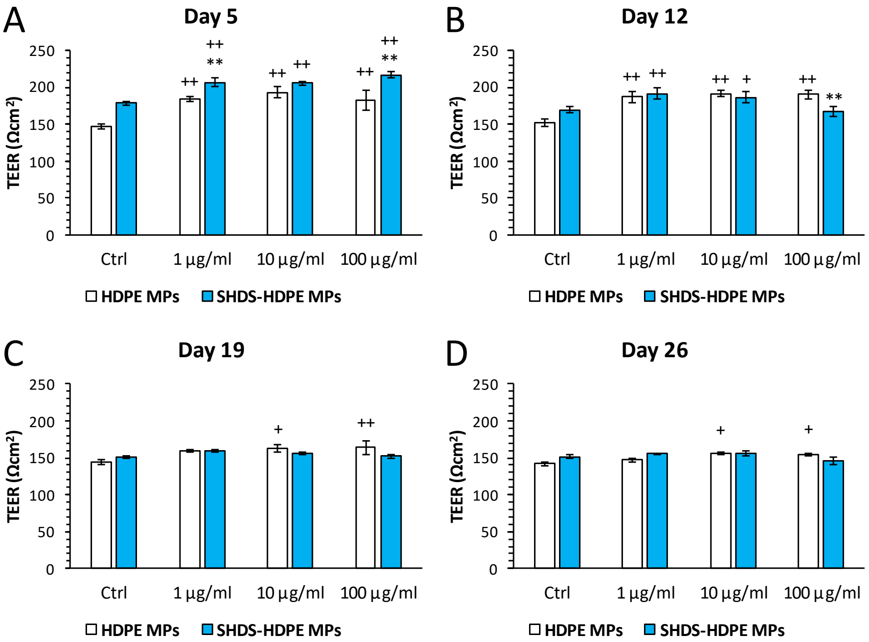

Figure 5.14. Caco-2/HT29-MTX/M-cells co-culture model barrier integrity *after* ***A)*** *5 days,* ***B)*** *12 days,* ***C)*** *19 days, and* ***D)*** *26 days of 4 hours-daily exposure with pristine or SHDS-treated MPs. Mean ± SEM. n=3.*
*+ p< 0.05 vs ctrl, ++ p< 0.01 vs ctrl, ** p<0.01 vs pristine MPs.*

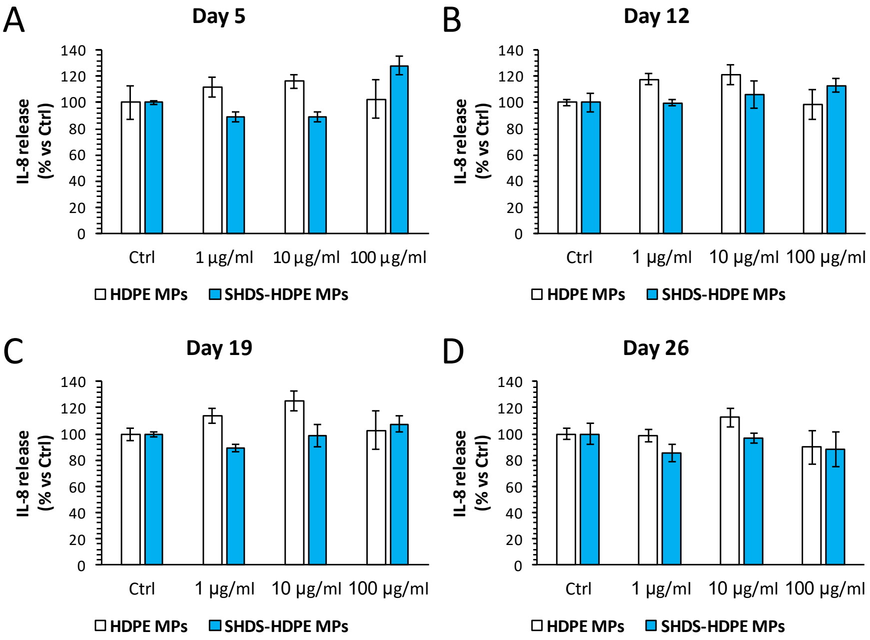

Figure 5.15. Caco-2/HT29-MTX/M-cells co-culture model IL-8 release** after* ***A) *5 days,* ***B)*** *12 days,* ***C)*** *19 days, and* ***D)*** *26 days of 4 hours-daily exposure with pristine or SHDS-treated MPs. Mean ± SEM. n=3.*

5.4.5 Effect of applying dynamic conditions on MPs exposure effects on intestinal barrier model

As mucus and M-cells are very important to a more in-depth assessment of MPs intestinal effects, the dynamic conditions present in the intestine (e.g., flow, pressure) are too.

To explore the role of these conditions in the effects evaluation of ingested MPs, we used a millifluidic device to reproduce on tri-culture intestinal model the physiological flow that allows to reach the physiological pressure found in human gut [300].

We used a sub-chronic exposure of 5 days, exposing the cells to MPs for 4 h a day, since the cell growth for a longer period is difficult in a millifluidic device. Intestinal model grown on porous membrane inserts and in LB2 support (*IVTech, Massarosa, Italy*) were exposed to the highest dose used in previous experiments (i.e., 100 µg/ml), as we did not observe great effect of MPs on static model up to 5 days.

At the end of the exposure time, barrier permeability, mucus secretion, and inflammation were evaluated. In static condition we observed an increased barrier permeability greater when particles were subjected to SHDS (**Table 5.4**). Instead, there were no differences in LY barrier crossing in the dynamic model (**Table 5.4**).

Table 5.4. Apparent permeability of Caco-2/HT29-MTX/M-cells gut model under static or dynamic conditions *after 5 days of 4h-daily exposure to HDPE MPs treated or not with SHDS.*

P_{app} (cm/h)	**Static**	**Dynamic**
Ctrl	$4.72 \times 10^{-2} \pm 9.66 \times 10^{-3}$	$2.57 \times 10^{-2} \pm 1.55 \times 10^{-3}$
HDPE	$6.80 \times 10^{-2} \pm 3.02 \times 10^{-2}$	$2.57 \times 10^{-2} \pm 4.39 \times 10^{-3}$
SHDS-HDPE	$8.60 \times 10^{-2} \pm 1.31 \times 10^{-2}$	$2.71 \times 10^{-2} \pm 1.53 \times 10^{-3}$

Data are Mean ± SEM. n=3.

To verify if MPs could also affect the mucus layer, a staining with Alcian Blue was performed: no qualitative differences with respect to the control for all conditions tested in both used models (**Figure 5.16**). Interestingly, the mucus covering the cells is more abundant forming a complete layer when the model was subjected to dynamic conditions (**Figure 5.16**).

To evaluate the possible induction of inflammation, the presence of pro- and anti-inflammatory cytokines was analysed by ELISA in the Bl medium. Anti-inflammatory cytokines IL-10 and IL-22 were not detected for all condition tested (data not shown), but an increased release of pro-inflammatory TNF-α was found only in static conditions (**Figure 5.17**), by using an improved and more sensitive protocol compared to previous experiments. Moreover, the measured amount of this cytokine was greater when MPs were treated with SHDS (**Figure 5.17**).

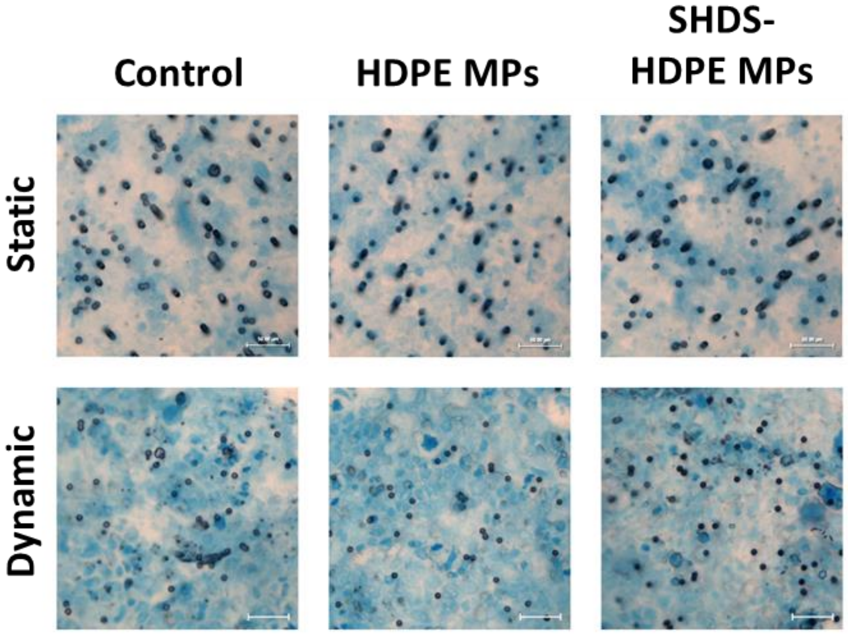

Figure 5.16. Mucus staining *with Alcian Blue of Caco-2/HT29-MTX/M-cells co-culture model in static or dynamic conditions after incubation with HDPE MPs before and after treatment with SHDS.*

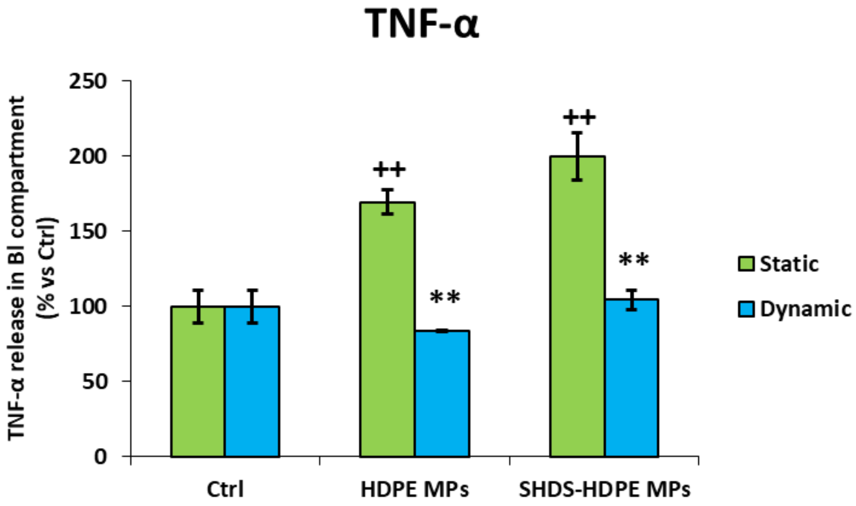

Figure 5.17. Caco-2/HT29-MTX/M-cells co-culture model TNF-α release *after 5 days of 4 hours-daily exposure with pristine or SHDS-treated MPs under static or dynamic conditions. Mean ± SEM. n=1. ++p<0.01 vs Ctrl; **p<0.01 vs pristine.*

The results presented in this section are just preliminary results that need further confirmation on permeability and barrier integrity parameters.

All the results discussed in this chapter are summarized in **Table 5.5**.

Table 5.5. *Resume of the Chapter 5 results.*

Endpoint	**Results**
V. parahaemolyticus biofilm formation on MPs	After 48h of incubation, *V. parahaemolyticus* successfully colonised HDPE MPs surface forming a dense biofilm
Effect of SHDS on MPs and on *V. parahaemolyticus* biofilm	After SHDS treatment the number of viable bacteria on MPs surface consistently decrease and they are not still visible in SEM images. The particles showed a biological covering
Advanced intestinal gut model validation	The Caco-2/HT29-MTX/Raji B cells co-culture successfully produce mucus and contain M-cells derived by Raji B-induced differentiation of Caco-2 cells
MPs evaluation as bacterial vehicle to the gut	On undifferentiated Caco-2 cells, the MPs with bacterial biofilm caused a significant decrease in cell viability and an increase of IL-8 release. After digestion this trend was less visible. On barrier model, neither decrease in cell viability and barrier integrity nor increased in barrier permeability and IL-8 release were found. An increased in TEER values was observed in presence of bacterial biofilm
MPs chronic exposure on intestinal barrier models	Neither decreased in cell viability and barrier integrity nor increased in IL-8 released were found up to 4 weeks of exposure. During the first two weeks an increased in TEER values was observed for both pristine MPs and SHDS-treated MPs
Effect of applying dynamic conditions on MPs exposure effects on intestinal barrier model	Dynamic condition allowed to obtain a more consistent mucus layer. If for static model increased permeability and TNF-α release were observed, in particular for SHDS-treated MPs, for dynamic model no changes were found for both parameter

5.5 Discussion

MPs are now ubiquitous in the environment and their amount is rising over time, increasing the possibility of human exposure. Yet, the effects of MPs on the human body have not been completely understood [35].

Despite one of most common routes of contact with humans is represented by ingestion through the food, an advanced and validate *in vitro* gut model to study the possible effects that MPs can exert on the intestine is not still available.

Currently, the most common gut models are not representative enough of the complex anatomy and physiology of the intestine. Therefore, it is needed to improve the current models to obtain a more representative one that allow to better predict *in vitro* the possible consequences of MPs ingestion.

Trying to fill this gap, in this work we have implemented in various aspects the simplest and most used *in vitro* gut model represented by the monoculture of Caco-2 cells. In particular, we developed a platform in which the possible bacterial contamination, the main cell types, the possible MPs changes occurring during the digestion process and the dynamic environment of the gut are considered, by adding to the Caco-2 culture goblet-like and M-cells, applying a SHDS and employing a millifluidic device to reach physiological flow and pressure.

5.5.1 Microplastics as microbial carrier to the gut

It was already reported that the environment-dispersed MPs can be quickly colonised by human pathogens [114,316] and that then they can be ingested through the food [317–320].

Confirming the previous findings, we verified the actual ability of HDPE MPs to act as a scaffold for *V. parahaemolyticus,* one of most foodborne pathogens that can reach the small intestine causing gastro-intestinal symptoms and in worst cases even septicaemia [321,322]. As this bacterium have the ability to disrupt the intestinal villi [321], in presence of *V. parahaemolyticus* HDPE MPs caused a dose-dependent loss in Caco-2 cell viability likely due to the induction of inflammation as indicated by the increase of IL-8 release that is already reported as the results of the mitogen-activated protein kinases stimulation via *V. parahaemolyticus* VP1680 effector protein [323].

Despite its resistance to gastric low pH [321,322], after SHDS treatment the *V. parahaemolyticus* CFU number on MPs surface decreased under the 50% of the non-treated MPs, similarly to what found by Wang and co-workers after *V. parahaemolyticus* subjection to SGF [324]. These results can explain the lower toxicity and inflammation induction after treatment with SHDS found on undifferentiated Caco-2 cells for the lower MPs concentrations. In fact, as suggested by Lynch and co-workers, the production of enterotoxic hemolysins is not sufficient to induce toxicity on Caco-2 cells barrier model supposing that the specific toxicity it could be mediated by a type III secretion systems that requires the contact with cells to exert the toxic effects [325]. Unfortunately, we are not able to exclude the possibility of *V. parahaemolyticus* adhesion to the culture plate and if SHDS-treatment can affect the entity of this process. Interestingly, the SHDS treatment leads to a decrease in cell viability even in absence of bacterial biofilm as already observed for TiO_2 nanoparticles on Caco-2 cells [162] and for iron particles on human liver cells [325].

However, this cellular model does not reflect well the gut epithelium structure and physiology. For instance, it does not consider the importance of the mucus layer [326–328] and of M-cells [306,315,329] in the particles/bacteria-cells interaction and their absorption through the gut.

The 9:1 ratio of Caco-2/HT29-MTX cells successfully led to an increase in mucus secretion: it has been already reported as the best ratio to obtain a physiological amount of mucus [152,330]. Moreover, the successful Caco-2 differentiation into M-cells was verified by WGA staining and TEER measurement that decrease due to the weaker junction strength than that formed by enterocytes [314,315]. On this model the effects of the HDPE MPs with biofilm on cell viability were lost likely due to the more sensitivity of undifferentiated Caco-2 cells compared to the more advanced models [214,331]. Surprisingly, barrier integrity increased, and barrier permeability decreased in a dose-dependence manner in presence of *V. parahaemolyticus* biofilm suggesting a compensation mechanism actuated to preserve the barrier homeostasis. Recently, other works have reported an increase in TJ-related genes after exposure to nanomaterials [190] or an *E. coli*-induced increased TEER [332], making our hypothesis stronger. However, after SHDS treatment both in the absence and presence of bacterial biofilm the above-mentioned trend was also observed, albeit in a non-significative manner, suggesting that the treatment induces an adaptive mechanism and that since the number of CFU decreases after SHDS, the effects was lower than that induced by pristine particles. The gain in barrier integrity was accompanied by the dose-dependence increase in IL-8 release only for SHDS treated particles without biofilm, albeit not in a significant way, suggesting an initial induction of inflammation that probably trigger a compensatory mechanism of upregulation of TJs. Ongoing experiments are setting up to demonstrate our hypothesis. Despite in literature the release of pro-inflammatory cytokines after intestinal cells exposure to nano/micro-particles have been largely reported [333–336], no studies which also consider the possible transformation during the digestion process was found. However, in **Chapters 3** of this thesis we reported an increase in pro-inflammatory cytokines IL-6 and TNF-α after nanomaterials exposure to Caco-2 gut model that was higher when the particles were treated with SHDS.

5.5.2 Effects of MPs long- and medium-term exposure to the gut model

Humans are constantly exposed to MPs; in fact, it was estimated that a person ingests on average 458000 - 3569000 MPs/ year [337]. As it happens for different types of particles, the acute effects do not always reflect the chronic ones. An example of this difference is reported by Visalli and co-workers who observed an increased mortality rate and a significant ROS production after 24 h of HT29 intestinal cells exposure to polystyrene (PS) MPs, but in a sub-chronic condition (i.e., 48 days) this effect decreased, probably due to the cell adaptation [338]. Another example can be found in the work of Lebedová and colleagues in which the acute or chronic exposure of mice to CdO NPs was observed to lead to different Cd accumulation in the organs that was higher for the chronic condition. Moreover, morphological alteration and tissue damage were observed only after chronic exposure[339].

In addition, the average of intestinal transit timing has been estimated to be around 4 h [340]. For this reason, to better mimic the real situation, we explored the possible effects of a long-term intestinal exposure to HDPE MPs incubating the simpler co-culture of Caco-2 and HT29-MTX cells and the previously described tri-culture model with the particles 4 h /day for 4 weeks. For both models no cell viability nor inflammation changes occurred. However, a we found a significant increase in TEER values in the firsts 2 weeks of exposure indicating a probable adaptation mechanism of the cells. Similarly, after 24 h of exposure to Ag nanoparticles, the co-culture of Caco-2/THP-1 cells showed an increased TEER value with respect to the control [341]. Also, Schulze and colleagues reported an increased TEER values after 6 h or 24 h of Calu-3 sub-bronchial gland cells exposure to different types of particles: AlOOH, TiO_2, and CeO_2 nanoparticles [342], reinforcing our hypothesis.

In summary we did not observe any notable sign of cell damage or perturbation, but an important element was neglected in the cellular model set up: the dynamic condition within the intestine. As a matter of facts, in the small intestine are present physiological flow and pressure that have an important role in the intestinal barrier properties and intestinal maintenance, but they could also influence the particles-cells interaction leading to a possible different outcome of cellular exposure to MPs [300]. To overcome this lack, we decided to employ a millifluidic device that mimics physiological physical parameters of the intestine.

It was previous demonstrated that dynamic conditions induce a reduction of the required time for differentiation of HT29-MTX cells and allow to reach a more physiological cellular organization and a generation of thicker layer of mucus [343]. Similarly, we observed a higher quantity of produced mucus that formed a complete layer on the cells when they were subjected to a physiological flow. However, comparing to the control, no changes were observed after incubation with HDPE MPs, both pristine and SHDS-treated.

In this case, a significant difference in the permeability and inflammation, measured as TNF-α release. was found between static and dynamic conditions after 5 days of exposure (4 h/ day). Both parameters were increased when the model was static, but no changes were found in the dynamic ones. It was previously demonstrated that Caco-2 cells cultured in the same millifluidic device used in this work showed an increased barrier integrity coupled with a higher quantity of TJs formation [300]. This increased barrier function makes the epithelium more compact: this could explain its higher resistance to MPs exposure in terms of permeability perturbation. Moreover, the dynamic flow could modify the cells-MPs interaction, altering the number of contacts, as previously demonstrated for other types of cells/tissue models exposed to NPs. Recently, Burns and co-workers observed that the physiological dynamic flow on adherent U937 endothelial cells resulted in a decrease in silver nanoparticles deposition consequently accompanied by a reduction in the oxidative stress [344]. On the contrary, when the cells were in suspension, the flow effect was the opposite, resulting in a higher frequency of contact and increased ROS production by cells [344]. Similarly, in another study it was found a smaller deposition rate of gold nanoparticles on A549 alveolar cells when a physiological flow was applied [345].

Since this last part of this chapter is composed by preliminary data, other tests studying the expression of TJ protein and other inflammatory/ anti-inflammatory cytokines, will be carried out in order to confirm the results.

5.6 Conclusions

In this chapter we demonstrated that the MPs could be a suitable scaffold for *V. parahaemolyticus* biofilm having the potential to serve as a vehicle of these bacteria to the human intestine. Moreover, we proved that the results can be different if obtained using a static monoculture or an organotypic dynamic culture model: in fact, by making the cellular model more complex and closer to the physiology, we obtained a different response. On the other hand, we are aware that the lack of immune cells and microbiota components makes the organotypic model still incomplete. The work of this chapter could be the starting point to develop intestinal models closer to human physiology to study in depth and in an accurate way the consequence of ingested MPs.

6 Inter-laboratory validation of an *in vitro* platform to evaluate the induction of oxidative stress by nano-materials

This chapter is focused on the Round Robin test performed in the context of the European Project BIORIMA. As suggested by the intrinsic meaning of the term used to describe this typology of studies, as part of the UNITO working group my contribution is restricted to a single type of experiments, namely "NRF2 reporter gene assay".

However, in this type of test each single contribution is important in order to increase the size of the statistical population on which the analyses are performed and consequently to make the results of the work more significant.

6.3 Materials and methods

6.3.1 Materials and Reagents

The reagents, cells and NBMs were common to all the participating laboratories. DMEM/F12 without phenol red, Trypsin 0.5% EDTA (10x), NEAA, FBS, dextran-coated charcoal-stripped foetal calf serum (DCC-FCS) and phosphate-buffered saline, were from Gibco (California). Curcumin, dichlorvos and mannitol were purchased from Sigma Aldrich (Amsterdam, Netherlands). Dimethyl sulfoxide (DMSO) was purchased from Acros Organics (Belgium), while geneticin (G418) from Duchefa (Haarlem, Netherlands), and P/S from Invitrogen (Netherlands).

6.3.2 Nanobiomaterials

Fe_3O_4-PEG-PLGA (FNPs) nanomaterials were provided by Colorobbia Holding S.p.A (Firenze, Italy) as early described in **section 3.1.2** of this thesis, while Ag nanoparticles (NM300K) and TiO_2 nanoparticles (NM101) were obtained from the Joint Research Center of the European Commission (Italy), respectively in suspension and in powder. NM101 was suspended following the Nanogenotox protocol [52].

6.3.3 Small Angle X-ray Scattering (SAXS)

After being incubated for 18 days at 37°C in cell culture medium supplemented with 4% v/v FBS, 1% v/v Glutamax (Invitrogen), 1% v/v NEAA, 1% v/v sodium pyruvate (Sigma-Merck), 1% v/v P/S and 1% v/v HEPES, the dissolution and aggregation of the Ag nanomaterials was observed by small angle X-ray scattering (SAXS) (Invitrogen, Netherlands).

SAXS measurements were performed in Kapton capillaries using the high-resolution X-ray spectrometers Xeuss 2.0 (Xenocs) and ChemSaxs (lab design, CEA) at a concentration of 0.5 mg/ml. PySAXS software [346] was used to fit the data after subtracting the baseline signal. One of the cooperating laboratories conducted SAXS experiments.

6.3.4 Transmission Electron Microscopy (TEM)

A FEI TECNAI F20 microscope operating at 200 keV was used for the TEM experiment. The suspension was drop-casted onto a gold grid-supported, holey carbon film. After that, the sample was dried at 60 °C. Phase contrast and high-angle annular dark-field scanning transmission modes (HAADFSTEM) were used to capture the images in order to learn more about the morphology of the particles.

The crystalline phase structure and content were examined using high resolution (HREM) and selected area electron diffraction (SAED) analyses. More than 100 particles were measured in order to determine the mean particle diameter.

One of the cooperating laboratories conducted TEM experiments.

6.3.5 Dynamic Light Scattering (DLS)

FNPs hydrodynamic diameters and zeta potential were determined as previously disclosed in the NANoREG project [347]. In brief, endotoxin-free water or medium with or without FBS were used to modify the concentrations of the test samples from their corresponding stock suspensions of 1 mg/ml to a concentration of 25 µg/ml for the measurements. Malvern Zetasizer Nano ZS was used to determine the zeta potential and particle size distribution of the test materials using respectively the ELS and DLS methods. Particle size distribution and zeta potential values of each test material were measured three times, without pausing, at 0 and 24 h at a temperature of 25°C. One of the cooperating laboratories conducted DLS tests.

6.3.6 Endotoxin Detection

According to prior descriptions [348,349], the Limulus Amoebocyte Lysate (LAL) assay was utilized to find bacterial endotoxin contamination. The Limulus Amoebocyte Lysate PYROTELL®-T test (Associates of Cape Cod, Inc., East Falmouth, MA) was utilized in accordance with the manufacturer's instructions. PYROS® Software was used for data analysis (Associates of Cape Cod, Inc., East Falmouth, MA).

6.3.7 Cell culture

Bio Detection Systems (BDS) (Netherlands) kindly provided U2OS-NRF2 cells. In the human osteoblastic osteosarcoma U2OS-NRF2 cells, four distinct EPRE sequences are expressed, including the consensus EPRE (TCACAGTGACTAAGCAAAAT), the hNQO1 EPRE (TCACAGTGAC TCAGCA-GAAT), the hGCLM EPRE (AGACAATGACTAAGCAGAAA), and the hGCLC EPRE (TCACAGTGAC TCAGCA-GAAT) (TCACAGTCAGTAAGTGATGG) [350]. The two oligos were linked to generate the luciferase reporter construct pLuc, which lacks a promoter. Because the NRF2 pathway is expressed naturally in U2OS cells, a selection construct (pSG5-neo) was employed. The cells were grown in DMEM/F12 supplemented with 10% v/v FCS and 1% v/v P/S.

To keep the selection pressure high, 200 g/ml G418 was added to the culture medium once a week. Cells were kept at 37 °C in a humid environment with 5% CO_2.

6.3.8 Cell viability assay

The Alamar blue® (resazurin) assay (Thermo Scientific, Sweden) was used to determine the cytotoxicity of NBMs [351]. Prior to the "round robin" pre-validation studies, one of the participating laboratories conducted the cell viability tests. Trypsinization, counting, and resuspension of the cells were performed before they were added to cell culture medium devoid of phenol red and supplemented with 5% v/v DCC-FCS, with a final concentration of 10^4 cells per well (100 µl).

Cells were seeded in 96-well plates and either maintained in DCC-FCS alone (negative control) or subjected to test items. To track cellular metabolic activity, the assay reagent was applied to each well (10% v/v). Using a spectrophotometer (Tecan Infinite® F200), the samples were examined.

6.3.9 Reporter gene assay

By monitoring the induction of luciferase activity in the NRF2-U2OS cells, the potential of NRF2 mediated gene expression induction by NBMs was examined. Briefly, in a 96-well plate without using the exterior wells, the cells were trypsinised, counted, and resuspended in cell culture media without phenol red and supplemented with 5% v/v DCC-FCS. The plates were incubated for 24 h at 37°C with 5% CO_2 in a humid environment. After this pre-incubation, one reference plate was exposed to 9 serial dilutions of the reference substance curcumin, ranging in concentration from $1X10^{-4}$ M to $1X10^{-8}$ M ($\log_{10}$ dilution steps), as well as the positive control dichlorvos ($1X10^{-}$

^{5} – 1X10^{-7} M) and the negative control mannitol (1X10^{-3} – 1X10^{-5} M). Dichlorvos was used as a positive control because it is well known to cause a reaction in this test, but mannitol should not. As curcumin typically produces a dose-effect response in the current experiment, it was chosen as the reference molecule. The compounds from a 200-fold concentrated stock solution in DMSO were added to the exposure medium (5% v/v DCC-FCS in DMEM/F12 without phenol red), which was used to expose the cells to the reference compounds. Cells underwent additional processing for the luciferase induction assay after being exposed to the test materials. Cells were rinsed in PBS before being lysed in 30 µl of low salt buffer (Tris, 25 mM, DTT 2.0 mM, CDTA 2.0 mM), which was followed by freezing at 80°C to ensure thorough cell lysis. In order to measure luciferase, a flash mix methodology was used (BDS, Netherlands). The illuminate mix, also known as the flash mix, contains 20 mM tricine, 1.07 mM $(MgCO_3)_4$ Mg(OH)2.5 H_2O, 2.67 mM $MgSO_4$ x 7 H_2O, EDTA 0.1 mM, DTT 1.5 mM, D-Luciferine 539 mM, and ATP 5.49 mM. Using a luminometer with two injectors—one to start the reaction by adding the Luciferin contained in the illumine mix and one to stop the enzymatic reaction with NaOH- the measurements were performed in the different laboratories. In order to stop the reaction, 100 µL of 0.2 M NaOH was added. As previously mentioned, an induction factor threshold of 1.5 was established for the NRF2 mediated gene expression [350].

In order to exclude any interference of the materials with the luciferase activity, the U2OS-NRF2 cells were fixed at the end of exposure by adding 50 µl of paraformaldehyde at 4% v/v in PBS for 30 min at room temperature just before cell lysis to carry out the luciferase induction assay as described above.

6.3.10 Design of “round robin” pre-validation

During the current work, FNPs were chosen as a representative and innovative NBM. Both therapeutic and diagnostic uses for these nanoparticles are envisioned. The "benchmark" NM101 NMs were included as an inert (non-cytotoxic) nanomaterial and the NM300K NMs were included as a nanomaterial that most likely would elicit NRF2 mediated gene expression. Cytotoxicity at higher concentrations of the latter nanomaterials, however, could not be excluded. Based on the manufacturer's recommendations, additional positive and negative chemical controls (dichlorvos and mannitol) were added for the test.

The NRF2 reporter gene assay, quality control procedures, and data analysis were all explained to the collaborating laboratories (see **Figure 6.1** for a flowchart of the process). Karolinska Institute, Wageningen University, University of Turin, University of Grenoble-Alpes, Edinburgh Napier University, University of Rome Tor Vergata, University of Paris Cité, and Tokyo University of Science were among the institutions that took part in the pre-validation study. The data are presented separately because one of these laboratories only examined FNPs and not the other "benchmark" nanomaterials. In-person meetings and online courses were used to debate and decide on protocols.

Hence, each experiment consisted of three experimental plates and one reference plate.

Each experimental plate had a full concentration range of the reference substance curcumin dissolved in DMSO, as did the reference plate three upper rows. The positive and negative controls (reference plate) or one of the three NBMs under examination (FNPs, NM101, NM300K) were in the lower section. The exposure settings were harmonized among the collaborating laboratories as well. As a result, FNPs and AgNM300K NMs were diluted from a stock of 3000 µg/ml in dispersant at a concentration range of 0.21 µg/ml to 3000 µg/ml, then underwent a second 30 x dilution step in exposure medium to an exposure range of 0.001-100 µg/ml. For NM101, the NANOGENOTOX dispersion procedure was used to create newly generated suspensions [52].

The reporter cells were exposed for 24 h in a humid environment with 5% CO_2 at 37°C.

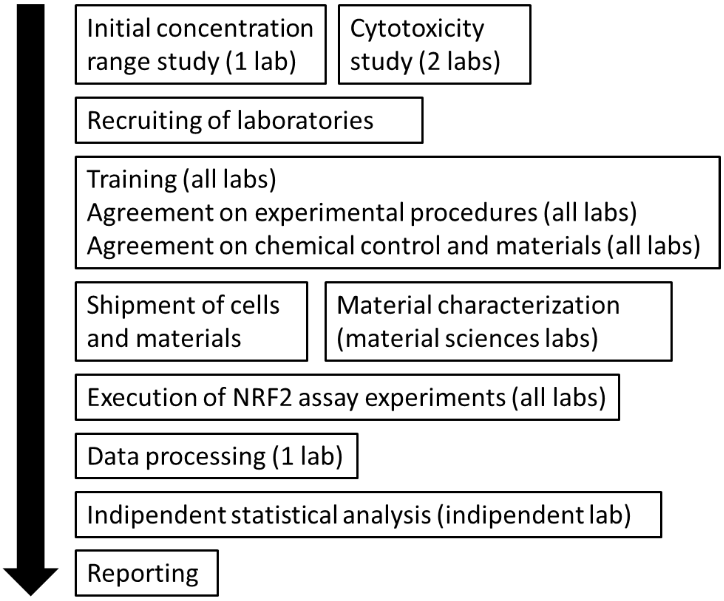

Figure 6.1. Pre-validation process workflow. *The number of involved labs is indicated. Edited from Martin et al., 2022* [352].

6.3.11 Data Analysis

Microsoft Excel was used to export the data for further processing.

The viability percentage toward the cells not exposed was used to express cytotoxicity. The Induction Factor (IF), which is the measured relative light unit (RLU) value divided by the mean RLU value of the solvent control, was used to display the results for the NRF2 reporter gene tests. The NRF2-U2OS reporter gene test was considered to be successful when the induction factor of curcumin was over 8. Inducers of NRF2 mediated-gene expression were samples with an induction of 1.5-fold or greater [350].

Prism 9.0 (GraphPad Software, Inc.) was used to create the graphs after non-linear curve fitting was used to analyse the data (agonist versus response). The intra-laboratory and inter-laboratory standard deviations were determined across all NRF2 reporter gene assay results and presented in a heatmap to assess the variability of results and reproducibility of the assay. Version 8.3.0 of GraphPad Prism was used for the statistical analysis.

According to ISO standards 5725-1 and 5725-2 for accuracy (trueness and precision) of measurement methods and results, the interlaboratory standard deviation of the assay results of all participating laboratories was calculated.

6.4 Results

6.4.1 Nanobiomaterials Characterization

The sterility in terms of endotoxins content of the FNPs and associated dispersant was assessed. Both were shown to have endotoxin levels that were below the standards set by the US FDA for medical devices (data not shown). Both HAADF-STEM pictures and TEM phase contrast images (**Figure 6.2A and B**) revealed regular morphology with a mean particle diameter of 12 nm.

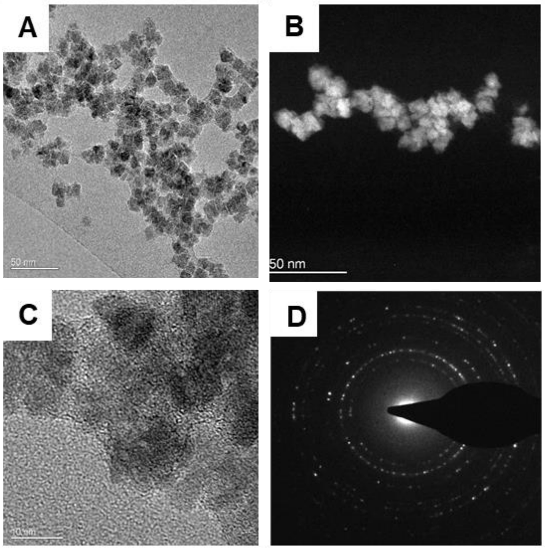

Figure 6.2. Representative TEM images of FNPs. A) *TEM phase contrast image;* ***B)*** *HAADF-STEM image;* ***C)*** *HREM phase contrast image;* ***D)*** *SAED polycrystalline pattern rings. Scale bars:* ***A,B)*** *50 nm;* ***C)*** *10 nm. Adapted from Martin et al., 2022* [352].

The polycrystalline pattern rings acquired by SAED (**Figure 6.2D**) were indexed as crystalline magnetite, which was identified as the unique phase composition. The higher magnification HREM phase contrast images (**Figure 6.2C**) revealed a cubic crystal structure compatible with the magnetite lattice. The benchmark materials were completely characterized [353,354].

After incubation at 37°C for 18 days in culture media, SAXS analysis revealed that there was little to no dissolution of the NM300K. These nanomaterials average sizes (15 0.2 nm and 15 0.2 nm at t = 0 and t = 18 days, respectively) did not change during incubation. In the relevant cell culture media, the hydrodynamic diameter and zeta potential of the NBMs were also examined.

After being incubated in cell culture media for 24 h under the exposure conditions required for the NRF2 reporter gene experiment, the data collectively showed that all the test materials were stable (**Figure 6.3A, B**).

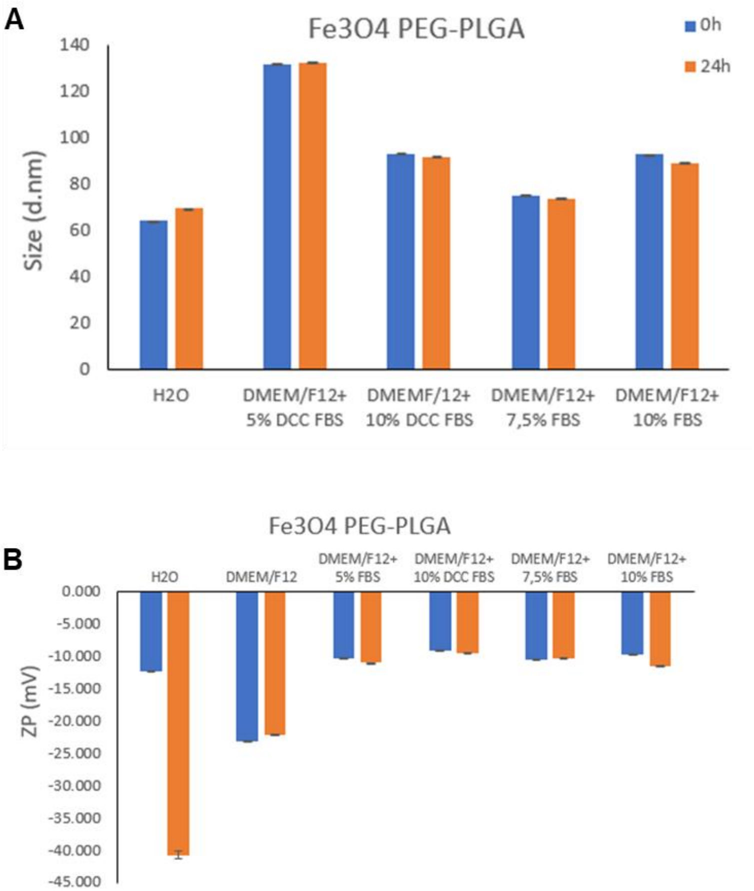

Figure 6.3. Characterization of Fe3O4-PEG-PLGA. A) *Hydrodynamic diameter and* ***B)*** *ζ-potential of FNPs in cell culture media or water. Adapted from Martin et al., 2022* [352].

6.4.2 Cytotoxicity evaluation

It is important to consider whether the test materials have the potential to affect cell viability before considering the outcomes of the reporter gene experiment. Only a modest reduction in U2OS cell viability was seen at the maximum tested dose of 100 µg/ml for FNPs (**Figure 6.4A**).

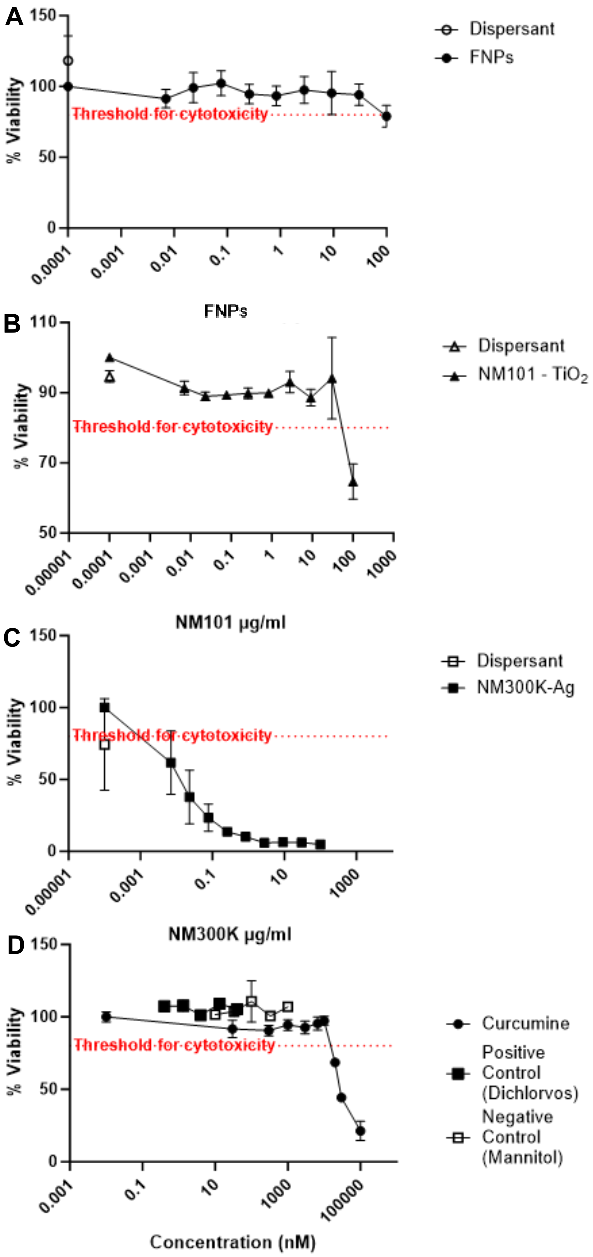

***Figure 6.4. Cytotoxicity evaluation** after 24 h of U2OS cells exposure to **A)** FNPs, **B)** TiO_2 nanomaterials (NM101), **C)** Ag nanomaterials (NM300K), and **D)** control chemicals or dispersants. Data are mean values ± S.D. n = 3. Edited from Martin et al., 2022* [352].

Similarly, NM101 was non-cytotoxic at low concentrations, but at the highest concentration (100 µg/ml) a significantly reduced viability was observed (**Figure 6.4B**). In contrast, a dose-dependent reduction of cell viability was found for NM300K (**Figure 6.4C**). The reference compounds were also evaluated for their potential cytotoxic effects (**Figure 6.4D**). The U2OS cells were unaffected by dichlorvos or mannitol, while curcumin, at concentrations of 500 nM and higher, significantly decreased U2OS cell viability in a dose-dependent manner (**Figure 6.4D**).

6.4.3 NRF2 reporter gene assay

The NRF2 pathway induction was then evaluated. Increasing amounts of the reference substance (curcumin), as well as the positive and negative controls, were administered to NRF2-U2OS cells (**Figure 6.5**). While exposure to mannitol did not induce NRF2 mediated gene expression, the reference substance, and the positive control (dichlorvos) did (**Figure 6.5**).

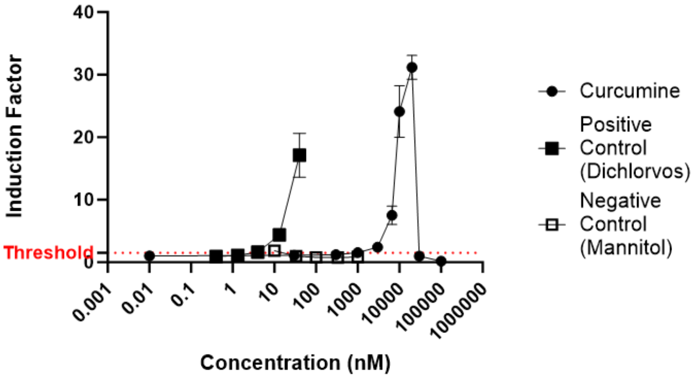

Figure 6.5. Induction of NRF2 mediated gene expression *by the reference compound (curcumin) and negative (mannitol) and positive controls (dichlorvos). The results are presented as induction factor, the fold induction over the solvent control. The data are presented as mean values ± S.D. n = 3. Edited from Martin et al., 2022* [352].

In the "round robin" pre-validation research, eight laboratories took part, seven of which (among which the UNITO team) employed FNPs, NM300K, and NM101 NMs (**Figure 6.6**), while one partner used solely FNPs (**Figure 6.7**).

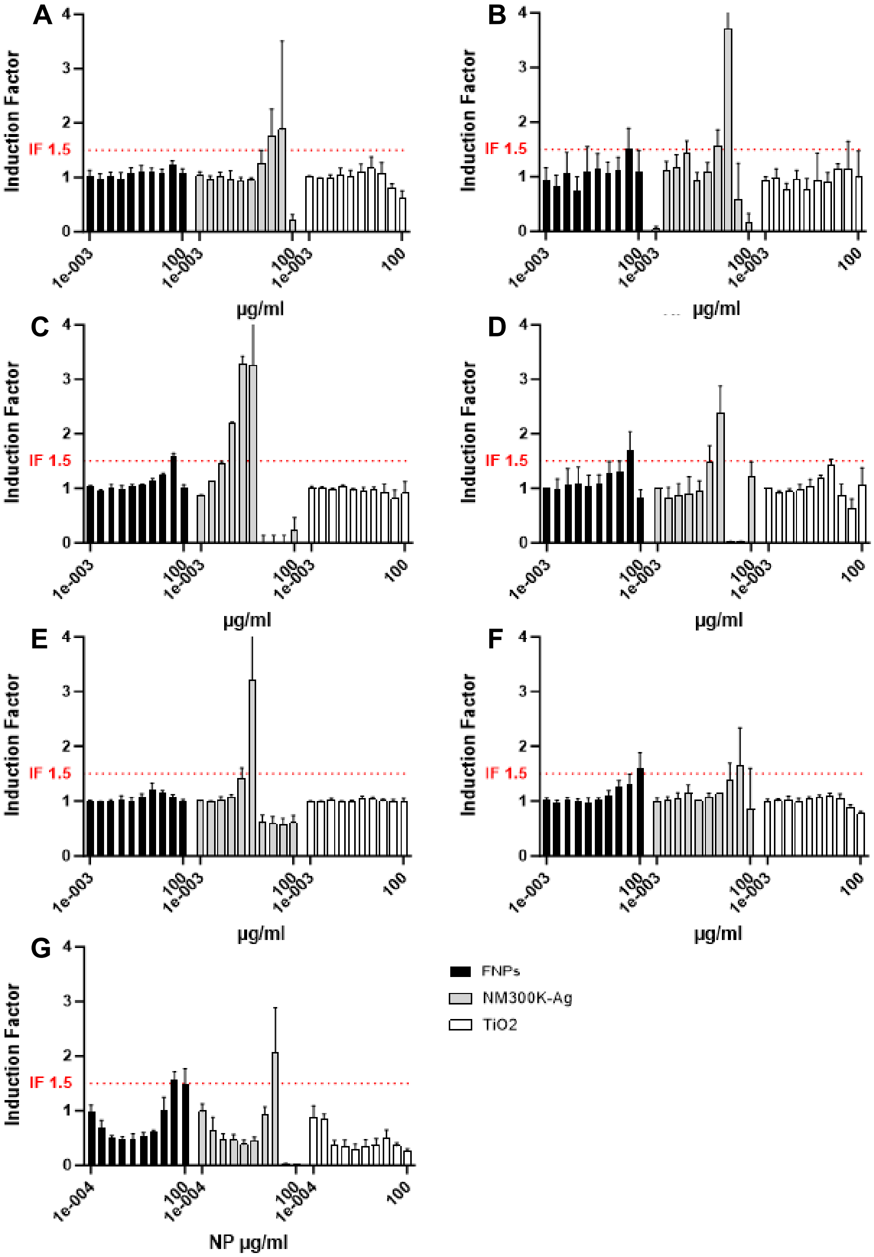

__Figure 6.6. Interlaboratory study__. Induction of NRF2 mediated gene expression following cells exposure to FNPs, NM300K, and NM101 nanomaterials. Each graph (__A–G__) represents the results of an individual laboratory. Each experiment was performed according to the same harmonized protocol. The results are presented as induction factor, the fold induction over the solvent control. The data are presented as mean values ± S.D, n = 3. Edited from Martin et al., 2022 [352].

Consistently, the findings demonstrated that NM101 did not promote NRF2-mediated gene expression. Yet, in every experiment, exposure to NM300K increased the expression of NRF2-mediated genes in a dose-dependent manner (**Figures 6.6A–G**). Induction factors, which measure the size of responses at similar concentrations, varied somewhat between laboratories. It was repeatedly discovered that the NRF2 mediated gene expression decreased at the highest concentrations, which is probably because of NM300K dose-dependent cytotoxicity as previously described in **section 6.2.2** (**Figure 6.4C**). Ultimately, little elevation of NRF2-mediated gene expression was seen after exposure to FNPs (**Figures 6.6A–G**).

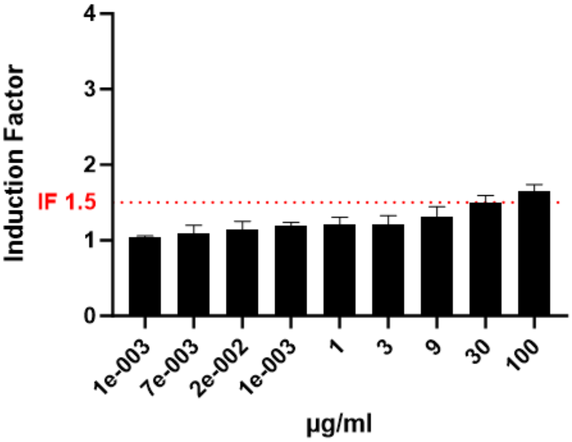

Figure 6.7. NRF2-mediated gene expression *in response to FNPs.*
The data are from participating laboratory 8. Data on NM101 and NM300K are not available. Edited from Martin et al., 2022 [352].

As a result, while three of the participating laboratories reported no induction, data from five more laboratories showed a slight induction at 30 or 100 µg/ml, and some laboratories reported a lower induction factor for the 100 µg/ml samples compared to the 30 µg/ml samples. The assay results inter- and intra-laboratory standard deviations were then determined. The mean inter-laboratory standard deviation was 0.28, with a range of 0.044 to 1.221. (**Figure**

6.8). The average intra-laboratory standard deviation was 0.16. (**Figures 6.9** and **6.10**).

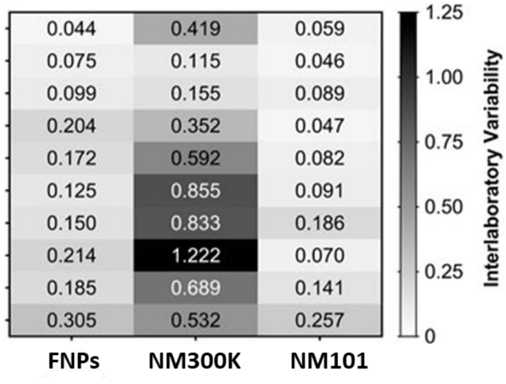

FNPs	NM300K	NM101
0.044	0.419	0.059
0.075	0.115	0.046
0.099	0.155	0.089
0.204	0.352	0.047
0.172	0.592	0.082
0.125	0.855	0.091
0.150	0.833	0.186
0.214	1.222	0.070
0.185	0.689	0.141
0.305	0.532	0.257

Figure 6.8. Heatmap of the interlaboratory standard deviation of the NRF2 induction results from all participating laboratories. *The combinations of concentration and nanomaterials that resulted in higher variability of assay results across the partner laboratories are indicated by darker boxes in the heatmap. Adapted from Martin et al., 2022* [352].

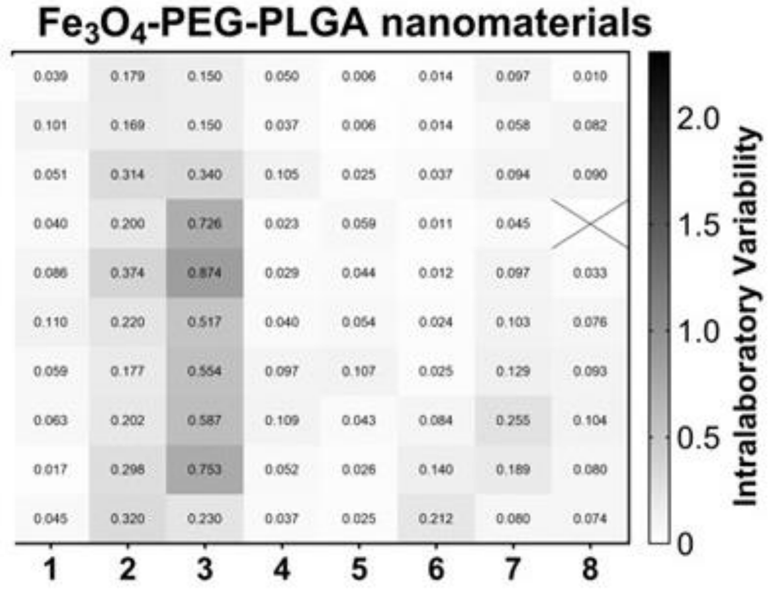

1	2	3	4	5	6	7	8
0.039	0.179	0.150	0.050	0.006	0.014	0.097	0.010
0.101	0.169	0.150	0.037	0.006	0.014	0.058	0.082
0.051	0.314	0.340	0.105	0.025	0.037	0.094	0.090
0.040	0.200	0.726	0.023	0.059	0.011	0.045	
0.086	0.374	0.874	0.029	0.044	0.012	0.097	0.033
0.110	0.220	0.517	0.040	0.054	0.024	0.103	0.076
0.059	0.177	0.554	0.097	0.107	0.025	0.129	0.093
0.063	0.202	0.587	0.109	0.043	0.084	0.255	0.104
0.017	0.298	0.753	0.052	0.026	0.140	0.189	0.080
0.045	0.320	0.230	0.037	0.025	0.212	0.080	0.074

Figure 6.9. Heatmaps of the intra-laboratory standard deviations of all NRF2 induction results performed with the U2OS cell line*. The combinations of concentration and nanomaterials that resulted in higher variability of assay results are indicated by darker boxes in the greyscale heatmap. The numbers represent the individual participating laboratories 1 – 8. Adapted from Martin et al., 2022* [352].

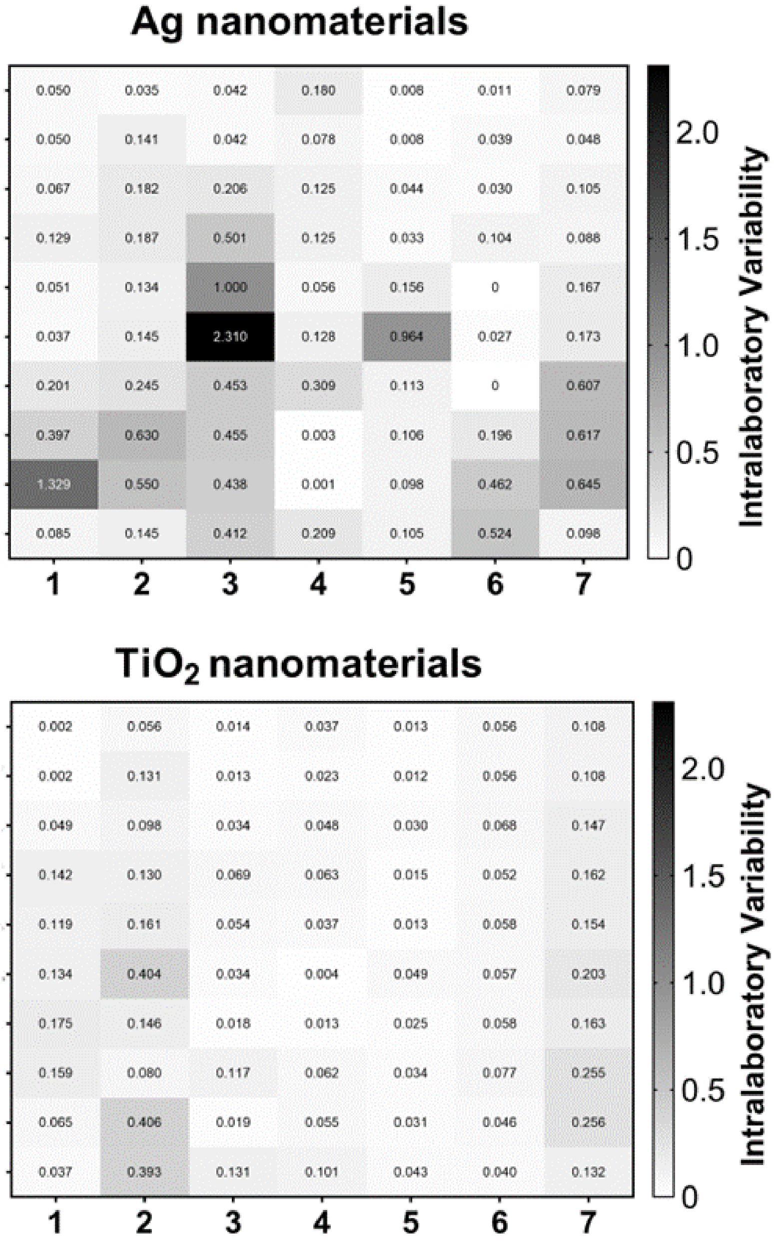

Ag nanomaterials

1	2	3	4	5	6	7
0.050	0.035	0.042	0.180	0.008	0.011	0.079
0.050	0.141	0.042	0.078	0.008	0.039	0.048
0.067	0.182	0.206	0.125	0.044	0.030	0.105
0.129	0.187	0.501	0.125	0.033	0.104	0.088
0.051	0.134	1.000	0.056	0.156	0	0.167
0.037	0.145	2.310	0.128	0.964	0.027	0.173
0.201	0.245	0.453	0.309	0.113	0	0.607
0.397	0.630	0.455	0.003	0.106	0.196	0.617
1.329	0.550	0.438	0.001	0.098	0.462	0.645
0.085	0.145	0.412	0.209	0.105	0.524	0.098

TiO_2 nanomaterials

1	2	3	4	5	6	7
0.002	0.056	0.014	0.037	0.013	0.056	0.108
0.002	0.131	0.013	0.023	0.012	0.056	0.108
0.049	0.098	0.034	0.048	0.030	0.068	0.147
0.142	0.130	0.069	0.063	0.015	0.052	0.162
0.119	0.161	0.054	0.037	0.013	0.058	0.154
0.134	0.404	0.034	0.004	0.049	0.057	0.203
0.175	0.146	0.018	0.013	0.025	0.058	0.163
0.159	0.080	0.117	0.062	0.034	0.077	0.255
0.065	0.406	0.019	0.055	0.031	0.046	0.256
0.037	0.393	0.131	0.101	0.043	0.040	0.132

Figure 6.10. Heatmaps of the intra-laboratory standard deviations of all NRF2 induction results performed with the U2OS cell line*. The combinations of concentration and nanomaterials that resulted in higher variability of assay results are indicated by darker boxes in the greyscale heatmap. The numbers represent the individual participating laboratories 1 – 7. Adapted from Martin et al., 2022* [352].

6.5 Discussion

In this chapter, we aimed to validate a NRF2 reporter gene assay to investigate for oxidative stress by screening for NRF2 mediated gene expression activation after exposure to NBMs. Eight laboratories participated in the pre-validation, including the UNITO team. As representative NMs, FNPs were chosen, and the outcomes were compared to "benchmark" nanomaterials from the JRC, NM101 (TiO_2) and NM300K (Ag), as well as positive and negative chemical controls. None of the collaborating labs saw an induction above the threshold for the NM101. Some laboratories measured an induction for the FNPs that was just above the threshold, however for other laboratories the induction levels were lower than the threshold. The NRF2 reporter gene assay can be easily used by several laboratories, as evidenced by the fact that all of them were able to detect a dose-dependent induction after exposure to the NM300K (albeit with varying induction factors). The NRF2 reporter gene test for assessing oxidative stress generated by NBMs is appropriate for application in different laboratories because the interlaboratory standard deviation was, overall, acceptable. Based on these preliminary results, we suggest considering this validated test for an in depth validation as a method for NBMs fast screening.

Manufactured NBMs have the ability to produce ROS through a variety of methods, including the Fenton reaction, redox cycling, and radical creation [355]. This ROS production can then activate the NRF2 mediated gene expression. Numerous previous investigations have demonstrated that nanoscale metal oxides, such as CuO and ZnO materials, can activate NRF2 [175,356]. Moreover, it was discovered that exposure to Ag nanoparticles activated NRF2, which is consistent with the present findings. According to the findings of the current investigation, FNPs only slightly activated U2OS-NRF2 cells. Unfortunately, no literature on the capacity of FNPs to induce NRF2-

mediated gene expression could be found. In a recent work, various acellular assays and a NRF2 reporter assay based on HEK293 cells were compared to examine the production of ROS and antioxidant responses of manmade NMs. It is noteworthy that whereas Fe_3O_4 nanoparticles have been found to be able to generate oxidative stress in rodents [357], the HEK293 cell-based NRF2 reporter experiment did not demonstrate any concentration-dependent reactivity for the Fe-based nanomaterials [177]. Due to the low number of expressed receptors in U2OS-NRF2 cells, there is extremely little chance of crosstalk between signal transduction pathways. Moreover, the U2OS cell line has a poor total metabolic capacity, which increases the likelihood and sensitivity of reactive substances, or metabolites, to activate reporter systems. The U2OS-NRF2 cells used in the current study have a tandem of four AREs upstream of the luciferase reporter and may therefore be more sensitive to inducers acting via the NRF2-pathway than the KeratinoSens^{TM} method validated by the OECD (Test No. 442D), which has one ARE-response element upfront of the ARE-reporter construct. However, caution must be used when comparing reporter assays in various cell systems and in vivo data because the presence of intracellular ROS levels can vary depending on the abundance of thiol-containing ligands (such as GSH and metallothioneins) [358], which may affect the sensitivity of cell-based NRF2 reporter gene assays.

In addition to the aforementioned *in vitro* research, a number of *in vivo* rodent investigations have also demonstrated that nanomaterials can cause NRF2 activation. For instance, Sun and co-workers [359] demonstrated that chronic exposure to TiO_2 nanoparticles increased the expression of the catalytic subunit of glutamate-cysteine ligase, NRF2, and heme oxygenase 1 (HO-1) (GCLC). In the aorta of mice, intra-tracheal injection of ZnO nanoparticles increased the expression of NRF2 and HO-1, according to other researchers [356]. In addition, members of the BIORIMA consortium previously used Nrf2-null mice to study the part NRF2 plays in pulmonary inflammation after exposure to ZnO nanoparticles [360]. The study showed infiltration of inflammatory cells in the mouse lung but only weakly stimulated NRF2-dependent antioxidant enzymes after administration of 20 nm ZnO nanoparticles by pharyngeal aspiration. The authors came to the conclusion that the neutrophil migration caused by ZnO nanoparticles is negatively regulated by NRF2 [360].

In recent years, a lot of research have been conducted to improve the quality of nanotoxicological investigations, including numerous interlaboratory comparisons (also known as round robins). For instance, a US consortium supported by the NIEHS carried out cell-based assays on a selection of NMs, concentrating on cell viability and cytokine (IL-1β) production. These assays included various kinds of TiO_2 and ZnO nanomaterials as well as multi-walled carbon nanotubes [361]. It was underlined how crucial it is to use carefully defined nanomaterials as well as positive and negative controls. The harmonization of *in vitro* test methods for the evaluation of NMs has also been a focus of several pan-European programs [52,362–364]. These efforts have highlighted the critical value of standardized test protocols while recognizing that the road to regulatory-relevant results can be challenging and long [365]. The need for adapting the current OECD Test Guidelines (TGs) and Guidance Documents (GDs) as well as generating new TGs and GDs to address NMs has been examined by the OECD Working Party on Manufactured Nanomaterials (WPMN) [366]. 18 European nations, numerous Directorates-General of the European Commission, the European Chemicals Agency (ECHA), and other organizations work together as part of the so-called Malta Initiative to make legislation, particularly for chemicals, enforceable [367]. The current goal of this European initiative is to make the OECD TGs on NMs fit for purpose by updating them. Although more validation is undoubtedly needed, the current reporter gene assay, which measures an essential biological endpoint called oxidative stress, is well matched with these efforts.

6.6 Conclusions

Comparing FNPs with NM101 and NM300K NMs, in this study a validation "round robin" employing the NRF2 reporter gene assay was successfully carried out. The assay was quickly adopted by different laboratories. It is important to remember that other reporter gene assays have already undergone validation and that the OECD TG 455 and TG 458 have just recently added the androgen receptor (AR)-reporter gene assay and the estrogen receptor (ER) reporter gene assay, respectively. In order to develop the NRF2 gene reporter assay for the screening of the induction of oxidative stress responses triggered by NBMs, the results of the current interlaboratory investigation may serve as a starting point for a large validation study.

These results have been published in Frontiers in Toxicology in the paper " Pre-validation of a reporter gene assay for oxidative stress for the rapid screening of nanobiomaterials ". [352]

7 General conclusions and perspectives

There is still a long road toward a validated *in vitro* model sufficiently representative of the OGI tract to predict the effects of NMs and MMs on the gut.

In the present study, we contribute to this field by exploring some possible improvements, starting by the widely used model Caco-2 cells.

Overall, the results show that the different *in vitro* models showed variable outcomes, supporting the need of standardization.

The employment of an *in vitro* digestion system, which modifies the physico-chemical features of the particles, has, depending upon the material, variable effects. The comparison with the effects in mice suggests that this pre-treatment have the potential to make the *in vitro* tests more predictive of the *in vivo* conditions. The differences between the two models could be attributed to the lack of some physiological features in Caco-2 barrier model, such as the presence of mucus, cells with an absorptive phenotype and inflammatory cells mimicking the mucosa-associated lymphoid tissue. For this reason, we moved in this direction by increasing the complexity of the model, exploring the possibility to add other types of cells such as goblet cells and M-cells, and by introducing a dynamic system by using a millifluidic system.

In perspective, the possibility to add other types of cells such as macrophages, dendritic cells, endothelial cells, and the microbiota components represents a further step to be closer to OGI physiology. Moreover, adding the variable of digested food that could affect the particles surface modification can add further information.

A future step made possible by millifluidic devices is the possibility to add other organ models (e.g., liver) to the OGI tract.

The validation of a cell-based assay to assess the particles potential to induce oxidative stress through an inter- laboratory test involving different European institutions and a non-European university was a key step in improving the reproducibility of *in vitro* tests, toward the set-up of standardized protocols.

Overall, this study contributes to the development of advanced and representative models reproducing the physiological features of the small intestine to assess the effects of micro- and nano-materials on this important and complex organ addressing the need to reduce the number of animals in the experimental research.

8 References

1. Ochekpe NA, Olorunfemi PO, Ngwuluka NC. Nanotechnology and drug delivery part 2: Nanostructures for drug delivery. Tropical Journal of Pharmaceutical Research. 2009;8:275–87.

2. Panel E, Chain F. Presence of microplastics and nanoplastics in food, with particular focus on seafood. EFSA Journal. 2016;14.

3. Galgani F, Hanke G, Werner S, De Vrees L. Marine litter within the European Marine Strategy Framework Directive. ICES Journal of Marine Science. 2013;70:1055–64.

4. Frias JPGL, Nash R. Microplastics: Finding a consensus on the definition. Mar Pollut Bull. 2019;138:145–7.

5. Solbes E, Harper RW. Biological responses to asbestos inhalation and pathogenesis of asbestos-related benign and malignant disease. J Investig Med. 2018;66:721–7.

6. Pira E, Donato F, Maida L, Discalzi G. Exposure to asbestos: past, present and future. J Thorac Dis. 2018;10:S237–45.

7. Noonan CW. Environmental asbestos exposure and risk of mesothelioma. Ann Transl Med. 2017;5:234.

8. Wagner GR. Asbestosis and silicosis. Lancet. 1997;349:1311–5.

9. Chemical agents and related occupations. IARC Monogr Eval Carcinog Risks Hum. 2012;100:9–562.

10. Hammad YY, Dharmarajan V, Weill H. Sampling of cotton dust for epidemiologic investigations. Chest. 1981;79:108S-113S.

11. Glindmeyer HW, Rando RJ, Lefante JJ, Freyder L, Brisolara JA, Jones RN. Longitudinal respiratory health study of the wood processing industry. Am J Ind Med. 2008;51:595–609.

12. Olenchock SA, May JJ, Pratt DS, Piacitelli LA, Parker JE. Presence of endotoxins in different agricultural environments. Am J Ind Med. 1990;18:279–84.

13. Séguin V, Lemauviel-Lavenant S, Garon D, Bouchart V, Gallard Y, Blanchet B, et al. Effect of agricultural and environmental factors on the hay

characteristics involved in equine respiratory disease. Agric Ecosyst Environ. 2010;135:206–15.

14. Alpert N, van Gerwen M, Taioli E. Epidemiology of mesothelioma in the 21(st) century in Europe and the United States, 40 years after restricted/banned asbestos use. Transl Lung Cancer Res. 2020;9:S28–38.

15. Leung CC, Yu ITS, Chen W. Silicosis. Lancet. 2012;379:2008–18.

16. Benmoussa N, Rebibo JD, Conan P, Charlier P. Chimney-sweeps' cancer—early proof of environmentally driven tumourigenicity. Lancet Oncol. 2019;20:338.

17. Binazzi A, Ferrante P, Marinaccio A. Occupational exposure and sinonasal cancer: a systematic review and meta-analysis. BMC Cancer. 2015;15:49.

18. Dangi BM, Bhise AR. Cotton dust exposure: Analysis of pulmonary function and respiratory symptoms. Lung India. 2017;34:144–9.

19. Reboux G, Piarroux R, Roussel S, Millon L, Bardonnet K, Dalphin J-C. Assessment of four serological techniques in the immunological diagnosis of farmers' lung disease. J Med Microbiol. 2007;56:1317–21.

20. Zhang P, Chen L, Gu W, Xu Z, Gao Y, Li Y. In vitro and in vivo evaluation of donepezil-sustained release microparticles for the treatment of Alzheimer's disease. Biomaterials. 2007;28:1882–8.

21. Amore E, Manca ML, Ferraro M, Valenti D, La Parola V, Di Vincenzo S, et al. Salmeterol Xinafoate (SX) loaded into mucoadhesive solid lipid microparticles for COPD treatment. Int J Pharm. 2019;562:351–8.

22. Thiyagarajan D, Huck B, Nothdurft B, Koch M, Rudolph D, Rutschmann M, et al. Spray-dried lactose-leucine microparticles for pulmonary delivery of antimycobacterial nanopharmaceuticals. Drug Deliv Transl Res. 2021;11:1766–78.

23. Matsuo T, Masumoto H, Tajima S, Ikuno T, Katayama S, Minakata K, et al. Efficient long-term survival of cell grafts after myocardial infarction with thick viable cardiac tissue entirely from pluripotent stem cells. Sci Rep. 2015;5:16842.

24. Li Z, Masumoto H, Jo J-I, Yamazaki K, Ikeda T, Tabata Y, et al. Sustained release of basic fibroblast growth factor using gelatin hydrogel improved left ventricular function through the alteration of collagen subtype in a rat

chronic myocardial infarction model. Gen Thorac Cardiovasc Surg. 2018;66:641–7.

25. Kakudo N, Morimoto N, Ogawa T, Hihara M, Notodihardjo PV, Matsui M, et al. Angiogenic effect of platelet-rich plasma combined with gelatin hydrogel granules injected into murine subcutis. J Tissue Eng Regen Med. 2017;11:1941–8.

26. Shibata M, Takagi G, Kudo M, Kurita J, Kawamoto Y, Miyagi Y, et al. Enhanced Sternal Healing Through Platelet-Rich Plasma and Biodegradable Gelatin Hydrogel. Tissue Eng Part A. 2018;24:1406–12.

27. Annamalai RT, Turner PA, Carson WF, Levi B, Kunkel S, Stegemann JP. Harnessing macrophage-mediated degradation of gelatin microspheres for spatiotemporal control of BMP2 release. Biomaterials. 2018;161:216–27.

28. Xia P, Wang S, Qi Z, Zhang W, Sun Y. BMP-2-releasing gelatin microspheres/PLGA scaffolds for bone repairment of X-ray-radiated rabbit radius defects. Artif Cells Nanomed Biotechnol. 2019;47:1662–73.

29. Kudva AK, Dikina AD, Luyten FP, Alsberg E, Patterson J. Gelatin microspheres releasing transforming growth factor drive in vitro chondrogenesis of human periosteum derived cells in micromass culture. Acta Biomater. 2019;90:287–99.

30. Bello AB, Kim Y, Park S, Muttigi MS, Kim J, Park H, et al. Matrilin3/TGFβ3 gelatin microparticles promote chondrogenesis, prevent hypertrophy, and induce paracrine release in MSC spheroid for disc regeneration. NPJ Regen Med. 2021;6:50.

31. Mitsui R, Matsukawa M, Nakagawa K, Isomura E, Kuwahara T, Nii T, et al. Efficient cell transplantation combining injectable hydrogels with control release of growth factors. Regen Ther. 2021;18:372–83.

32. Wang D, Yao Y, He J, Zhong X, Li B, Rao S, et al. Engineered Cell-Derived Microparticles Bi(2)Se(3)/DOX@MPs for Imaging Guided Synergistic Photothermal/Low-Dose Chemotherapy of Cancer. Adv Sci (Weinh). 2020;7:1901293.

33. Andrady AL. Microplastics in the marine environment. Mar Pollut Bull. 2011;62:1596–605.

34. Wright SL, Thompson RC, Galloway TS. The physical impacts of microplastics on marine organisms: A review. Environmental Pollution. 2013;178:483–92.

35. Commission E, Innovation D-G for R and. Microplastic pollution – The policy context – Background paper. Publications Office; 2018.

36. Hesler M, Aengenheister L, Ellinger B, Drexel R, Straskraba S, Jost C, et al. Multi-endpoint toxicological assessment of polystyrene nano- and microparticles in different biological models in vitro. Toxicol In Vitro. 2019;61:104610.

37. Stock V, Böhmert L, Lisicki E, Block R, Cara-Carmona J, Pack LK, et al. Uptake and effects of orally ingested polystyrene microplastic particles in vitro and in vivo. Arch Toxicol. 2019;93:1817–33.

38. Rudolph J, Völkl M, Jérôme V, Scheibel T, Freitag R. Noxic effects of polystyrene microparticles on murine macrophages and epithelial cells. Sci Rep. 2021;11:15702.

39. Hollerova A, Hodkovicova N, Blahova J, Faldyna M, Franc A, Pavlokova S, et al. Polystyrene microparticles can affect the health status of freshwater fish - Threat of oral microplastics intake. Sci Total Environ. 2023;858:159976.

40. Ahmadifar E, Kalhor N, Dawood MAO, Ahmadifar M, Moghadam MS, Abarghouei S, et al. Effects of polystyrene microparticles on inflammation, antioxidant enzyme activities, and related gene expression in Nile tilapia (Oreochromis niloticus). Environ Sci Pollut Res Int. 2021;28:14909–16.

41. Jasinski J, Wilde M V, Voelkl M, Jérôme V, Fröhlich T, Freitag R, et al. Tailor-Made Protein Corona Formation on Polystyrene Microparticles and its Effect on Epithelial Cell Uptake. ACS Appl Mater Interfaces. 2022;14:47277–87.

42. Żeliszewska P, Wasilewska M, Adamczyk Z. Monolayers of immunoglobulin G on polystyrene microparticles and their interactions with human serum albumin. J Colloid Interface Sci. 2017;490:587–97.

43. Foulon V, Le Roux F, Lambert C, Huvet A, Soudant P, Paul-Pont I. Colonization of Polystyrene Microparticles by Vibrio crassostreae: Light and Electron Microscopic Investigation. Environ Sci Technol. 2016;50:10988–96.

44. Ziani K, Ioniță-Mîndrican C-B, Mititelu M, Neacșu SM, Negrei C, Moroșan E, et al. Microplastics: A Real Global Threat for Environment and Food Safety: A State of the Art Review. Nutrients. 2023;15.

45. Recommendation C. Πολιτική - European Commission. 2022;36237:1–5.

46. Lähde A, Sæunn Gudmundsdottir S, Joutsensaari J, Tapper U, Ruusunen J, Ihalainen M, et al. In vitro evaluation of pulmonary deposition of airborne volcanic ash. Atmos Environ. 2013;70:18–27.

47. Blanco-Andujar C, Ortega D, Pankhurst QA, Thanh NTK. Elucidating the morphological and structural evolution of iron oxide nanoparticles formed by sodium carbonate in aqueous medium. J Mater Chem. 2012;22:12498–506.

48. Wu C-Y, Martel J, Wong T-Y, Young D, Liu C-C, Lin C-W, et al. Formation and characteristics of biomimetic mineralo-organic particles in natural surface water. Sci Rep. 2016;6:28817.

49. Janssen A, De Keizer A, Van Aelst A, Fokkink R, Yangling H, Lettinga G. Surface characteristics and aggregation of microbiologically produced sulphur particles in relation to the process conditions. Colloids Surf B Biointerfaces. 1996;6:115–29.

50. Mishra S, Singh BR, Naqvi AH, Singh HB. Potential of biosynthesized silver nanoparticles using Stenotrophomonas sp. BHU-S7 (MTCC 5978) for management of soil-borne and foliar phytopathogens. Sci Rep. 2017;7:45154.

51. Murr LE, Guerrero PA. Carbon nanotubes in wood soot. Atmospheric Science Letters. 2006;7:93–5.

52. Farcal L, Torres Andón F, Di Cristo L, Rotoli BM, Bussolati O, Bergamaschi E, et al. Comprehensive In Vitro Toxicity Testing of a Panel of Representative Oxide Nanomaterials: First Steps towards an Intelligent Testing Strategy. PLoS One. 2015;10:e0127174.

53. Chen X, Mao SS. Titanium dioxide nanomaterials: synthesis, properties, modifications, and applications. Chem Rev. 2007;107:2891–959.

54. Larue C, Castillo-Michel H, Sobanska S, Trcera N, Sorieul S, Cécillon L, et al. Fate of pristine TiO2 nanoparticles and aged paint-containing TiO2 nanoparticles in lettuce crop after foliar exposure. J Hazard Mater. 2014;273:17–26.

55. Wittig A, Gehrke H, Del Favero G, Fritz E-M, Al-Rawi M, Diabaté S, et al. Amorphous Silica Particles Relevant in Food Industry Influence Cellular Growth and Associated Signaling Pathways in Human Gastric Carcinoma Cells. Nanomaterials (Basel). 2017;7.

56. Quiterio-Gutiérrez T, Ortega-Ortiz H, Cadenas-Pliego G, Hernández-Fuentes AD, Sandoval-Rangel A, Benavides-Mendoza A, et al. The Application of Selenium and Copper Nanoparticles Modifies the Biochemical Responses of Tomato Plants under Stress by Alternaria solani. Int J Mol Sci. 2019;20.

57. Khoobchandani M, Katti KK, Karikachery AR, Thipe VC, Srisrimal D, Dhurvas Mohandoss DK, et al. New Approaches in Breast Cancer Therapy Through Green Nanotechnology and Nano-Ayurvedic Medicine - Pre-Clinical and Pilot Human Clinical Investigations. Int J Nanomedicine. 2020;15:181–97.

58. Lee YY, Park HH, Park W, Kim H, Jang JG, Hong KS, et al. Long-acting nanoparticulate DNase-1 for effective suppression of SARS-CoV-2-mediated neutrophil activities and cytokine storm. Biomaterials. 2021;267:120389.

59. Golestannejad Z, Khozeimeh F, Mehrasa M, Mirzaeei S, Sarfaraz D. A novel drug delivery system using acyclovir nanofiber patch for topical treatment of recurrent herpes labialis: A randomized clinical trial. Clin Exp Dent Res. 2022;8:184–90.

60. Bahadur S, Sachan N, Harwansh RK, Deshmukh R. Nanoparticlized System: Promising Approach for the Management of Alzheimer’s Disease through Intranasal Delivery. Curr Pharm Des. 2020;26:1331–44.

61. Nayeem MOG, Lee S, Jin H, Matsuhisa N, Jinno H, Miyamoto A, et al. All-nanofiber-based, ultrasensitive, gas-permeable mechanoacoustic sensors for continuous long-term heart monitoring. Proc Natl Acad Sci U S A. 2020;117:7063–70.

62. Tan Y, Yan B, Xue L, Li Y, Luo X, Ji P. Surface-enhanced Raman spectroscopy of blood serum based on gold nanoparticles for the diagnosis of the oral squamous cell carcinoma. Lipids Health Dis. 2017;16:73.

63. Verry C, Dufort S, Villa J, Gavard M, Iriart C, Grand S, et al. Theranostic AGuIX nanoparticles as radiosensitizer: A phase I, dose-escalation study in patients with multiple brain metastases (NANO-RAD trial). Radiother Oncol. 2021;160:159–65.

64. Tomar R, Abdala AA, Chaudhary RG, Singh NB. Photocatalytic degradation of dyes by nanomaterials. Mater Today Proc. 2020;29:967–73.

65. Roduner E. Size matters: why nanomaterials are different. Chem Soc Rev. 2006;35:583–92.

66. Geoffrion LD, Guisbiers G. Quantum confinement: Size on the grill! Journal of Physics and Chemistry of Solids. 2020;140:109320.

67. Krishnan SK, Singh E, Singh P, Meyyappan M, Nalwa HS. A review on graphene-based nanocomposites for electrochemical and fluorescent biosensors. RSC Adv. 2019;9:8778–881.

68. Wu Q, Miao W, Zhang Y, Gao H, Hui D. No Title. Nanotechnol Rev. 2020;9:259–73.

69. Amin MT, Alazba AA, Manzoor U. A Review of Removal of Pollutants from Water/Wastewater Using Different Types of Nanomaterials. de Lima AGB, editor. Advances in Materials Science and Engineering. 2014;2014:825910.

70. Malakar A, Kanel SR, Ray C, Snow DD, Nadagouda MN. Nanomaterials in the environment, human exposure pathway, and health effects: A review. Science of The Total Environment. 2021;759:143470.

71. Buzea C, Pacheco I. Nanomaterial and Nanoparticle: Origin and Activity BT - Nanoscience and Plant–Soil Systems. In: Ghorbanpour M, Manika K, Varma A, editors. Cham: Springer International Publishing; 2017. p. 71–112.

72. Dris R, Gasperi J, Saad M, Mirande C, Tassin B. Synthetic fibers in atmospheric fallout: A source of microplastics in the environment? Mar Pollut Bull. 2016;104:290–3.

73. Dris R, Gasperi J, Rocher V, Saad M, Renault N, Tassin B. Microplastic contamination in an urban area: a case study in Greater Paris. Environmental Chemistry. 2015;12:592–9.

74. Oberbek P, Kozikowski P, Czarnecka K, Sobiech P, Jakubiak S, Jankowski T. Inhalation exposure to various nanoparticles in work environment—contextual information and results of measurements. Journal of Nanoparticle Research. 2019;21:222.

75. Cox KD, Covernton GA, Davies HL, Dower JF, Juanes F, Dudas SE. Human Consumption of Microplastics. Environ Sci Technol. 2019;53:7068–74.

76. Geiser M, Jeannet N, Fierz M, Burtscher H. Evaluating Adverse Effects of Inhaled Nanoparticles by Realistic In Vitro Technology. Nanomaterials. 2017;7.

77. Brown LM, Collings N, Harrison RM, Maynard AD, Maynard RL, Donaldson K, et al. Ultrafine particles: mechanisms of lung injury. Philosophical Transactions of the Royal Society of London Series A: Mathematical, Physical and Engineering Sciences. 2000;358:2741–9.

78. Monteiro-Riviere NA, Tran CL. Pulmonary and Cardiovascular Effects of Nanoparticles. Nanotoxicology. United Kingdom: CRC Press; 2007. p. 283–314.

79. Clift MJD, Gehr P, Rothen-Rutishauser B. Nanotoxicology: a perspective and discussion of whether or not in vitro testing is a valid alternative. Arch Toxicol. 2011;85:723–31.

80. Foldbjerg R, Dang DA, Autrup H. Cytotoxicity and genotoxicity of silver nanoparticles in the human lung cancer cell line, A549. Arch Toxicol. 2011;85:743–50.

81. Magdolenova Z, Collins A, Kumar A, Dhawan A, Stone V, Dusinska M. Mechanisms of genotoxicity. A review of in vitro and in vivo studies with engineered nanoparticles. Nanotoxicology. 2014;8:233–78.

82. Donaldson K, Tran L, Jimenez LA, Duffin R, Newby DE, Mills N, et al. Combustion-derived nanoparticles: a review of their toxicology following inhalation exposure. Part Fibre Toxicol. 2005;2:10.

83. Donaldson K, Duffin R, Langrish JP, Miller MR, Mills NL, Poland CA, et al. Nanoparticles and the cardiovascular system: a critical review. Nanomedicine (Lond). 2013;8:403–23.

84. BéruBé K, Balharry D, Sexton K, Koshy L, Jones T. Combustion-derived nanoparticles: mechanisms of pulmonary toxicity. Clin Exp Pharmacol Physiol. 2007;34:1044–50.

85. Prata JC. Airborne microplastics: Consequences to human health? Environ Pollut. 2018;234:115–26.

86. Turcotte SE, Chee A, Walsh R, Grant FC, Liss GM, Boag A, et al. Flock worker's lung disease: natural history of cases and exposed workers in Kingston, Ontario. Chest. 2013;143:1642–8.

87. Yhee JY, Im J, Nho RS. Advanced Therapeutic Strategies for Chronic Lung Disease Using Nanoparticle-Based Drug Delivery. J Clin Med. 2016;5.

88. McClements DJ, Xiao H. Is nano safe in foods? Establishing the factors impacting the gastrointestinal fate and toxicity of organic and inorganic food-grade nanoparticles. NPJ Sci Food. 2017;1:6.

89. Koelmans AA, Mohamed Nor NH, Hermsen E, Kooi M, Mintenig SM, De France J. Microplastics in freshwaters and drinking water: Critical review and assessment of data quality. Water Res. 2019;155:410–22.

90. Elizalde-Velázquez GA, Gómez-Oliván LM. Microplastics in aquatic environments: A review on occurrence, distribution, toxic effects, and implications for human health. Sci Total Environ. 2021;780:146551.

91. Shruti VC, Pérez-Guevara F, Elizalde-Martínez I, Kutralam-Muniasamy G. Toward a unified framework for investigating micro(nano)plastics in packaged beverages intended for human consumption. Environ Pollut. 2021;268:115811.

92. Ammar HO, Ghorab M, Kamel R, Salama AH. A trial for the design and optimization of pH-sensitive microparticles for intestinal delivery of cinnarizine. Drug Deliv Transl Res. 2016;6:195–209.

93. Cherniakov I, Izgelov D, Barasch D, Davidson E, Domb AJ, Hoffman A. Piperine-pro-nanolipospheres as a novel oral delivery system of cannabinoids: Pharmacokinetic evaluation in healthy volunteers in comparison to buccal spray administration. J Control Release. 2017;266:1–7.

94. Marucco A, Prono M, Beal D, Alasonati E, Fisicaro P, Bergamaschi E, et al. Biotransformation of Food-Grade and Nanometric TiO(2) in the Oral-Gastro-Intestinal Tract: Driving Forces and Effect on the Toxicity toward Intestinal Epithelial Cells. Nanomaterials (Basel). 2020;10.

95. Li B, Ding Y, Cheng X, Sheng D, Xu Z, Rong Q, et al. Polyethylene microplastics affect the distribution of gut microbiota and inflammation development in mice. Chemosphere. 2020;244:125492.

96. Ding G, Zhang N, Wang C, Li X, Zhang J, Li W, et al. Effect of the size on the aggregation and sedimentation of graphene oxide in seawaters with different salinities. Journal of Nanoparticle Research. 2018;20:313.

97. De Matteis V. Exposure to Inorganic Nanoparticles: Routes of Entry, Immune Response, Biodistribution and In Vitro/In Vivo Toxicity Evaluation. Toxics. 2017;5.

98. Cheung PK, Fok L. Evidence of microbeads from personal care product contaminating the sea. Mar Pollut Bull. 2016;109:582–5.

99. Borrero-Lopez O, Guiberteau F, Zhang Y, Lawn BR. Wear of ceramic-based dental materials. J Mech Behav Biomed Mater. 2019;92:144–51.

100. Larese Filon F, Mauro M, Adami G, Bovenzi M, Crosera M. Nanoparticles skin absorption: New aspects for a safety profile evaluation. Regulatory Toxicology and Pharmacology. 2015;72:310–22.

101. Rahman A, Sarkar A, Yadav OP, Achari G, Slobodnik J. Potential human health risks due to environmental exposure to nano- and microplastics and knowledge gaps: A scoping review. Sci Total Environ. 2021;757:143872.

102. Chen Y-Y, Lee Y-H, Wang B-J, Chen R-J, Wang Y-J. Skin damage induced by zinc oxide nanoparticles combined with UVB is mediated by activating cell pyroptosis via the NLRP3 inflammasome-autophagy-exosomal pathway. Part Fibre Toxicol. 2022;19:2.

103. Korin N, Kanapathipillai M, Ingber DE. Shear-Responsive Platelet Mimetics for Targeted Drug Delivery. Isr J Chem. 2013;53:610–5.

104. Yu YM, Bu FZ, Meng SS, Yan CW, Wu ZY, Li YT. The first nano-cocrystal formulation of marine drug cytarabine with uracil based on cocrystal nanonization strategy for long-acting injection exhibiting enhanced antitumor activity. Int J Pharm. 2023;644:123300.

105. Xia D, Zhang X, Hao H, Jiang W, Chen C, Li H, et al. Strategies to prolong drug retention in solid tumors by aggregating Endo-CMC nanoparticles. J Control Release. 2023;360:705–17.

106. Ilinskaya AN, Dobrovolskaia MA. Nanoparticles and the blood coagulation system. Part I: benefits of nanotechnology. Nanomedicine (Lond). 2013;8:773–84.

107. Ning H, Zhou Y, Zhou Z, Cheng S, Huang R, Ning H, et al. Challenges to improving occupational health in China. Occup Environ Med. 2017;74:924–5.

108. Sajid M, Ilyas M, Basheer C, Tariq M, Daud M, Baig N, et al. Impact of nanoparticles on human and environment: review of toxicity factors, exposures, control strategies, and future prospects. Environmental Science and Pollution Research. 2015;22:4122–43.

109. Favi PM, Gao M, Johana Sepúlveda Arango L, Ospina SP, Morales M, Pavon JJ, et al. Shape and surface effects on the cytotoxicity of nanoparticles:

Gold nanospheres versus gold nanostars. J Biomed Mater Res A. 2015;103:3449–62.

110. Steckiewicz KP, Barcinska E, Malankowska A, Zauszkiewicz–Pawlak A, Nowaczyk G, Zaleska-Medynska A, et al. Impact of gold nanoparticles shape on their cytotoxicity against human osteoblast and osteosarcoma in in vitro model. Evaluation of the safety of use and anti-cancer potential. J Mater Sci Mater Med. 2019;30:22.

111. Hermabessiere L, Dehaut A, Paul-Pont I, Lacroix C, Jezequel R, Soudant P, et al. Occurrence and effects of plastic additives on marine environments and organisms: A review. Chemosphere. 2017;182:781–93.

112. Casals-Casas C, Desvergne B. Endocrine disruptors: from endocrine to metabolic disruption. Annu Rev Physiol. 2011;73:135–62.

113. Braun JM, Sathyanarayana S, Hauser R. Phthalate exposure and children’s health. Curr Opin Pediatr. 2013;25:247–54.

114. Kirstein I V, Kirmizi S, Wichels A, Garin-Fernandez A, Erler R, Löder M, et al. Dangerous hitchhikers? Evidence for potentially pathogenic Vibrio spp. on microplastic particles. Mar Environ Res. 2016;120:1–8.

115. Yang Y, Liu W, Zhang Z, Grossart H-P, Gadd GM. Microplastics provide new microbial niches in aquatic environments. Appl Microbiol Biotechnol. 2020;104:6501–11.

116. Udovicki B, Andjelkovic M, Cirkovic-Velickovic T, Rajkovic A. Microplastics in food: scoping review on health effects, occurrence, and human exposure. Int J Food Contam. 2022;9:7.

117. Wolfram J, Yang Y, Shen J, Moten A, Chen C, Shen H, et al. The nano-plasma interface: Implications of the protein corona. Colloids Surf B Biointerfaces. 2014;124:17–24.

118. Marucco A, Gazzano E, Ghigo D, Enrico E, Fenoglio I. Fibrinogen enhances the inflammatory response of alveolar macrophages to TiO2, SiO2 and carbon nanomaterials. Nanotoxicology. 2016;10:1–9.

119. Park S, Ha MK, Lee Y, Song J, Yoon TH. Effects of Immune Cell Heterogeneity and Protein Corona on the Cellular Association and Cytotoxicity of Gold Nanoparticles: A Single-Cell-Based, High-Dimensional Mass Cytometry Study. ACS nanoscience Au. 2023;3:323–34.

120. Sharma V, Singh P, Pandey AK, Dhawan A. Induction of oxidative stress, DNA damage and apoptosis in mouse liver after sub-acute oral exposure to zinc oxide nanoparticles. Mutat Res. 2012;745:84–91.

121. Deng Y, Zhang Y, Lemos B, Ren H. Tissue accumulation of microplastics in mice and biomarker responses suggest widespread health risks of exposure. Sci Rep. 2017;7:46687.

122. Bressan E, Ferroni L, Gardin C, Rigo C, Stocchero M, Vindigni V, et al. Silver Nanoparticles and Mitochondrial Interaction. Jimbo R, editor. Int J Dent. 2013;2013:312747.

123. Huang C-C, Aronstam RS, Chen D-R, Huang Y-W. Oxidative stress, calcium homeostasis, and altered gene expression in human lung epithelial cells exposed to ZnO nanoparticles. Toxicol In Vitro. 2010;24:45–55.

124. Van Tienhoven EAE, Korbee D, Schipper L, Verharen HW, De Jong WH. In vitro and in vivo (cyto)toxicity assays using PVC and LDPE as model materials. J Biomed Mater Res A. 2006;78A:175–82.

125. Medina C, Santos-Martinez MJ, Radomski A, Corrigan OI, Radomski MW. Nanoparticles: pharmacological and toxicological significance. Br J Pharmacol. 2007;150:552–8.

126. Zhu X, Hondroulis E, Liu W, Li C-Z. Biosensing approaches for rapid genotoxicity and cytotoxicity assays upon nanomaterial exposure. Small. 2013;9:1821–30.

127. Mourya D, Dubey K, Jha S, Maurya R, Pandey AK. In Vitro Effects of Zirconia Nanoparticles: Uptake, Genotoxicity, and Mutagenicity in V-79 cells. Biol Trace Elem Res. 2023;

128. Shi X, Wang X, Huang R, Tang C, Hu C, Ning P, et al. Cytotoxicity and Genotoxicity of Polystyrene Micro- and Nanoplastics with Different Size and Surface Modification in A549 Cells. Int J Nanomedicine. 2022;17:4509–23.

129. Downs TR, Crosby ME, Hu T, Kumar S, Sullivan A, Sarlo K, et al. Silica nanoparticles administered at the maximum tolerated dose induce genotoxic effects through an inflammatory reaction while gold nanoparticles do not. Mutation Research/Genetic Toxicology and Environmental Mutagenesis. 2012;745:38–50.

130. Greenwood-Van Meerveld B, Johnson AC, Grundy D. Gastrointestinal Physiology and Function. Handb Exp Pharmacol. 2017;239:1–16.

131. Hoyle T. The digestive system: linking theory and practice. Br J Nurs. 1997;6:1285–91.

132. Groschwitz KR, Hogan SP. Intestinal barrier function: molecular regulation and disease pathogenesis. J Allergy Clin Immunol. 2009;124:2–3.

133. Bravo-Osuna I, Vauthier C, Farabollini A, Palmieri GF, Ponchel G. Mucoadhesion mechanism of chitosan and thiolated chitosan-poly(isobutyl cyanoacrylate) core-shell nanoparticles. Biomaterials. 2007;28:2233–43.

134. Anderson JM, Van Itallie CM. Physiology and function of the tight junction. Cold Spring Harb Perspect Biol. 2009;1:a002584.

135. Turner JR. Intestinal mucosal barrier function in health and disease. Nat Rev Immunol. 2009;9:799–809.

136. Dokladny K, Zuhl MN, Moseley PL. Intestinal epithelial barrier function and tight junction proteins with heat and exercise. J Appl Physiol (1985). 2016;120:692–701.

137. Liang B, Zhong Y, Huang Y, Lin X, Liu J, Lin L, et al. Underestimated health risks: polystyrene micro- and nanoplastics jointly induce intestinal barrier dysfunction by ROS-mediated epithelial cell apoptosis. Part Fibre Toxicol. 2021;18:20.

138. Cornu R, Chrétien C, Pellequer Y, Martin H, Béduneau A. Small silica nanoparticles transiently modulate the intestinal permeability by actin cytoskeleton disruption in both Caco-2 and Caco-2/HT29-MTX models. Arch Toxicol. 2020;94:1191–202.

139. Snyder RJ, Hussain S, Rice AB, Garantziotis S. Multiwalled carbon nanotubes induce altered morphology and loss of barrier function in human bronchial epithelium at noncytotoxic doses. Int J Nanomedicine. 2014;9:4093–105.

140. des Rieux A, Fievez V, Théate I, Mast J, Préat V, Schneider Y-J. An improved in vitro model of human intestinal follicle-associated epithelium to study nanoparticle transport by M cells. Eur J Pharm Sci. 2007;30:380–91.

141. Delon LC, Faria M, Jia Z, Johnston S, Gibson R, Prestidge CA, et al. Capturing and Quantifying Particle Transcytosis with Microphysiological Intestine-on-Chip Models. Small Methods. 2023;7:e2200989.

142. Oberdörster G, Maynard A, Donaldson K, Castranova V, Fitzpatrick J, Ausman K, et al. Principles for characterizing the potential human health effects from exposure to nanomaterials: elements of a screening strategy. Part Fibre Toxicol. 2005;2:8.

143. Abbott LC, Maynard AD. Exposure assessment approaches for engineered nanomaterials. Risk Anal. 2010;30:1634–44.

144. Sohal IS, Cho YK, O'Fallon KS, Gaines P, Demokritou P, Bello D. Dissolution Behavior and Biodurability of Ingested Engineered Nanomaterials in the Gastrointestinal Environment. ACS Nano. 2018;12:8115–28.

145. Pedata P, Ricci G, Malorni L, Venezia A, Cammarota M, Volpe MG, et al. In vitro intestinal epithelium responses to titanium dioxide nanoparticles. Food Res Int. 2019;119:634–42.

146. Sousa A, Azevedo R, Costa VM, Oliveira S, Preguiça I, Viana S, et al. Biodistribution and intestinal inflammatory response following voluntary oral intake of silver nanoparticles by C57BL/6J mice. Arch Toxicol. 2023;97:2643–57.

147. Wang J, Zhou G, Chen C, Yu H, Wang T, Ma Y, et al. Acute toxicity and biodistribution of different sized titanium dioxide particles in mice after oral administration. Toxicol Lett. 2007;168:176–85.

148. Shrivastava R, Raza S, Yadav A, Kushwaha P, Flora SJS. Effects of sub-acute exposure to TiO2, ZnO and Al2O3 nanoparticles on oxidative stress and histological changes in mouse liver and brain. Drug Chem Toxicol. 2014;37:336–47.

149. Peterson MD, Mooseker MS. Characterization of the enterocyte-like brush border cytoskeleton of the C2BBe clones of the human intestinal cell line, Caco-2. J Cell Sci. 1992;102:581–600.

150. Gamboa JM, Leong KW. In vitro and in vivo models for the study of oral delivery of nanoparticles. Adv Drug Deliv Rev. 2013;65:800–10.

151. Mabbott NA, Donaldson DS, Ohno H, Williams IR, Mahajan A. Microfold (M) cells: important immunosurveillance posts in the intestinal epithelium. Mucosal Immunol. 2013;6:666–77.

152. Vincentini O, Prota V, Cecchetti S, Bertuccini L, Tinari A, Iosi F, et al. Towards the Standardization of Intestinal In Vitro Advanced Barrier Model

for Nanoparticles Uptake and Crossing: The SiO(2) Case Study. Cells. 2022;11.

153. Meirelles GC, Mendes C, Caon T, Teixeira HF, von Poser G, Ponchel G. Intestinal permeability enhancement of benzopyran HP1-loaded nanoemulsions. Eur J Pharm Sci. 2019;127:115–20.

154. Krupa L, Bajka B, Staroń R, Dupont D, Singh H, Gutkowski K, et al. Comparing the permeability of human and porcine small intestinal mucus for particle transport studies. Sci Rep. 2020;10:20290.

155. Liu T, Gu J, Fu C, Su L. Three-Dimensional Scaffolds for Intestinal Cell Culture: Fabrication, Utilization, and Prospects. Tissue Eng Part B Rev. 2023;

156. Brodkorb A, Egger L, Alminger M, Alvito P, Assunção R, Ballance S, et al. INFOGEST static in vitro simulation of gastrointestinal food digestion. Nat Protoc. 2019;14:991–1014.

157. Dudefoi W, Rabesona H, Rivard C, Mercier-Bonin M, Humbert B, Terrisse H, et al. In vitro digestion of food grade TiO(2) (E171) and TiO(2) nanoparticles: physicochemical characterization and impact on the activity of digestive enzymes. Food Funct. 2021;12:5975–88.

158. Quintriqueo-Cid A, Giménez B, Romero-Hasler P, Soto-Bustamante E, Lozano-Sánchez J, Robert P. Influence of the crystallinity on the physicochemical properties of spray-dried quercetin-inulin microparticles and their performance during in vitro digestion. Food Chem. 2024;434:137325.

159. Yu Y, Chen D, Lee YY, Chen N, Wang Y, Qiu C. Physicochemical and In Vitro Digestion Properties of Curcumin-Loaded Solid Lipid Nanoparticles with Different Solid Lipids and Emulsifiers. Foods. 2023;12.

160. Jabor Z, Sutton SC. Effects of Digestion, Cell Culture Media, and Mucous on the Physical Properties, Cellular Effects, and Translocation of Polystyrene and Polymethacrylate Nanoparticles. Toxics. 2023;11.

161. Ai C, Zhao C, Xiang C, Zheng Y, Zhong S, Teng H, et al. Gum arabic as a sole wall material for constructing nanoparticle to enhance the stability and bioavailability of curcumin. Food Chem X. 2023;18:100724.

162. Espada-Bernabé E, Moreno-Martín G, Gómez-Gómez B, Madrid Y. Assesing the behaviour of particulate/nanoparticulate form of E171 (TiO(2)) food additive in colored chocolate candies before and after in vitro oral

ingestion by spICP-MS, TEM and cellular in vitro models. Food Chem. 2024;432:137201.

163. Kokalari I, Gassino R, Giovannozzi AM, Croin L, Gazzano E, Bergamaschi E, et al. Pro- and anti-oxidant properties of near-infrared (NIR) light responsive carbon nanoparticles. Free Radic Biol Med. 2019;134:165–76.

164. Liu Z, Yao S, Li Y. Plasmonic-driven charge separation through combining Ag nanoparticles (Ag NPs) to form a double Z-scheme heterostructure in WO(3)/BiOCl/g-C(3)N(4) for the photocatalytic degradation of antibiotics. Dalton Trans. 2023;52:12999–3008.

165. Ogawa Y, Kawaguchi T, Tanaka M, Hashimoto A, Fukui K, Uekawa N, et al. Quenching effect of cerium oxide nanoparticles on singlet oxygen: validation of the potential for reaction with multiple reactive oxygen species. J Clin Biochem Nutr. 2023;73:1–8.

166. Dikalov SI, Polienko YF, Kirilyuk I. Electron Paramagnetic Resonance Measurements of Reactive Oxygen Species by Cyclic Hydroxylamine Spin Probes. Antioxid Redox Signal. 2018;28:1433–43.

167. Fu PP, Xia Q, Hwang HM, Ray PC, Yu H. Mechanisms of nanotoxicity: Generation of reactive oxygen species. J Food Drug Anal. 2014;22:64–75.

168. Abdal Dayem A, Hossain MK, Lee S Bin, Kim K, Saha SK, Yang G-M, et al. The Role of Reactive Oxygen Species (ROS) in the Biological Activities of Metallic Nanoparticles. Int J Mol Sci. 2017;18.

169. Risom L, Møller P, Loft S. Oxidative stress-induced DNA damage by particulate air pollution. Mutat Res. 2005;592:119–37.

170. Xia T, Kovochich M, Brant J, Hotze M, Sempf J, Oberley T, et al. Comparison of the Abilities of Ambient and Manufactured Nanoparticles To Induce Cellular Toxicity According to an Oxidative Stress Paradigm. Nano Lett. 2006;6:1794–807.

171. Zorov DB, Juhaszova M, Sollott SJ. Mitochondrial Reactive Oxygen Species (ROS) and ROS-Induced ROS Release. Physiol Rev. 2014;94:909–50.

172. Kokalari I, Keshavan S, Rahman M, Gazzano E, Barzan G, Mandrile L, et al. Efficacy, biocompatibility and degradability of carbon nanoparticles for photothermal therapy of lung cancer. Nanomedicine. 2021;16:689–707.

173. Tacu I, Kokalari I, Abollino O, Albrecht C, Malandrino M, Ferretti AM, et al. Mechanistic Insights into the Role of Iron, Copper, and Carbonaceous

Component on the Oxidative Potential of Ultrafine Particulate Matter. Chem Res Toxicol. 2021;34:767–79.

174. OECD. Test No. 442D: In Vitro Skin Sensitisation. 2022.

175. Kim S-H, Lee D, Lee J, Yang J-Y, Seok J, Jung K, et al. Evaluation of the skin sensitization potential of metal oxide nanoparticles using the ARE-Nrf2 Luciferase KeratinoSensTM assay. Toxicol Res. 2021;37:277–84.

176. Miranda RR, Oliveira ACS, Skytte L, Rasmussen KL, Kjeldsen F. Proteome-wide analysis reveals molecular pathways affected by AgNP in a ROS-dependent manner. Nanotoxicology. 2022;16:73–87.

177. Ag Seleci D, Tsiliki G, Werle K, Elam DA, Okpowe O, Seidel K, et al. Determining nanoform similarity via assessment of surface reactivity by abiotic and in vitro assays. NanoImpact. 2022;26:100390.

178. Tyanova S, Temu T, Cox J. The MaxQuant computational platform for mass spectrometry-based shotgun proteomics. Nat Protoc. 2016;11:2301–19.

179. Tyanova S, Temu T, Sinitcyn P, Carlson A, Hein MY, Geiger T, et al. The Perseus computational platform for comprehensive analysis of (prote)omics data. Nat Methods. 2016;13:731–40.

180. Sambuy Y, De Angelis I, Ranaldi G, Scarino ML, Stammati A, Zucco F. The Caco-2 cell line as a model of the intestinal barrier: influence of cell and culture-related factors on Caco-2 cell functional characteristics. Cell Biol Toxicol. 2005;21:1–26.

181. Dorier M, Tisseyre C, Dussert F, Béal D, Arnal ME, Douki T, et al. Toxicological impact of acute exposure to E171 food additive and TiO2 nanoparticles on a co-culture of Caco-2 and HT29-MTX intestinal cells. Mutation Research/Genetic Toxicology and Environmental Mutagenesis. 2019;845:402980.

182. Dussert F, Wegner KD, Moriscot C, Gallet B, Jouneau P-H, Reiss P, et al. Evaluation of the Dermal Toxicity of InZnP Quantum Dots Before and After Accelerated Weathering: Toward a Safer-By-Design Strategy. Frontiers in Toxicology. 2021;3:6.

183. Konishi Y, Hagiwara K, Shimizu M. Transepithelial transport of fluorescein in Caco-2 cell monolayers and use of such transport in in vitro

evaluation of phenolic acid availability. Biosci Biotechnol Biochem. 2002;66:2449–57.

184. Jeitner TM. Optimized ferrozine-based assay for dissolved iron. Anal Biochem. 2014;454:36–7.

185. Balivada S, Rachakatla RS, Wang H, Samarakoon TN, Dani RK, Pyle M, et al. A/C magnetic hyperthermia of melanoma mediated by iron(0)/iron oxide core/shell magnetic nanoparticles: a mouse study. BMC Cancer. 2010;10:119.

186. ANalisys Of VAriance. p. https://astatsa.com/OneWay_Anova_with_TukeyHSD/.

187. Schoepf JJ, Bi Y, Kidd J, Herckes P, Hristovski K, Westerhoff P. Detection and dissolution of needle-like hydroxyapatite nanomaterials in infant formula. NanoImpact. 2017;5:22–8.

188. HUANG Y, QI M, ZHANG M, LIU H, YANG D. Degradation mechanisms of poly (lactic-co-glycolic acid) films in vitro under static and dynamic environment. Transactions of Nonferrous Metals Society of China. 2006;16:s293–7.

189. Feeney OM, Williams HD, Pouton CW, Porter CJH. “Stealth” lipid-based formulations: poly(ethylene glycol)-mediated digestion inhibition improves oral bioavailability of a model poorly water soluble drug. J Control Release. 2014;192:219–27.

190. Antonello G, Marucco A, Gazzano E, Kainourgios P, Ravagli C, Gonzalez-Paredes A, et al. Changes of physico-chemical properties of nano-biomaterials by digestion fluids affect the physiological properties of epithelial intestinal cells and barrier models. Part Fibre Toxicol. 2022;19:49.

191. Marucco A, Carella E, Fenoglio I. A comparative study on the efficacy of different probes to predict the photo-activity of nano-titanium dioxide toward biomolecules. RSC Adv. 2015;5:89559–68.

192. Monopoli MP, Pitek AS, Lynch I, Dawson KA. Formation and characterization of the nanoparticle-protein corona. Methods Mol Biol. 2013;1025:137–55.

193. Zheng X, Baker H, Hancock WS, Fawaz F, McCaman M, Pungor EJ. Proteomic analysis for the assessment of different lots of fetal bovine serum

as a raw material for cell culture. Part IV. Application of proteomics to the manufacture of biological drugs. Biotechnol Prog. 2006;22:1294–300.

194. Ferruzza S, Rossi C, Scarino ML, Sambuy Y. A protocol for in situ enzyme assays to assess the differentiation of human intestinal Caco-2 cells. Toxicol In Vitro. 2012;26:1247–51.

195. Matsumoto T, Kaifuchi N, Mizuhara Y, Warabi E, Watanabe J. Use of a Caco-2 permeability assay to evaluate the effects of several Kampo medicines on the drug transporter P-glycoprotein. J Nat Med. 2018;72:897–904.

196. Shekhawat P, Bagul M, Edwankar D, Pokharkar V. Enhanced dissolution/caco-2 permeability, pharmacokinetic and pharmacodynamic performance of re-dispersible eprosartan mesylate nanopowder. Eur J Pharm Sci. 2019;132:72–85.

197. Susewind J, de Souza Carvalho-Wodarz C, Repnik U, Collnot E-M, Schneider-Daum N, Griffiths GW, et al. A 3D co-culture of three human cell lines to model the inflamed intestinal mucosa for safety testing of nanomaterials. Nanotoxicology. 2016;10:53–62.

198. Ishiguro Y. Mucosal proinflammatory cytokine production correlates with endoscopic activity of ulcerative colitis. J Gastroenterol. 1999;34:66–74.

199. Kühn R, Löhler J, Rennick D, Rajewsky K, Müller W. Interleukin-10-deficient mice develop chronic enterocolitis. Cell. 1993;75:263–74.

200. Lindemans CA, Calafiore M, Mertelsmann AM, O'Connor MH, Dudakov JA, Jenq RR, et al. Interleukin-22 promotes intestinal-stem-cell-mediated epithelial regeneration. Nature. 2015;528:560–4.

201. Lo BC, Shin SB, Canals Hernaez D, Refaeli I, Yu HB, Goebeler V, et al. IL-22 Preserves Gut Epithelial Integrity and Promotes Disease Remission during Chronic Salmonella Infection. J Immunol. 2019;202:956–65.

202. Miller MR, Raftis JB, Langrish JP, McLean SG, Samutrtai P, Connell SP, et al. Inhaled Nanoparticles Accumulate at Sites of Vascular Disease. ACS Nano. 2017;11:4542–52.

203. Milto I V, Ivanova V V, Shevtsova NM, Sukhodolo I V. Rat Blood Leukocytes after Intravenous Injection of Chitosan-Modified Magnetic Nanospheres. Bull Exp Biol Med. 2020;168:785–8.

204. Stefaniak AB, Duling MG, Lawrence RB, Thomas TA, LeBouf RF, Wade EE, et al. Dermal exposure potential from textiles that contain silver nanoparticles. Int J Occup Environ Health. 2014;20:220–34.

205. Lamson NG, Berger A, Fein KC, Whitehead KA. Anionic nanoparticles enable the oral delivery of proteins by enhancing intestinal permeability. Nat Biomed Eng. 2020;4:84–96.

206. Xavier M, García-Hevia L, Amado IR, Pastrana L, Gonçalves C. In Vitro Intestinal Uptake And Permeability Of Fluorescently-Labelled Hyaluronic Acid Nanogels. Int J Nanomedicine. 2019;14:9077–88.

207. Lima IA de, Khalil NM, Tominaga TT, Lechanteur A, Sarmento B, Mainardes RM. Mucoadhesive chitosan-coated PLGA nanoparticles for oral delivery of ferulic acid. Artif Cells Nanomed Biotechnol. 2018;46:993–1002.

208. Tian Y, Xu J, Li Y, Zhao R, Du S, Lv C, et al. MicroRNA-31 Reduces Inflammatory Signaling and Promotes Regeneration in Colon Epithelium, and Delivery of Mimics in Microspheres Reduces Colitis in Mice. Gastroenterology. 2019;156:2281-2296.e6.

209. Bouwmeester H, van der Zande M, Jepson MA. Effects of food-borne nanomaterials on gastrointestinal tissues and microbiota. WIREs Nanomedicine and Nanobiotechnology. 2018;10:e1481.

210. Lin Q, Liang R, Ye A, Singh H, Zhong F. Effects of calcium on lipid digestion in nanoemulsions stabilized by modified starch: Implications for bioaccessibility of β-carotene. Food Hydrocoll. 2017;73:184–93.

211. Bourlieu C, Ménard O, Bouzerzour K, Mandalari G, Macierzanka A, Mackie AR, et al. Specificity of infant digestive conditions: some clues for developing relevant in vitro models. Crit Rev Food Sci Nutr. 2014;54:1427–57.

212. Llewellyn S V, Kämpfer A, Keller JG, Vilsmeier K, Büttner V, Ag Seleci D, et al. Simulating Nanomaterial Transformation in Cascaded Biological Compartments to Enhance the Physiological Relevance of In Vitro Dosing Regimes: Optional or Required? Small. 2021;17:e2004630.

213. Bitounis D, Parviz D, Cao X, Amadei CA, Vecitis CD, Sunderland EM, et al. Synthesis and Physicochemical Transformations of Size-Sorted Graphene Oxide during Simulated Digestion and Its Toxicological Assessment against an In Vitro Model of the Human Intestinal Epithelium. Small. 2020;16:e1907640.

214. Gerloff K, Pereira DIA, Faria N, Boots AW, Kolling J, Förster I, et al. Influence of simulated gastrointestinal conditions on particle-induced cytotoxicity and interleukin-8 regulation in differentiated and undifferentiated Caco-2 cells. Nanotoxicology. 2013;7:353–66.

215. Abdelkhaliq A, van der Zande M, Undas AK, Peters RJB, Bouwmeester H. Impact of in vitro digestion on gastrointestinal fate and uptake of silver nanoparticles with different surface modifications. Nanotoxicology. 2020;14:111–26.

216. Zaiter T, Cornu R, Millot N, Herbst M, Pellequer Y, Moarbess G, et al. Size effect and mucus role on the intestinal toxicity of the E551 food additive and engineered silica nanoparticles. Nanotoxicology. 2022;16:165–82.

217. Kose O, Béal D, Motellier S, Pelissier N, Collin-Faure V, Blosi M, et al. Physicochemical Transformations of Silver Nanoparticles in the Oro-Gastrointestinal Tract Mildly Affect Their Toxicity to Intestinal Cells In Vitro: An AOP-Oriented Testing Approach. Toxics. 2023;11.

218. Nel A, Xia T, Mädler L, Li N. Toxic potential of materials at the nanolevel. Science. 2006;311:622–7.

219. Fubini B, Ghiazza M, Fenoglio I. Physico-chemical features of engineered nanoparticles relevant to their toxicity. Nanotoxicology. 2010;4:347–63.

220. Prokopovich P. Interactions between mammalian cells and nano- or micro-sized wear particles: physico-chemical views against biological approaches. Adv Colloid Interface Sci. 2014;213:36–47.

221. Gehr P. Interaction of nanoparticles with biological systems. Colloids Surf B Biointerfaces. 2018;172:395–9.

222. Hinderliter PM, Minard KR, Orr G, Chrisler WB, Thrall BD, Pounds JG, et al. ISDD: A computational model of particle sedimentation, diffusion and target cell dosimetry for in vitro toxicity studies. Part Fibre Toxicol. 2010;7:36.

223. Marucco A, Aldieri E, Leinardi R, Bergamaschi E, Riganti C, Fenoglio I. Applicability and Limitations in the Characterization of Poly-Dispersed Engineered Nanomaterials in Cell Media by Dynamic Light Scattering (DLS). Materials (Basel). 2019;12.

224. Gonzalez-Paredes A, Torres D, Alonso MJ. Polyarginine nanocapsules: A versatile nanocarrier with potential in transmucosal drug delivery. Int J Pharm. 2017;529:474–85.

225. Ault AP, Stark DI, Axson JL, Keeney JN, Maynard AD, Bergin IL, et al. Protein Corona-Induced Modification of Silver Nanoparticle Aggregation in Simulated Gastric Fluid. Environ Sci Nano. 2016;3:1510–20.

226. Walczak AP, Fokkink R, Peters R, Tromp P, Herrera Rivera ZE, Rietjens IMCM, et al. Behaviour of silver nanoparticles and silver ions in an in vitro human gastrointestinal digestion model. Nanotoxicology. 2013;7:1198–210.

227. Coreas R, Cao X, Deloid GM, Demokritou P, Zhong W. Lipid and protein corona of food-grade TiO(2) nanoparticles in simulated gastrointestinal digestion. NanoImpact. 2020;20.

228. Sakai-Kato K, Hidaka M, Un K, Kawanishi T, Okuda H. Physicochemical properties and in vitro intestinal permeability properties and intestinal cell toxicity of silica particles, performed in simulated gastrointestinal fluids. Biochim Biophys Acta. 2014;1840:1171–80.

229. Gelli R, Tempesti P, Ridi F, Baglioni P. Formation and properties of amorphous magnesium-calcium phosphate particles in a simulated intestinal fluid. J Colloid Interface Sci. 2019;546:130–8.

230. Jiang X, Zhang X, Gray P, Zheng J, Croley TR, Fu PP, et al. Influences of simulated gastrointestinal environment on physicochemical properties of gold nanoparticles and their implications on intestinal epithelial permeability. J Environ Sci Health C Environ Carcinog Ecotoxicol Rev. 2019;37:116–31.

231. Gou J, Feng S, Liang Y, Fang G, Zhang H, Yin T, et al. Polyester-Solid Lipid Mixed Nanoparticles with Improved Stability in Gastro-Intestinal Tract Facilitated Oral Delivery of Larotaxel. Mol Pharm. 2017;14:3750–61.

232. Li Z, Ha J, Zou T, Gu L. Fabrication of coated bovine serum albumin (BSA)-epigallocatechin gallate (EGCG) nanoparticles and their transport across monolayers of human intestinal epithelial Caco-2 cells. Food Funct. 2014;5:1278–85.

233. Ibrahim HM, Awad M, Al-Farraj AS, Al-Turki AM. Stability and Dynamic Aggregation of Bare and Stabilized Zero-Valent Iron Nanoparticles under Variable Solution Chemistry. Nanomaterials (Basel). 2020;10.

234. He X, Zhang H, Shi H, Liu W, Sahle-Demessie E. Fates of Au, Ag, ZnO, and CeO(2) Nanoparticles in Simulated Gastric Fluid Studied using Single-Particle-Inductively Coupled Plasma-Mass Spectrometry. J Am Soc Mass Spectrom. 2020;31:2180–90.

235. Rogers KR, Bradham K, Tolaymat T, Thomas DJ, Hartmann T, Ma L, et al. Alterations in physical state of silver nanoparticles exposed to synthetic human stomach fluid. Sci Total Environ. 2012;420:334–9.

236. Asadi E, Azodi-Deilami S, Abdouss M, Khaghani S. Cyproterone synthesis, recognition and controlled release by molecularly imprinted nanoparticle. Appl Biochem Biotechnol. 2012;167:2076–87.

237. Jannin V, Dellera E, Chevrier S, Chavant Y, Voutsinas C, Bonferoni C, et al. In vitro lipolysis tests on lipid nanoparticles: comparison between lipase/co-lipase and pancreatic extract. Drug Dev Ind Pharm. 2015;41:1582–8.

238. Ban C, Jo M, Lim S, Choi YJ. Control of the gastrointestinal digestion of solid lipid nanoparticles using PEGylated emulsifiers. Food Chem. 2018;239:442–52.

239. Gonçalves RFS, Martins JT, Abrunhosa L, Baixinho J, Matias AA, Vicente AA, et al. Lipid-based nanostructures as a strategy to enhance curcumin bioaccessibility: Behavior under digestion and cytotoxicity assessment. Food Res Int. 2021;143:110278.

240. Zöller K, To D, Knoll P, Bernkop-Schnürch A. Digestion of lipid excipients and lipid-based nanocarriers by pancreatic lipase and pancreatin. Eur J Pharm Biopharm. 2022;176:32–42.

241. Hosseinidoust Z, Alam MN, Sim G, Tufenkji N, van de Ven TGM. Cellulose nanocrystals with tunable surface charge for nanomedicine. Nanoscale. 2015;7:16647–57.

242. Wang J, Zhang L, Peng F, Shi X, Leong DT. Targeting Endothelial Cell Junctions with Negatively Charged Gold Nanoparticles. Chemistry of Materials. 2018;30:3759–67.

243. Schleh C, Semmler-Behnke M, Lipka J, Wenk A, Hirn S, Schäffler M, et al. Size and surface charge of gold nanoparticles determine absorption across intestinal barriers and accumulation in secondary target organs after oral administration. Nanotoxicology. 2012;6:36–46.

244. Walczyk D, Bombelli FB, Monopoli MP, Lynch I, Dawson KA. What the cell “sees” in bionanoscience. J Am Chem Soc. 2010;132:5761–8.

245. Kumar S, Yadav I, Aswal VK, Kohlbrecher J. Structure and Interaction of Nanoparticle-Protein Complexes. Langmuir. 2018;34:5679–95.

246. Ranjan S, Dasgupta N, Sudandiradoss C, Ramalingam C, Kumar A. Titanium dioxide nanoparticle-protein interaction explained by docking approach. Int J Nanomedicine. 2018;13:47–50.

247. Bhogale A, Patel N, Sarpotdar P, Mariam J, Dongre PM, Miotello A, et al. Systematic investigation on the interaction of bovine serum albumin with ZnO nanoparticles using fluorescence spectroscopy. Colloids Surf B Biointerfaces. 2013;102:257–64.

248. Sasidharan A, Chandran P, Monteiro-Riviere NA. Biocorona Bound Gold Nanoparticles Augment Their Hematocompatibility Irrespective of Size or Surface Charge. ACS Biomater Sci Eng. 2016;2:1608–18.

249. Setyawati MI, Zhao Z, Ng KW. Transformation of Nanomaterials and Its Implications in Gut Nanotoxicology. Small. 2020;16:e2001246.

250. Lundqvist M, Stigler J, Cedervall T, Berggård T, Flanagan MB, Lynch I, et al. The evolution of the protein corona around nanoparticles: a test study. ACS Nano. 2011;5:7503–9.

251. Maiorano G, Sabella S, Sorce B, Brunetti V, Malvindi MA, Cingolani R, et al. Effects of cell culture media on the dynamic formation of protein-nanoparticle complexes and influence on the cellular response. ACS Nano. 2010;4:7481–91.

252. Tsoi KM, MacParland SA, Ma X-Z, Spetzler VN, Echeverri J, Ouyang B, et al. Mechanism of hard-nanomaterial clearance by the liver. Nat Mater. 2016;15:1212–21.

253. Yu M, Song W, Tian F, Dai Z, Zhu Q, Ahmad E, et al. Temperature- and rigidity-mediated rapid transport of lipid nanovesicles in hydrogels. Proc Natl Acad Sci U S A. 2019;116:5362–9.

254. Choki K, Li S, Ye A, Jameson GB, Singh H. Fate of hydroxyapatite nanoparticles during dynamic in vitro gastrointestinal digestion: the impact of milk as a matrix. Food Funct. 2021;12:2760–71.

255. Levak M, Burić P, Dutour Sikirić M, Domazet Jurašin D, Mikac N, Bačić N, et al. Effect of Protein Corona on Silver Nanoparticle Stabilization and Ion

Release Kinetics in Artificial Seawater. Environ Sci Technol. 2017;51:1259–66.

256. Martin MN, Allen AJ, MacCuspie RI, Hackley VA. Dissolution, agglomerate morphology, and stability limits of protein-coated silver nanoparticles. Langmuir. 2014;30:11442–52.

257. Chao Y, Marsh AI, Behray M, Guan F, Engdahl A, Chao Y, et al. Synthesis and characterisation of isothiocyanate functionalised silicon nanoparticles and their uptake in cultured colonic cells. Faraday Discuss. 2020;222:332–49.

258. Marchiando AM, Graham WV, Turner JR. Epithelial barriers in homeostasis and disease. Annu Rev Pathol. 2010;5:119–44.

259. Al-Sadi R, Boivin M, Ma T. Mechanism of cytokine modulation of epithelial tight junction barrier. Front Biosci (Landmark Ed). 2009;14:2765–78.

260. Van Spaendonk H, Ceuleers H, Witters L, Patteet E, Joossens J, Augustyns K, et al. Regulation of intestinal permeability: The role of proteases. World J Gastroenterol. 2017;23:2106–23.

261. Brun E, Barreau F, Veronesi G, Fayard B, Sorieul S, Chanéac C, et al. Titanium dioxide nanoparticle impact and translocation through ex vivo, in vivo and in vitro gut epithelia. Part Fibre Toxicol. 2014;11:13.

262. Cao X, Khare S, DeLoid GM, Gokulan K, Demokritou P. Co-exposure to boscalid and TiO2 (E171) or SiO2 (E551) downregulates cell junction gene expression in small intestinal epithelium cellular model and increases pesticide translocation. NanoImpact. 2021;22:100306.

263. Zhang Y, Duan S, Liu Y, Wang Y. The combined effect of food additive titanium dioxide and lipopolysaccharide on mouse intestinal barrier function after chronic exposure of titanium dioxide-contained feedstuffs. Part Fibre Toxicol. 2021;18:8.

264. Lee Y, Kamada N, Moon JJ. Oral nanomedicine for modulating immunity, intestinal barrier functions, and gut microbiome. Adv Drug Deliv Rev. 2021;179:114021.

265. Tang M, Li S, Wei L, Hou Z, Qu J, Li L. Do Engineered Nanomaterials Affect Immune Responses by Interacting With Gut Microbiota? Front Immunol. 2021;12:684605.

266. Goto Y. Epithelial Cells as a Transmitter of Signals From Commensal Bacteria and Host Immune Cells. Front Immunol. 2019;10:2057.

267. Colombo G, Cortinovis C, Moschini E, Bellitto N, Perego MC, Albonico M, et al. Cytotoxic and proinflammatory responses induced by ZnO nanoparticles in in vitro intestinal barrier. J Appl Toxicol. 2019;39:1155–63.

268. Busch M, Bredeck G, Kämpfer AAM, Schins RPF. Investigations of acute effects of polystyrene and polyvinyl chloride micro- and nanoplastics in an advanced in vitro triple culture model of the healthy and inflamed intestine. Environ Res. 2021;193:110536.

269. Gao T, Wang Z, Dong Y, Cao J, Lin R, Wang X, et al. Role of melatonin in sleep deprivation-induced intestinal barrier dysfunction in mice. J Pineal Res. 2019;67:e12574.

270. Kiss J, Lamarque D, Delchier JC, Whittle BJ. Time-dependent actions of nitric oxide synthase inhibition on colonic inflammation induced by trinitrobenzene sulphonic acid in rats. Eur J Pharmacol. 1997;336:219–24.

271. Yoshida Y, Iwai A, Itoh K, Tanaka M, Kato S, Hokari R, et al. Role of inducible nitric oxide synthase in dextran sulphate sodium-induced colitis. Aliment Pharmacol Ther. 2000;14 Suppl 1:26–32.

272. Hosoi T, Goto H, Arisawa T, Niwa Y, Okada N, Ohmiya N, et al. Role of nitric oxide synthase inhibitor in experimental colitis induced by 2,4,6-trinitrobenzene sulphonic acid in rats. Clin Exp Pharmacol Physiol. 2001;28:9–12.

273. Kelly CP, Murray JA, Leffler DA, Getts DR, Bledsoe AC, Smithson G, et al. TAK-101 Nanoparticles Induce Gluten-Specific Tolerance in Celiac Disease: A Randomized, Double-Blind, Placebo-Controlled Study. Gastroenterology. 2021;161:66-80.e8.

274. Gillmore JD, Gane E, Taubel J, Kao J, Fontana M, Maitland ML, et al. CRISPR-Cas9 In Vivo Gene Editing for Transthyretin Amyloidosis. N Engl J Med. 2021;385:493–502.

275. Aldrich C, Leroux-Roels I, Huang KB, Bica MA, Loeliger E, Schoenborn-Kellenberger O, et al. Proof-of-concept of a low-dose unmodified mRNA-based rabies vaccine formulated with lipid nanoparticles in human volunteers: A phase 1 trial. Vaccine. 2021;39:1310–8.

276. Gao T, Wang Z, Cao J, Dong Y, Chen Y. Melatonin alleviates oxidative stress in sleep deprived mice: Involvement of small intestinal mucosa injury. Int Immunopharmacol. 2020;78:106041.

277. Akcan A, Kucuk C, Sozuer E, Esel D, Akyildiz H, Akgun H, et al. Melatonin reduces bacterial translocation and apoptosis in trinitrobenzene sulphonic acid-induced colitis of rats. World J Gastroenterol. 2008;14:918–24.

278. Gao T, Wang T, Wang Z, Cao J, Dong Y, Chen Y. Melatonin-mediated MT2 attenuates colitis induced by dextran sodium sulfate via PI3K/AKT/Nrf2/SIRT1/RORα/NF-κB signaling pathways. Int Immunopharmacol. 2021;96:107779.

279. Sánchez AB, Clares B, Rodríguez-Lagunas MJ, Fábrega MJ, Calpena AC. Study of Melatonin as Preventive Agent of Gastrointestinal Damage Induced by Sodium Diclofenac. Cells. 2020;9.

280. Abdulridha MK. POTENTIAL MODULATION OF DISEASE ACTIVITY INDICES AND INFLAMMATORY BIOMARKERS IN PATIENTS WITH ACTIVE INFLAMMATORY BOWEL DISEASE ON MELATONIN ADJUVANT THERAPY. Asian Journal of Pharmaceutical and Clinical Research. 2018;11:476–481.

281. Chojnacki C, Wisniewska-Jarosinska M, Walecka-Kapica E, Klupinska G, Jaworek J, Chojnacki J. Evaluation of melatonin effectiveness in the adjuvant treatment of ulcerative colitis. J Physiol Pharmacol. 2011;62:327–34.

282. Lin R, Wang Z, Cao J, Gao T, Dong Y, Chen Y. Role of melatonin in intestinal mucosal injury induced by restraint stress in mice. Pharm Biol. 2020;58:342–51.

283. Rutgeerts P, Sandborn WJ, Feagan BG, Reinisch W, Olson A, Johanns J, et al. Infliximab for induction and maintenance therapy for ulcerative colitis. N Engl J Med. 2005;353:2462–76.

284. Wei W, Mu S, Han Y, Chen Y, Kuang Z, Wu X, et al. Gpr174 Knockout Alleviates DSS-Induced Colitis via Regulating the Immune Function of Dendritic Cells. Front Immunol. 2022;13:841254.

285. Straub RH, Lehle K, Herfarth H, Weber M, Falk W, Preuner J, et al. Dehydroepiandrosterone in relation to other adrenal hormones during an acute inflammatory stressful disease state compared with chronic inflammatory disease: role of interleukin-6 and tumour necrosis factor. Eur J Endocrinol. 2002;146:365–74.

286. Rogy MA, Beinhauer BG, Reinisch W, Huang L, Pokieser P. Transfer of interleukin-4 and interleukin-10 in patients with severe inflammatory bowel disease of the rectum. Hum Gene Ther. 2000;11:1731–41.

287. Naganuma M, Sugimoto S, Mitsuyama K, Kobayashi T, Yoshimura N, Ohi H, et al. Efficacy of Indigo Naturalis in a Multicenter Randomized Controlled Trial of Patients With Ulcerative Colitis. Gastroenterology. 2018;154:935–47.

288. Sasaki M, Jordan P, Joh T, Itoh M, Jenkins M, Pavlick K, et al. Melatonin reduces TNF-a induced expression of MAdCAM-1 via inhibition of NF-kappaB. BMC Gastroenterol. 2002;2:9.

289. Cui W, Li LX, Sun CM, Wen Y, Zhou Y, Dong YL, et al. Tumor necrosis factor alpha increases epithelial barrier permeability by disrupting tight junctions in Caco-2 cells. Braz J Med Biol Res. 2010;43:330–7.

290. D'Haens G, Baert F, van Assche G, Caenepeel P, Vergauwe P, Tuynman H, et al. Early combined immunosuppression or conventional management in patients with newly diagnosed Crohn's disease: an open randomised trial. Lancet. 2008;371:660–7.

291. Franke A, Balschun T, Karlsen TH, Sventoraityte J, Nikolaus S, Mayr G, et al. Sequence variants in IL10, ARPC2 and multiple other loci contribute to ulcerative colitis susceptibility. Nat Genet. 2008;40:1319–23.

292. Neufert C, Pickert G, Zheng Y, Wittkopf N, Warntjen M, Nikolaev A, et al. Activation of epithelial STAT3 regulates intestinal homeostasis. Cell Cycle. 2010;9:652–5.

293. Chaudhry A, Samstein RM, Treuting P, Liang Y, Pils MC, Heinrich J-M, et al. Interleukin-10 signaling in regulatory T cells is required for suppression of Th17 cell-mediated inflammation. Immunity. 2011;34:566–78.

294. Rubtsov YP, Rasmussen JP, Chi EY, Fontenot J, Castelli L, Ye X, et al. Regulatory T cell-derived interleukin-10 limits inflammation at environmental interfaces. Immunity. 2008;28:546–58.

295. Habil N, Abate W, Beal J, Foey AD. Heat-killed probiotic bacteria differentially regulate colonic epithelial cell production of human β-defensin-2: dependence on inflammatory cytokines. Benef Microbes. 2014;5:483–95.

296. Zenewicz LA, Yancopoulos GD, Valenzuela DM, Murphy AJ, Stevens S, Flavell RA. Innate and adaptive interleukin-22 protects mice from inflammatory bowel disease. Immunity. 2008;29:947–57.

297. Lema I, Araújo JR, Rolhion N, Demignot S. Jejunum: The understudied meeting place of dietary lipids and the microbiota. Biochimie. 2020;178:124–36.

298. Kominsky DJ, Campbell EL, Ehrentraut SF, Wilson KE, Kelly CJ, Glover LE, et al. IFN-γ-mediated induction of an apical IL-10 receptor on polarized intestinal epithelia. J Immunol. 2014;192:1267–76.

299. Gullberg E, Leonard M, Karlsson J, Hopkins AM, Brayden D, Baird AW, et al. Expression of specific markers and particle transport in a new human intestinal M-cell model. Biochem Biophys Res Commun. 2000;279:808–13.

300. Giusti S, Sbrana T, La Marca M, Di Patria V, Martinucci V, Tirella A, et al. A novel dual-flow bioreactor simulates increased fluorescein permeability in epithelial tissue barriers. Biotechnol J. 2014;9:1175–84.

301. IVTech web page [Internet]. Available from: https://www.ivtech.it/

302. Schwabl P, Köppel S, Königshofer P, Bucsics T, Trauner M, Reiberger T, et al. Detection of Various Microplastics in Human Stool: A Prospective Case Series. Ann Intern Med. 2019;171:453–7.

303. Bradney L, Wijesekara H, Palansooriya KN, Obadamudalige N, Bolan NS, Ok YS, et al. Particulate plastics as a vector for toxic trace-element uptake by aquatic and terrestrial organisms and human health risk. Environ Int. 2019;131:104937.

304. Horton AA, Walton A, Spurgeon DJ, Lahive E, Svendsen C. Microplastics in freshwater and terrestrial environments: Evaluating the current understanding to identify the knowledge gaps and future research priorities. Sci Total Environ. 2017;586:127–41.

305. Pan F, Han L, Zhang Y, Yu Y, Liu J. Optimization of Caco-2 and HT29 co-culture in vitro cell models for permeability studies. Int J Food Sci Nutr. 2015;66:680–5.

306. Ude VC, Brown DM, Stone V, Johnston HJ. Using 3D gastrointestinal tract in vitro models with microfold cells and mucus secreting ability to assess the hazard of copper oxide nanomaterials. J Nanobiotechnology. 2019;17:70.

307. Neutra MR, Pringault E, Kraehenbuhl JP. Antigen sampling across epithelial barriers and induction of mucosal immune responses. Annu Rev Immunol. 1996;14:275–300.

308. Gupta PN, Khatri K, Goyal AK, Mishra N, Vyas SP. M-cell targeted biodegradable PLGA nanoparticles for oral immunization against hepatitis B. J Drug Target. 2007;15:701–13.

309. Sigurdsson HH, Kirch J, Lehr C-M. Mucus as a barrier to lipophilic drugs. Int J Pharm. 2013;453:56–64.

310. Lefebvre DE, Venema K, Gombau L, Valerio LGJ, Raju J, Bondy GS, et al. Utility of models of the gastrointestinal tract for assessment of the digestion and absorption of engineered nanomaterials released from food matrices. Nanotoxicology. 2015;9:523–42.

311. Hollander D, Kaunitz JD. The “Leaky Gut”: Tight Junctions but Loose Associations? Dig Dis Sci. 2020;65:1277–87.

312. Maib H, Smythe E, Ayscough K. Forty years on: clathrin-coated pits continue to fascinate. Mol Biol Cell. 2017;28:843–7.

313. Antunes F, Andrade F, Araújo F, Ferreira D, Sarmento B. Establishment of a triple co-culture in vitro cell models to study intestinal absorption of peptide drugs. Eur J Pharm Biopharm. 2013;83:427–35.

314. Béduneau A, Tempesta C, Fimbel S, Pellequer Y, Jannin V, Demarne F, et al. A tunable Caco-2/HT29-MTX co-culture model mimicking variable permeabilities of the human intestine obtained by an original seeding procedure. Eur J Pharm Biopharm. 2014;87:290–8.

315. Lozoya-Agullo I, Araújo F, González-Álvarez I, Merino-Sanjuán M, González-Álvarez M, Bermejo M, et al. Usefulness of Caco-2/HT29-MTX and Caco-2/HT29-MTX/Raji B Coculture Models To Predict Intestinal and Colonic Permeability Compared to Caco-2 Monoculture. Mol Pharm. 2017;14:1264–70.

316. Gong M, Yang G, Zhuang L, Zeng EY. Microbial biofilm formation and community structure on low-density polyethylene microparticles in lake water microcosms. Environ Pollut. 2019;252:94–102.

317. Pennino MG, Bachiller E, Lloret-Lloret E, Albo-Puigserver M, Esteban A, Jadaud A, et al. Ingestion of microplastics and occurrence of parasite

association in Mediterranean anchovy and sardine. Mar Pollut Bull. 2020;158:111399.

318. Zhang D, Cui Y, Zhou H, Jin C, Yu X, Xu Y, et al. Microplastic pollution in water, sediment, and fish from artificial reefs around the Ma'an Archipelago, Shengsi, China. Sci Total Environ. 2020;703:134768.

319. Walkinshaw C, Lindeque PK, Thompson R, Tolhurst T, Cole M. Microplastics and seafood: lower trophic organisms at highest risk of contamination. Ecotoxicol Environ Saf. 2020;190:110066.

320. Lerebours A, Bathie M, Kazour M, Amara R, Huet V, Thomas H. Spatio-temporal contamination of microplastics in shellfish farming regions: A case study. Mar Pollut Bull. 2022;181:113842.

321. Ritchie JM, Rui H, Zhou X, Iida T, Kodoma T, Ito S, et al. Inflammation and disintegration of intestinal villi in an experimental model for Vibrio parahaemolyticus-induced diarrhea. PLoS Pathog. 2012;8:e1002593.

322. Wang S, Zhang Z, Malakar PK, Pan Y, Zhao Y. The Fate of Bacteria in Human Digestive Fluids: A New Perspective Into the Pathogenesis of Vibrio parahaemolyticus. Front Microbiol. 2019;10:1614.

323. Shimohata T, Nakano M, Lian X, Shigeyama T, Iba H, Hamamoto A, et al. Vibrio parahaemolyticus infection induces modulation of IL-8 secretion through dual pathway via VP1680 in Caco-2 cells. J Infect Dis. 2011;203:537–44.

324. Wang Y, Zhao Y, Pan Y, Liu H. Comparison on the Growth Variability of Vibrio parahaemolyticus Coupled With Strain Sources and Genotypes Analyses in Simulated Gastric Digestion Fluids. Front Microbiol. 2020;11:212.

325. Qin X, Zhuang Y, Ma J, Liu S, Shi B. Enhanced toxicity effects of iron particles together with PFOA in drinking water. Environ Pollut. 2022;311:119919.

326. Akbari A, Lavasanifar A, Wu J. Interaction of cruciferin-based nanoparticles with Caco-2 cells and Caco-2/HT29-MTX co-cultures. Acta Biomater. 2017;64:249–58.

327. Hoffmann P, Burmester M, Langeheine M, Brehm R, Empl MT, Seeger B, et al. Caco-2/HT29-MTX co-cultured cells as a model for studying physiological properties and toxin-induced effects on intestinal cells. PLoS One. 2021;16:e0257824.

328. Gillois K, Stoffels C, Leveque M, Fourquaux I, Blesson J, Mils V, et al. Repeated exposure of Caco-2 versus Caco-2/HT29-MTX intestinal cell models to (nano)silver in vitro: Comparison of two commercially available colloidal silver products. Sci Total Environ. 2021;754:142324.

329. Finn R, Ahmad T, Coffey ET, Brayden DJ, Baird AW, Boyd A. Translocation of Vibrio parahaemolyticus across an in vitro M cell model. FEMS Microbiol Lett. 2014;350:65–71.

330. Mahler GJ, Shuler ML, Glahn RP. Characterization of Caco-2 and HT29-MTX cocultures in an in vitro digestion/cell culture model used to predict iron bioavailability. J Nutr Biochem. 2009;20:494–502.

331. Kämpfer AAM, Busch M, Büttner V, Bredeck G, Stahlmecke B, Hellack B, et al. Model Complexity as Determining Factor for In Vitro Nanosafety Studies: Effects of Silver and Titanium Dioxide Nanomaterials in Intestinal Models. Small. 2021;17:e2004223.

332. Yuan L, van der Mei HC, Busscher HJ, Peterson BW. Two-Stage Interpretation of Changes in TEER of Intestinal Epithelial Layers Protected by Adhering Bifidobacteria During E. coli Challenges. Front Microbiol. 2020;11:599555.

333. Piret J-P, Vankoningsloo S, Mejia J, Noël F, Boilan E, Lambinon F, et al. Differential toxicity of copper (II) oxide nanoparticles of similar hydrodynamic diameter on human differentiated intestinal Caco-2 cell monolayers is correlated in part to copper release and shape. Nanotoxicology. 2012;6:789–803.

334. Georgantzopoulou A, Serchi T, Cambier S, Leclercq CC, Renaut J, Shao J, et al. Effects of silver nanoparticles and ions on a co-culture model for the gastrointestinal epithelium. Part Fibre Toxicol. 2016;13:9.

335. Proquin H, Jonkhout MCM, Jetten MJ, van Loveren H, de Kok TM, Briedé JJ. Transcriptome changes in undifferentiated Caco-2 cells exposed to food-grade titanium dioxide (E171): contribution of the nano- and micro- sized particles. Sci Rep. 2019;9:18287.

336. Singh A, Mandal UK, Narang RK. Development and In Vivo Evaluation of Pectin Based Enteric Coated Microparticles Loaded with Mesalamine and Saccharomyces boulardii for Management of Ulcerative Colitis. Assay Drug Dev Technol. 2022;20:22–34.

337. Danopoulos E, Twiddy M, Rotchell JM. Microplastic contamination of drinking water: A systematic review. PLoS One. 2020;15:e0236838.

338. Visalli G, Facciolà A, Pruiti Ciarello M, De Marco G, Maisano M, Di Pietro A. Acute and Sub-Chronic Effects of Microplastics (3 and 10 µm) on the Human Intestinal Cells HT-29. Int J Environ Res Public Health. 2021;18.

339. Lebedová J, Bláhová L, Večeřa Z, Mikuška P, Dočekal B, Buchtová M, et al. Impact of acute and chronic inhalation exposure to CdO nanoparticles on mice. Environmental Science and Pollution Research. 2016;23:24047–60.

340. Worsøe J, Fynne L, Gregersen T, Schlageter V, Christensen LA, Dahlerup JF, et al. Gastric transit and small intestinal transit time and motility assessed by a magnet tracking system. BMC Gastroenterol. 2011;11:145.

341. Kämpfer AAM, Urbán P, La Spina R, Jiménez IO, Kanase N, Stone V, et al. Ongoing inflammation enhances the toxicity of engineered nanomaterials: Application of an in vitro co-culture model of the healthy and inflamed intestine. Toxicology in Vitro. 2020;63:104738.

342. Schulze C, Schaefer UF, Voetz M, Wohlleben W, Venzago C, Lehr C-M. Transport of Metal Oxide Nanoparticles Across Calu-3 Cell Monolayers Modelling the Air-Blood Barrier. EURO-NanoTox-Letters. 2015;3:1–10.

343. Lindner M, Laporte A, Block S, Elomaa L, Weinhart M. Physiological shear stress enhances differentiation and mucus-formation of intestinal epithelial cells in vitro. 2020;

344. Burns KE, Uhrig RF, Jewett ME, Bourbon MF, Krupa KA. Characterizing the Role of Biologically Relevant Fluid Dynamics on Silver Nanoparticle Dependent Oxidative Stress in Adherent and Suspension In Vitro Models. Antioxidants (Basel). 2021;10.

345. Breitner EK, Hussain SM, Comfort KK. The role of biological fluid and dynamic flow in the behavior and cellular interactions of gold nanoparticles. J Nanobiotechnology. 2015;13:56.

346. PySAXS [Internet]. Available from: https://pypi.org/project/pySAXS/

347. Bhattacharya K, Kiliç G, Costa PM, Fadeel B. Cytotoxicity screening and cytokine profiling of nineteen nanomaterials enables hazard ranking and grouping based on inflammogenic potential. Nanotoxicology. 2017;11:809–26.

348. Kroll A, Gietl JK, Wiesmüller GA, Günsel A, Wohlleben W, Schnekenburger J, et al. In vitro toxicology of ambient particulate matter: correlation of cellular effects with particle size and components. Environ Toxicol. 2013;28:76–86.

349. Eder KM, Marzi A, Barroso Á, Ketelhut S, Kemper B, Schnekenburger J. Label-Free Digital Holographic Microscopy for In Vitro Cytotoxic Effect Quantification of Organic Nanoparticles. Cells. 2022;11.

350. Van der Linden SC, von Bergh ARM, van Vught-Lussenburg BMA, Jonker LRA, Teunis M, Krul CAM, et al. Development of a panel of high-throughput reporter-gene assays to detect genotoxicity and oxidative stress. Mutation Research/Genetic Toxicology and Environmental Mutagenesis. 2014;760:23–32.

351. Keshavan S, Gupta G, Martin S, Fadeel B. Multi-walled carbon nanotubes trigger lysosome-dependent cell death (pyroptosis) in macrophages but not in neutrophils. Nanotoxicology. 2021;15:1125–50.

352. Martin S, de Haan L, Miro Estruch I, Eder KM, Marzi A, Schnekenburger J, et al. Pre-validation of a reporter gene assay for oxidative stress for the rapid screening of nanobiomaterials. Frontiers in Toxicology. 2022;4.

353. Centre JR, Sustainability I for E and, Protection I for H and C, Measurements I for RM and, Maier G, Romazanov J, et al. NM-Series of representative manufactured nanomaterials – NM-300 silver characterisation, stability, homogeneity. Publications Office; 2011.

354. Centre JR, Protection I for H and C, Rasmussen K, Mast J, De Temmerman P, Verleysen E, et al. Titanium dioxide, NM-100, NM-101, NM-102, NM-103, NM-104, NM-105 – Characterisation and physico-chemical properties. Publications Office of the European Union; 2014.

355. Bi X, Westerhoff P. Ferric reducing reactivity assay with theoretical kinetic modeling uncovers electron transfer schemes of metallic-nanoparticle-mediated redox in water solutions. Environ Sci: Nano. 2019;6:1791–8.

356. Zhang L, Zou L, Jiang X, Cheng S, Zhang J, Qin X, et al. Stabilization of Nrf2 leading to HO-1 activation protects against zinc oxide nanoparticles-induced endothelial cell death. Nanotoxicology. 2021;15:779–97.

357. Wu L, Wen W, Wang X, Huang D, Cao J, Qi X, et al. Ultrasmall iron oxide nanoparticles cause significant toxicity by specifically inducing acute oxidative stress to multiple organs. Part Fibre Toxicol. 2022;19:24.

358. Bobyk L, Tarantini A, Beal D, Veronesi G, Kieffer I, Motellier S, et al. Toxicity and chemical transformation of silver nanoparticles in A549 lung cells: dose-rate-dependent genotoxic impact. Environ Sci: Nano. 2021;8:806–21.

359. Sun Q, Tan D, Zhou Q, Liu X, Cheng Z, Liu G, et al. Oxidative damage of lung and its protective mechanism in mice caused by long-term exposure to titanium dioxide nanoparticles. J Biomed Mater Res A. 2012;100:2554–62.

360. Sehsah R, Wu W, Ichihara S, Hashimoto N, Hasegawa Y, Zong C, et al. Role of Nrf2 in inflammatory response in lung of mice exposed to zinc oxide nanoparticles. Part Fibre Toxicol. 2019;16:47.

361. Xia T, Hamilton RF, Bonner JC, Crandall ED, Elder A, Fazlollahi F, et al. Interlaboratory evaluation of in vitro cytotoxicity and inflammatory responses to engineered nanomaterials: the NIEHS Nano GO Consortium. Environ Health Perspect. 2013;121:683–90.

362. Dusinska M, Boland S, Saunders M, Juillerat-Jeanneret L, Tran L, Pojana G, et al. Towards an alternative testing strategy for nanomaterials used in nanomedicine: lessons from NanoTEST. Nanotoxicology. 2015;9 Suppl 1:118–32.

363. Kermanizadeh A, Gosens I, MacCalman L, Johnston H, Danielsen PH, Jacobsen NR, et al. A Multilaboratory Toxicological Assessment of a Panel of 10 Engineered Nanomaterials to Human Health--ENPRA Project--The Highlights, Limitations, and Current and Future Challenges. J Toxicol Environ Health B Crit Rev. 2016;19:1–28.

364. Piret J-P, Bondarenko OM, Boyles MSP, Himly M, Ribeiro AR, Benetti F, et al. Pan-European inter-laboratory studies on a panel of in vitro cytotoxicity and pro-inflammation assays for nanoparticles. Arch Toxicol. 2017;91:2315–30.

365. Teunenbroek T Van, Baker J, Dijkzeul A. Towards a more effective and efficient governance and regulation of nanomaterials. Part Fibre Toxicol. 2017;14:54.

366. Rasmussen K, Rauscher H, Kearns P, González M, Riego Sintes J. Developing OECD test guidelines for regulatory testing of nanomaterials to

ensure mutual acceptance of test data. Regul Toxicol Pharmacol. 2019;104:74–83.

367. Mech A, Gottardo S, Amenta V, Amodio A, Belz S, Bøwadt S, et al. Safe- and sustainable-by-design: The case of Smart Nanomaterials. A perspective based on a European workshop. Regul Toxicol Pharmacol. 2022;128:105093.

9 Abbreviations

53BP1: Tumor Suppressor P53-binding Protein 1

ACTB: Beta-actin

AJs: Adherent Junctions

ANOVA: ANalysis Of VAriance

Ap: Apical

ATCC: American Type Culture Collection

Bl: Basolateral

BSA: Bovine Serum Albumin

CFU: Colony-forming Unit

CLAUD: caludin

CNPs: Carbon Nanoparticles

DAPI: 4′,6-diamidino-2-phenylindole

DCC-FCS: charcoal-stripped foetal calf serum

DCFDA: 5-(and-6)-chloromethyl-2′,7′-dichorodihydrofluorescein diacetate-acetoxymethyl ester

disulfonate)

DLS: Dynamic Light Scattering

DMEM: Dulbecco's Modified Eagle Medium

DMSO: Dimethyl sulfoxide

DNA: DesoxyriboNucleic Acid

DTT: Dithiothreitol

ECACC: European Collection of Authenticated Cell Cultures

ELISA: Enzyme-linked Immunosorbent Assay

ELS: Electrophoretic Light Scattering

EPR: Electron Paramagnetic Resonance spectroscopy

FBS: Foetal Bovine Serum

FITC: Fluorescein Isothiocyanate

FNPs: Magnetite Nanoparticles

FPIA: Flow Particle Imaging Analysis

HBSS: Hanks' Balanced Salt Solution

HCS: High-Content Screening

HDPE: High-density polyethylene

HNPs: Hydroxyapatite Nanoparticles

HREM: high resolution

HSD: Honestly Significant Difference

IBD: Inflammatory Bowel Disease

IBS: Irritable Bowel Syndrome

IF: Induction Factor

Ig: Immunoglobin

IL: Interleukin

LAL: Limulus Amoebocyte Lysate

LDPE: Low-density polyethylene

LFQ: Label Free Quantification

LSNPs: Lipid Surfactant Nanoparticles

LY: Lucifer Yellow

M-cells: Microfold Cells

MLT: Melatonin

MM: Micromaterial

MP: Microplastic

MUC: Mucin

NBM: Nano-biomaterial

NEAA: Non-Essential Aminiacids

NM: Nanomaterial

NOS2: Nitric Oxide Synthase 2

NRF2: nuclear factor erythroid 2-related factor 2

NTA: Nanoparticle Tracking Analysis

OCCL: occludin

OGI: Oral-gastro-intestinal

Papp: apparent permeability

PBS: Phosphate Buffered Saline

PDI: Polydispersion Index

PEG: Poly(Ethylene glycol)

PET: polyethylene terephthalate

PLGA: Poly(lactic-co-glycolic acid)

PS: Penicillin/Streptomycin

PS: Polystirene

PVC: Polyvinyl chloride

qRT-PCR: quantitative Real Time – Polymerase Chain Reaction

RFU: Relative Fluorescence Units

RLU: Relative Light Unit

RNA: RiboNucleic Acid

ROS: Reactive Oxygen Species

SAED: selected area electron diffraction

SBF: Simulated Bile Fluid

SD: standard deviation

SDF: Simulated Duodenal Fluid

SDS-PAGE: Sodium Dodecyl Sulphate - PolyAcrylamide Gel Electrophoresis

SEM: Scanning Electron Microscope

SF: Simulated Digestive Fluid

SGF: Simulated Gastric Fluid

SHDS: Simulated Human Digestion System

SIF: Simulated Intestine Fluid

SPSS: Statistical Package for Social Science

SSF: Simulated Saliva Fluid

TEER: Trans-epithelial electrical resistance

TEM: Transmission Electron Microscope

TJP1: Tight Junction Protein-1 or Zonula Occludens-1

TJs: Tight Junctions

TNF-α: Tumor Necrosis Factor α

TSB: Tryptic Soy Broth

WGA: Wheat Germ Agglutinin

WST-1: (4-[3-(4-iodophenyl)-2-(4-nitrophenyl)-2H-5-tetrazolio]-1,3-benzene

10 Publications

1. Martin S, de Haan L, Miro Estruch I, Moritz Eder K, Marzi A, Schnekenburger J, Blosi M, Costa A, **Antonello G**, Bergamaschi E, Riganti C, Beal D, Carrière M, Taché O, Hutchison G, Malone E, Young L, Campagnolo L, La Civita F, Pietroiusti A, Devineau S, Baeza A, Boland S, Zong C, Ichihara G, Fadeel B, Bouwmeester H. Pre-validation of a reporter gene assay for oxidative stress for the rapid screening of nanobiomaterials. Front Toxicol. 2022 Sep 5;4:974429. doi: 10.3389/ftox.2022.974429.

2. **Antonello G**, Marucco A, Gazzano E, Kainourgios P, Ravagli C, Gonzalez-Paredes A, Sprio S, Padín González E, Soliman MG, Beal D, Barbero F, Gasco P, Baldi G, Carriere M, Monopoli M, Charitidis CA, Bergamaschi E, Fenoglio I & Riganti C. Changes of physico-chemical properties of nano-biomaterials by digestion fluids affect the physiological properties of epithelial intestinal cells and barrier models. Part Fibre Toxicol. 2022 Jul 19;19(1):49. doi: 10.1186/s12989-022-00491-w.

3. Kokalari I, Keshavan S, Rahman M, Gazzano E, Barzan G, Mandrile L, Giovannozzi A, Ponti J, **Antonello G**, Monopoli M, Perrone G, Bergamaschi E, Riganti C, Fadeel B, Fenoglio I. Efficacy, biocompatibility and degradability of carbon nanoparticles for photothermal therapy of lung cancer. Nanomedicine (Lond). 2021 Apr;16(9):689-707. doi: 10.2217/nnm-2021-0009.

4. Contino M, Guglielmo S, Riganti C, **Antonello G**, Perrone MG, Giampietro R, Rolando B, Fruttero R, Colabufo NA. One molecule two goals: A selective P-glycoprotein modulator increases drug transport across gastro-intestinal barrier and recovers doxorubicin toxicity in multidrug resistant cancer cells. Eur J Med Chem 2020 Sep 17;208:112843. doi: 10.1016/j.ejmech.2020.112843.

11 Acknowledgments

This thesis project has received funding from the European Union’s Horizon 2020 research and innovation programs “BIORIMA” and “PlasticsFatE” under grant agreement No 760928 and No 965367.

Above all, I thank the Professors who allowed me to live this experience and who helped me grow, not only professionally, but also personally.
I would like to thank all the people who collaborated on this thesis project, in particular the people who followed and trained me over these years and the people who hosted and followed me during my period abroad.

UNITO		**GAIKER**	
Dr. Arianna Marucco	Dr. Martina Godel	Dr. Juliana Carrillo Romero	Dr. Josu Berganza Granda
Dr. Camille Macaraig Mansilungan	Dr. Muhlis Akman	Dr. Isabel Rodríguez Llopis	Dr. Amaia Aspiazu Zubiaurre
Dr. Carolina Belisario	Dr. Sabrina Digiovanni	Dr. Albiñe Leizea	Dr. Olatz Suarez
Dr. Cristian Simo	Dr. Simona Fontana	Dr. Adrián García Salvador	Dr. Eneritz Arriaga Etxano
Dr. Francesco Barbero	Dr. Stefano Zamariola	Dr. Aida García	Dr. Itziar Polanco Garriz
Dr. Giulia Orlandin	Dr. Susanna Papillo	Dr. Paloma Gómez Fernández	Dr. Felipe Goñi
Dr. Ida Kokalari	Dr. Valeria Ramundo	Dr. Ibai Nafarrate Mendez	Dr. Alberto Katsumiti
Dr. Iris Salaroglio	Prof. Chiara Riganti	Dr. Gartze Mentxaka Miranda	Dr. Filippo Chierchini
Dr. Joanna Kopecka	Prof. Elena Gazzano	Dr. Ainhoa Bilbao	
Dr. Luca Traina	Prof. Enrico Bergamaschi	Dr. Alejandra López Iruretagoyena	
Dr. Marianna Esposito	Prof. Ivana Fenoglio		

Université Paris Cité

Dr. Sonja Boland

Prof. Armelle Baeza

Prof. Stéphanie Devineau

Edinburgh Napier University

Dr. Lesley Young

Prof. Eva Malone

Prof. Gary Hutchison

Université Grenoble Alpes

Dr. David Beal

Dr. Marie Carriere

Nanovector Srl

Dr. Ana Gonzalez-Paredes

Dr. Paolo Gasco

Karolinska Institutet

Dr. Sebastian Martin

Prof. Bengt Fadel

Colorobbia Consulting Srl

Dr. Costanza Ravagli

Dr. Giovanni Baldi

Westfälische Wilhelms-University

Dr. Anne Marzi

Dr. Kai Moritz Eder

Prof. Jürgen Schnekenburger

Wageningen University and Research

Dr. Ignacio Miro Estruch

Dr. Laura de Haan

Prof. Hans Bouwmeester

Tokyo University of Science

Prof. Cai Zong

Prof. Gaku Ichihara

National Technical University of Athens

Dr. Panagiotis Kainourgios

Prof. Costas A. Charitidis

Université Paris-Saclay

Dr. Olivier Taché

Royal College of Surgeons in Ireland

Prof. Marco Monopoli

Dr. Esperanza Padín-González

University of Rome Tor Vergata

Dr. Fabio la Civita

Dr. Micol Massimiani

Dr. Valentina Lacconi

Prof. Antonio Pietroiusti

Prof. Luisa Campagnolo

ISTEC-CNR

Dr. Anna Costa

Dr. Magda Blosi

Dr. Simone Sprio

Finally, I would like to thank all the people who have been close to me in these years and who have supported me by advising me, helping me to face the most difficult periods and sharing with me the joys linked to this journey: Cristian, my parents, my sister, my brother-in-law, Giulia, Chiara, Barbara, Davide and all the friends who have in some way shared this journey with me.